Doctoral Dissertations   Student Scholarship

Winter 2011

A computational fluid dynamics study of two-phase flows in the presence of surfactants

Yuanyuan Cui
University of New Hampshire, Durham

Follow this and additional works at: https://scholars.unh.edu/dissertation

A COMPUTATIONAL FLUID DYNAMICS STUDY OF TWO-PHASE FLOWS IN THE PRESENCE OF SURFACTANTS

BY

Yuanyuan Cui

B.S., Chem. Engr., Beijing Univ. Chem. Tech., July. 2004
M.S., Chem. Engg, Beijing Univ. Chem. Tech., Dec. 2006

DISSERTATION

Submitted to the University of New Hampshire
in partial fulfillment of
the requirements for the degree of

Doctor of Philosophy

in

Chemical Engineering

December 2011

UMI Number: 3500780

UMI®

Dissertation Publishing
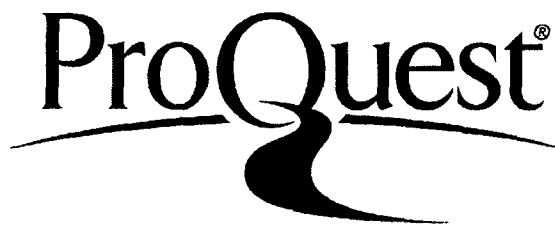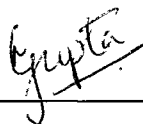
ProQuest®

ProQuest LLC
789 East Eisenhower Parkway
P.O. Box 1346
Ann Arbor, MI 48106-1346

This dissertation has been examined and approved.

Dissertation Director, Nivedita R. Gupta
Associate Professor of Chemical Engineering

Palligarnai T. Vasudevan
Professor of Chemical Engineering

Russell T. Carr
Professor of Chemical Engineering

Qing Song
Assistant Professor of Chemical Engineering

Gregory P. Chini
Associate Professor of Mechanical Engineering

DECEMBER 16, 2011
Date

Dedication

To my parents.

Acknowledgments

I would like to express my strong gratitude to my advisor, Dr. Gupta, for her continuous guidance and support of my Doctoral research. Her immense knowledge, patience, motivation, and enthusiasm helped me a lot during my Doctoral study and will influence my whole life. I feel very lucky to have such a great advisor. Beside my advisor, I would like to e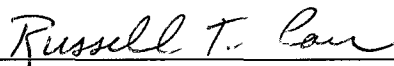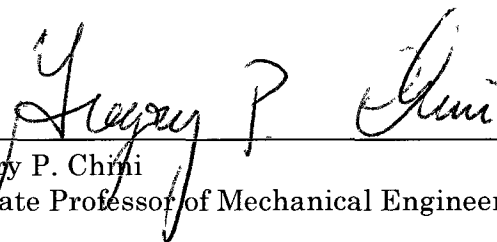xpress sincere gratitude to Dr. Vasudevan for all his great help and support in the past five years and for taking time to be on my dissertation committee. I also would like to heartily thank Dr. Carr, Dr. Song and Dr. Chini for taking time to be on my dissertation committee and for their encouragement and insightful guidance in my study and life.

I would like to thank my current and previous labmates at Interfacial Phenomena lab: Robert M. Carroll, Xiameng Liu, Weihua Li, Michael O' Connor, and Jingyan Li, for all the help and stimulating discussions. Besides, I would like to thank Mr. Jonathan E. Newell for his assistance with customized capillaries for our experimental work and help in my teaching assistance lab duties.

Last but not the least, I would like to thank my family and all my friends who support me all the time.

Table of Contents

List of Tables

List of Figures

ABSTRACT

A COMPUTATIONAL FLUID DYNAMICS STUDY OF TWO-PHASE FLOWS IN THE PRESENCE OF SURFACTANTS

by

Yuanyuan Cui

University of New Hampshire, December, 2011

Drop formation in co-flowing fluids and drops rising in a tube are important in applications such as microencapsulation and enhanced oil recovery. A hybrid volume-of-fluid method with a front-tracking scheme is developed to study two-phase flows in the presence of surfactants at finite Reynolds numbers. Both fluids can be Newtonian or shear-thinning, and surfactants are soluble in the adsorption-desorption limit. A drop in the co-flowing geometry typically breaks up at the primary neck. The drop breaks faster with smaller volumes as the outer flow rate increases or the drop viscosity decreases. When surfactants are present, they accumulate in the neck region resulting in Marangoni stresses that slow down the neck thinning rate. This results in longer breakup times with larger drop volumes. At high surfactant coverages, the primary neck formation slows down enough and breakup occurs at the secondary neck. Increasing outer co-flowing flow weakens the retarding effect of the high surfactant coverage leading to breakup again at the primary neck. The adsorption-desorption kinetics also affects the neck breakup position, and the primary drop volume and breakup time depend non-linearly on the Biot number. The presence of a confining wall may lower the value of the critical equilibrium fractional coverage required for the drop to enter the no-necking regime. As the drop becomes more shear-thinning, the drop breaks up faster with a shorter remnant drop length. Multiple satellite drops are observed at breakup with strongly shear-thinning drop fluid at high coverage of soluble surfacants. The buoyancy-driven motion of drops in a tube is investigated by determining the

steady shapes and velocities of the drops as a function of the drop size. Higher buoyancy force leads to larger deformation of drops and increased terminal velocities. Higher inertia increases the terminal velocity of drops and results in the development of negative curvatures at the rear of the drop. The non-uniform distribution of surfactants at the interface gives rise to Marangoni stresses that retard the drop motion though the drop shapes remain unaffected.

Chapter 1

Introduction

1.1 Two-Phase Flows in Nature and Industry

Two-phase flows involving drops and bubbles are encountered in a number of natural and industrial processes such as rainfall, boiling, inkjet printing, and enhanced oil recovery. In processes such as microencapsulation, inkjet printing, and spray coating, generation of droplets of controllable size is crucial. Several strategies are used to generate monodisperse drops in an immiscible ambient fluid such as a co-flowing or flow focusing geometry [8, 9]. Once generated, the motion and deformation of drops and bubbles in confined geometries is important in applications such as oil recovery, solvent extraction, and polymer processing. It has also been used as a pore-scale model for understanding the dynamics of two-phase flows in porous media [92] and as a model for blood flow in capillaries [114]. Determining the interplay of interfacial, viscous, inertial, and gravitational forces on the formation, deformation, and mobility of drops and bubbles is key to understanding and optimizing processes involving two-phase flows.

Surface active agents or surfactants are amphiphiles that adsorb at the interface and can critically affect the dynamics of two-phase flow systems [28, 118]. In several processes, surfactants are typically present either naturally or as impurities that are

1

difficult to remove. For example, in the pulmonary system, surfactants play a vital role in reducing the work required to expand lungs with each breath by reducing the surface tension of the liquid lining alveoli and airways. A lack of pulmonary surfactant causes respiratory distress syndrome in premature neonates [6]. Surfactants are sometimes deliberately added to two-phase systems as stabilizers or emulsifiers [31, 66, 67, 129, 150]. In recent microfluidic applications, surfactants have been used to manipulate drops and bubbles in microchannels [119] and to synthesize monodisperse drops and bubbles [3]. When surfactants accumulate at the interface, drop coalescence can be inhibited, which is essential for the long-term stability of monodisperse emulsions [11]. This benefits industrial operations where drop coalescence is undesirable such as a gas-liquid reaction where drop coalescence can reduce the overall interfacial area and lower the reactor efficiency. Surfactants are also used to suppress the occurrence of satellite drops during the drop formation process [31, 66]. This is useful in applications such as inkjet printing where satellite drops can blur the image during printing. A thorough understanding of how surfactants affect drop break up and deformation can therefore help in improving process and device design.

In applications such as printing, coating, polymer processing, and biomedical microdevices, the fluids of interest may be non-Newtonian. Early rheology experiments done by Pangalos et al. [97] showed that several ink formulations were shear-thinning, that is, their viscosity decreased with increasing shear stress. Recent work by Fernandez et al. [46] reported that highly pigmented inks exhibited shear-thinning as well as viscoelastic properties. Various types of polymers such as polymer suspensions, melts, and blends used in paint and coating industry exhibit shear-thinning or viscoelastic behavior [13, 133, 127]. Biological fluids such as blood and DNA solutions used in biomedical microdevices also show shear-thinning or viscoelastic behavior [51, 113, 114]. It is well-known that non-Newtonian liquids respond to an

applied stress field dramatically differently than Newtonian liquids. Therefore, determining the effect of non-Newtonian rheology on the drop formation, deformation and mobility in two-phase flows will improve our understanding of two-phase processes involving inks, paint, and biofluids.

1.2 Surfactants at Interfaces

Drops and bubbles in two-phase flows show interesting dynamics compared to solid particles due to their deformable interface [28, 73]. The deformable interface between two fluids is actually a thin layer which is a few molecular dimensions thick. The thickness is not well defined since the physical properties of the fluid vary rapidly but continuously in the interfacial region from the values of one bulk phase to that of the other. Due to lack of appropriate molecular theories to describe the interface, it is treated as a massless and zero-thickness boundary where the fluid properties are maintained at the bulk values on either side of the interface and change discontinuously at the interface. The interface is characterized by the interfacial tension, σ, which depends on its local thermodynamic state such as temperature, pressure, and the concentration of any solutes such as surfactants and charged particles, but is not dependent on whether the interface is undergoing deformation or any macroscopic motion [73]. Interfacial tension can be viewed as the net inward force of molecular attraction per unit length experienced by fluid molecules at the interface that minimizes its interfacial area. It can also be interpreted as the work done to generate a unit area of new interface.

Surfactants have an amphiphilic molecular structure consisting of a hydrophilic (water-loving) head and a hydrophobic (water-repelling) tail. The hydrophobic tail is usually a long-chain hydrocarbon and the hydrophilic head is usually a highly po-

lar or ionic group. Depending on the nature of the hydrophilic head, surfactants can be classified as: nonionic, anionic, cationic, or zwitterionic [108]. Detergent is one familiar example of surfactants, but many substances including salts and fatty acids and even polymers can act as surfactants. When surfactants are dissolved in water, the hydrophobic group may distort the structure of water and increase the free energy of the system. The system responds by expelling the surfactant molecule to the interface to minimize contact between the hydrophobic group and water and reduce the free energy of the system. As a result, the interface becomes covered with surfactant molecules with their hydrophobic tails pointing into non-aqueous phase (air or oil) while keeping their hydrophilic heads in the water phase to decrease the dissimilarity of the two phases contacting each other at the interface. The adsorption of surfactants at the interface can lower the energy of the interface resulting in a reduction in the interfacial tension. Consider an air-water or an oil-water interface with a clean interfacial tension, σ_o, created suddenly in the presence of surfactants as shown in Fig. 1-1. If the surfactants have enough time to adsorb onto the interface and reach an equilibrium, the interfacial tension reduces to its equilibrium value, σ_{eq}, which is less than σ_o. The equilibrium interfacial tension, σ_{eq}, depends on the bulk concentration of surfactants. If experiments are conducted to determine the equilibrium interfacial tension for varying bulk surfactant concentrations, a plot similar to Fig. 1-2 is obtained. For small bulk surfactant concentrations, the equilibrium interfacial tension remains nearly identical to the clean interfacial tension. With increasing bulk concentration of surfactants, the equilibrium interfacial tension decreases until it reaches a plateau value at a certain critical concentration known as the critical micelle concentration (CMC). Beyond CMC, surfactants start to aggregate and form micelles inside the bulk solution resulting in a nearly constant interfacial tension [108]. As this dissertation is concerned with only non-micellar surfactant
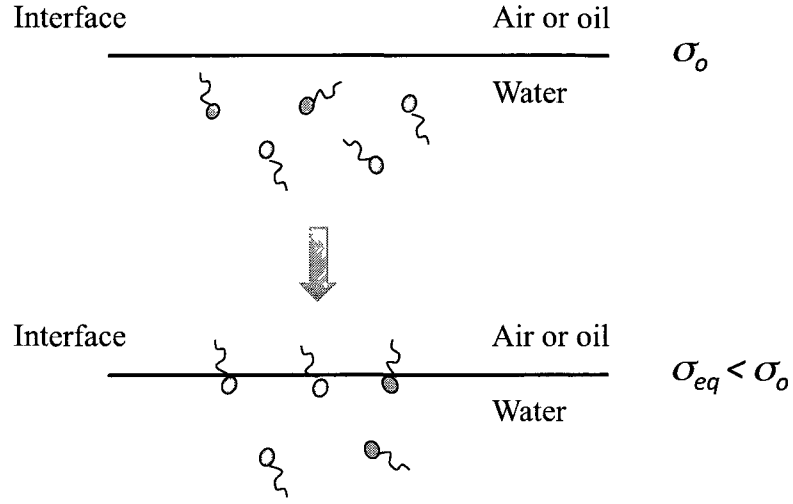
Figure 1-1: Schematic of equilibrium behavior of surfactant molecules at the interface.

solution, the following discussion assumes that the bulk concentration is less than CMC.

In dynamic flow situations, equilibrium conditions are usually not achieved along the interface. The reduction in interfacial tension by surfactants can alter the stress conditions along the interface and eventually alter the interfacial hydrodynamics [73]. Since the interface is viewed as a massless and zero-thickness boundary, the volume of any segment of the interface is zero, and the net force acting on the interface must also be zero. Two types of forces act on any segment of the interface: the bulk pressure and stresses acting on the faces of the interface element proportional to the interfacial area and a tensile force due to the interfacial tension acting in the plane of the interface at the edges of the interface element. A force balance at the interface is given in the following mathematical form [73]:
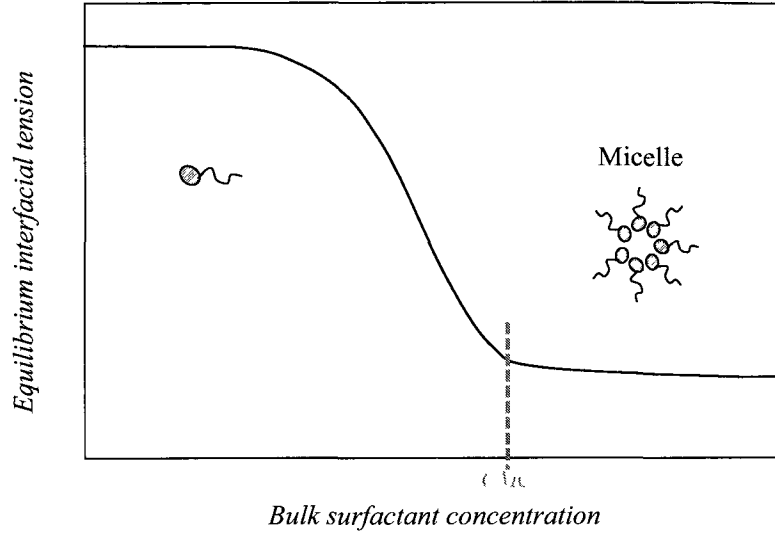
Figure 1-2: Schematic of equilibrium interfacial tension as a function of bulk surfactant concentration.

$$(p_1 - p_2) \mathbf{n} + (\tau_2 - \tau_1) \cdot \mathbf{n} = \sigma \mathbf{n} (\nabla \cdot \mathbf{n}) - \nabla_s \sigma, \tag{1.1}$$

where the subscripts 1 and 2 denotes the two phases, p_i and τ_i ($i = 1$ or 2) are the actual total pressure and the deviatoric stress tensor exerted on the fluids, and $\mathbf{n}$ is the outward pointing unit normal from phase 1 into phase 2. Eq. 1.1 shows that the force balance across the interface requires that the total stress across the interface undergo a jump. The normal stress jump across the interface is given by the product of the interfacial tension and the mean curvature of the interface while the tangential stress jump across the interface is given by the gradient of interfacial tension. Surfactants adsorbed at a drop or bubble interface alter the stress jump balance shown in Eq. 1.1 in two ways. First, a local accumulation of surfactants along the interface lowers the interfacial tension there. To balance the normal stress jump across the interface, the interface in these low interfacial tension regions deforms to produce a larger curvature as seen in Fig. 1-3(a). This affects the deformation of drops and bubbles in the

6
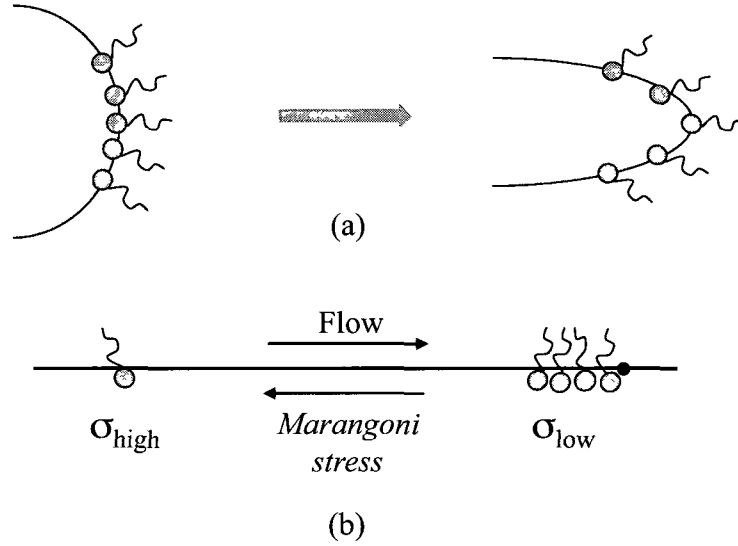
Figure 1-3: Schematic of the effect of non-uniform distribution of surfactants on the dynamics of interface based on (a) normal stress balance and (b) tangential stress balance.

presence of surfactants, which in turn affects its mobility. Second, if a non-uniform distribution of surfactants is generated along the interface due to a stagnation point in the flow, a non-uniform interfacial tension along the interface results. As shown in Fig. 1-3(b), a gradient in interfacial tension generates additional tangential stresses known as Marangoni stresses which reduce the tangential velocity of the interface. This affects the mobility of drops and bubbles in the presence of surfactants.

The non-uniform distribution of surfactants at the interface depends on the relative time scales of diffusion, convection, and adsorption-desorption in the problem. While surfactants are convected and diffuse along the interface, they are also transported by adsorption-desorption and diffusion between the interface and the bulk. Fig. 1-4 presents a schematic of different timescales at play for the non-equilibrium behavior of surfactants at the interface with interfacial flow. Convection at the interface leads to a local accumulation of surfactants at stagnation points represented by a

"dot" at the interface in Fig. 1-4. The timescale for surface convection, τ_{SC}, depends on the tangential velocity at the interface. The timescale of mass transport of surfactants between the interface and the bulk solution, τ_{MT}, depends on the timescale of adsorption and desorption of surfactants between the sublayer and the interface, τ_{AD}, and the timescale of bulk diffusion of surfactants between the bulk and the sublayer, τ_D. If $\tau_{MT} \ll \tau_{SC}$, the interface gets replenished with surfactants very quickly to achieve a uniform reduction of interfacial tension along the interface. If on the other hand, $\tau_{MT} \gg \tau_{SC}$, there is almost no exchange of surfactants between the bulk and the interface and the surfactants are essentially insoluble. If $\tau_{MT} \sim \tau_{SC}$, the relative magnitudes of τ_{AD} and τ_D determines the behavior of the surfactants. For example, in the adsorption-desorption limit, $\tau_{AD} \gg \tau_D$, and the sublayer concentration of surfactants is equal to the bulk surfactant concentration. In the diffusion-controlled limit, $\tau_{AD} \ll \tau_D$, and there will be a surfactant concentration gradient between the bulk and the sublayer. The same surfactant two-phase system may behave differently depending on the surfactant concentration and flow conditions.

1.3   Non-Newtonian Rheology Effect

The viscosity of a Newtonian fluid is independent of the shear rate, and depends only on temperature, pressure, and the chemical composition of the fluid. In several industries such as food, cosmetics, biomedical, and polymer processing, the fluids exhibit non-Newtonian behavior. Unlike a Newtonian fluid, the viscosity of a non-Newtonian fluid changes with shear rate or even shear rate history. Non-Newtonian fluids are generally classified into three categories: purely viscous time-independent or generalized Newtonian fluids (GNF), time-dependent fluids, and viscoelastic fluids [26]. For time-independent fluids, the shear rate only depends on the current value of

8
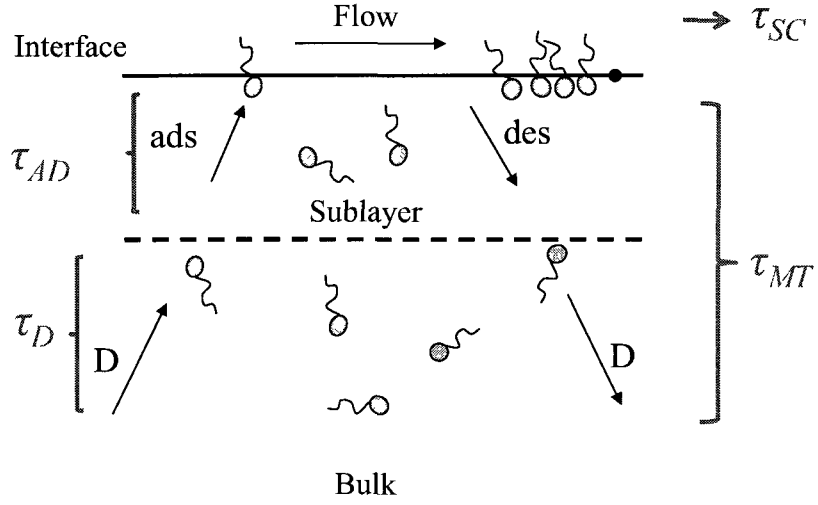
Figure 1-4: Schematic of non-equilibrium behavior of surfactant molecules at the interface.

(a)   (b)
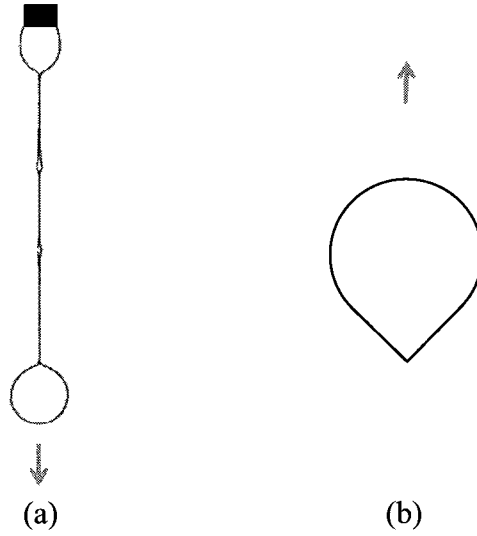
Figure 1-5: Schematic of (a) the "bead-on-string" pattern observed during in a viscoelastic drop formed into a quiescent air[143] and (b) the cusp formation seen during a bubble rising in a quiescent viscoelastic fluid[80].

the shear stress. If the apparent viscosity defined as the shear stress divided by shear rate for a fluid decreases with increasing shear rate, it is classified as a shear-thinning or pseudoplastic fluid. If its apparent viscosity increases with increasing shear rate it is termed as a shear-thickening or dilatant fluid. For time-dependent fluids, shear stress depends on shear rate, the duration of shearing, the previous kinematic history and so on. A thixotropic fluid shows decreased apparent viscosity with time when sheared at a constant shear rate, whereas a rheopectic fluid shows a increased apparent viscosity with the duration of shearing. For viscoelastic fluids, materials exhibit combined characteristics of both a viscous fluid and an elastic solid showing partial elastic and recoil recovery after deformation. Rod climbing and die-swelling phenomena are examples of peculiar behavior of viscoelastic fluids due to extra normal stresses generated in the fluids. Several interesting two-phase dynamics such as "bead-on-a-string" structure and cusp formation are seen in viscoelastic liquids (see Fig. 1-5). During the thinning of a viscoelastic thread, the competition of elastic, capillary, and inertial forces leads to the formation of a periodic array of beads connected by axially uniform ligaments known as "bead-on-a-string" [77, 94, 143]. Formation of a cusp is seen at the rear stagnation point of bubbles rising in a quiescent viscoelastic fluid due to large normal stresses when the interfacial forces are weak [80]. Most real materials often display a combination of two or even all the three types of non-Newtonian characteristic. For example, a variety of polymer solutions such as Xanthan gum, sodium acrylate, polyacrylamide, and carboxymethyl cellulose solutions exhibit both shear-thinning and viscoelastic behaviors. For diluted polymer solutions, viscoelasticity can sometimes be neglected and solutions are only considered as shear-thinning fluids. At low shear rates, the viscosity reaches a limiting value referred to as the zero shear-rate viscosity followed by a region of shear-thinning behavior.

1.4 Research Objectives

The aim of this work is to further our understanding of the dynamics of two-phase flows in confined domains in the presence of surfactant and non-Newtonian effects. The main goals are to

- develop a numerical model to simulate two-phase flows with a rapidly deforming interface,

- study the interplay of interfacial, viscous, inertial, and gravitational forces in the presence of confining walls on the dynamics of the two-phase interface,

- determine how surfactants adsorbed at the two-phase interface affect the dynamics of the interface, and

- investigate the effect of fluid rheology on the dynamics of the two-phase interface.

To achieve these goals, a numerical algorithm based on a hybrid Volume-of-Fluid (VOF) method is developed to study strongly deforming interfaces. The numerical model uses a VOF method combined with a front-tracking scheme to accurately describe the deforming interface in the presence of surfactants. The model is implemented on two different flow problems encountered in a variety of two-phase applications. The first problem is the formation of a drop at the tip of a needle in the presence of a co-flowing stream. The second problem is a drop rising in a tube filled with an immiscible fluid. Both processes are considered isothermal. Nonionic surfactants in non-micellar bulk solutions, that is, the surfactant concentration is below CMC, are chosen for the investigation of surfactant effects on these two-phase flow problems. Surfactants are considered soluble with adsorption-desorption as the

11

rate-limiting step. In addition, either the drop fluid or the bulk fluid may exhibit non-Newtonian shear-thinning behavior. The mathematical models for two-phase flows, surfactants, and non-Newtonian rheology are discussed in Chapter 2. Various numerical techniques used for two-phase flows and the numerical algorithm used in this work are presented in Chapter 3. The detailed problem description and results for drop formation in a co-flowing fluid stream and drops rising in a tube are presented in Chapters 4 and 5, respectively. Chapter 6 summarizes the conclusions of this work and presents some suggestions for future work on the subject.

Chapter 2

Mathematical Formulation

2.1 Modeling Two-phase Flows

A two-phase interface S separates the drop phase 1 from the bulk phase 2 as shown in Fig. 2-1. The outward pointing unit normal from the drop phase to the bulk phase is denoted by $\mathbf{n}$ and $\mathbf{t}$ is the unit tangent vector at the interface. Both phases are treated as isothermal and incompressible. Applying the continuum hypothesis that describes the motion of the fluid on a much coarser scale of resolution than the molecular scale [14, 73], the continuity and the equations of motion for both phases are given by

$$\nabla^* \cdot \mathbf{u}_i^* = 0, \tag{2.1}$$

$$\rho_i \left(\frac{\partial \mathbf{u}_i^*}{\partial t^*} + \mathbf{u}_i^* \cdot \nabla^* \mathbf{u}_i^* \right) = -\nabla^* P_i^* + \nabla^* \cdot \tau_i^*. \tag{2.2}$$

The superscript $*$ denotes dimensional quantities and the subscript i represents the drop phase for $i = 1$ or the bulk phase for $i = 2$. The fluid velocity and the modified pressure in phase i are represented by $\mathbf{u}_i^*$ and P_i^*, respectively. The modified pressure is defined as $P_i^* = p_i^* - \rho_i \mathbf{g} \cdot \mathbf{x}^*$ where $\mathbf{x}^*$ is the axial location vector. The deviatoric stress tensor in phase i is represented by τ_i^* and is given by

$$\tau_i^* = \mu_i \left[(\nabla^* \mathbf{u}_i^*) + (\nabla^* \mathbf{u}_i^*)^T \right]. \tag{2.3}$$
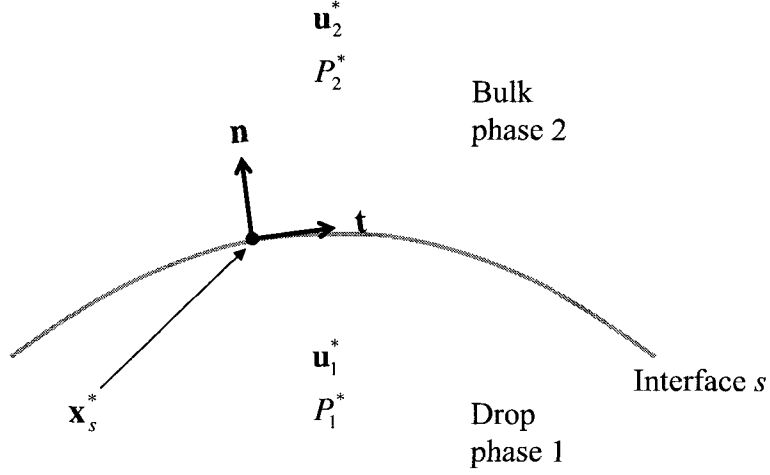
Figure 2-1: Schematic of a two-phase interface separating the drop phase from the bulk phase.

The viscosity of phase i, μ_i, is either constant for a Newtonian fluid or variable for a non-Newtonian fluid.

The governing equations in Eq.s 2.1 - 2.3 are solved with initial conditions and boundary conditions imposed at the fluid boundaries and the two-phase interface. The boundary conditions imposed at the flow domain boundary depends on the flow problem considered. Here, the three boundary conditions imposed at the two-phase interface are discussed. First, the velocity at the interface S is required to be continuous and equal to the interface velocity, that is,

$$\mathbf{u}_1^* = \mathbf{u}_2^* = \mathbf{u}_s^*. \tag{2.4}$$

Here, $\mathbf{u}_s^* = u_n^* \mathbf{n} + u_t^* \mathbf{t}$ is the interfacial velocity and u_n^* and u_t^* are the normal and tangential components. Second, the force balance at the interface results in a stress jump across the interface described by

$$(P_1^* - P_2^*)\,\mathbf{n} + (\tau_2^* - \tau_1^*) \cdot \mathbf{n} = \sigma^* \mathbf{n}\,(\nabla^* \cdot \mathbf{n}) - \nabla_s^* \sigma^* + (\rho_2 - \rho_1)\,(\mathbf{g} \cdot \mathbf{x}^*)\,\mathbf{n}. \tag{2.5}$$

14

Here, σ^* is the interfacial tension, $\nabla_s^* = (\mathbf{I} - \mathbf{nn}) \cdot \nabla^*$ is the surface gradient operator, and $\nabla^* \cdot \mathbf{n}$ is the mean curvature of the interface. Since modified pressure is used in this formulation, the hydrostatic pressure term appears on the right hand side of the stress jump balance instead of the governing equations. Eq. 2.5 shows that the normal stress jump is balanced by the Laplace pressure, $\sigma^* \mathbf{n} \, (\nabla^* \cdot \mathbf{n})$, normal to the interface, while the tangential stress jump is balanced by the Marangoni stress, $-\nabla_s^* \sigma^*$, tangent to the interface. Finally, the interface evolution is governed by the kinematic condition

$$\frac{d\mathbf{x}_s^*}{dt^*} = \mathbf{u}_s^*, \qquad (2.6)$$

where $\mathbf{x}_s^*$ is the location of the interface.

2.1.1 Dimensionless Governing Equations

Eqs. 2.1 to 2.5 are nondimensionalized with the characteristic length, l_c, velocity, u_c, and time, l_c/u_c, which depend on the flow problem considered. A viscous scale is chosen as the characteristic pressure, that is, $P_c = \mu_2 u_c/l_c$. The characteristic interfacial tension, σ_c is chosen as the clean interfacial tension, σ_o for the surfactant-free simulations and as the equilibrium interfacial tension, σ_{eq} for simulations for the surfactant-laden systems. The dimensionless forms of the continuity and the equations of motion then become

$$\nabla \cdot \mathbf{u}_i = 0, \qquad (2.7)$$

$$\tilde{\rho}_i Re \left(\frac{\partial \mathbf{u}_i}{\partial t} + \mathbf{u}_i \cdot \nabla \mathbf{u}_i \right) = -\nabla P_i + \nabla \cdot \tau_i. \qquad (2.8)$$

P_i represents the dimensionless modified pressure and $\tau_i = \tilde{\mu}_i \left[(\nabla \mathbf{u}_i) + (\nabla \mathbf{u}_i)^T \right]$ represents the dimensionless deviatoric stress tensor. The dimensionless fluid properties are defined as $\tilde{\rho}_i = 1 + (\chi - 1)\delta_{1i}$ and $\tilde{\mu}_i = 1 + (\lambda - 1)\delta_{1i}$. The ratio of density of

15

the drop phase to the bulk phase is given by $\chi = \rho_1/\rho_2$ and $\lambda = \mu_1/\mu_2$ represents the ratio of drop phase viscosity to the bulk phase viscosity. For shear-thinning fluids, the zero-shear viscosity is used to calculate the viscosity ratio. Eq. 2.8 introduces the Reynolds number, Re, which represents relative importance of inertial forces to viscous forces and is defined as

$$Re \equiv \frac{\rho_2 u_c l_c}{\mu_2}. \tag{2.9}$$

The dimensionless forms of the continuity of velocity, the stress jump condition, and the kinematic condition at the two-phase interface are given by

$$\mathbf{u}_1 = \mathbf{u}_2 = \mathbf{u}_s, \tag{2.10}$$

$$(P_1 - P_2)\mathbf{n} + (\tau_2 - \tau_1) \cdot \mathbf{n} = \frac{1}{Ca}\left[\sigma\mathbf{n}\left(\nabla \cdot \mathbf{n}\right) - \nabla_s\sigma - Boz\mathbf{n}\right], \tag{2.11}$$

$$\frac{d\mathbf{x}_s}{dt} = \mathbf{u}_s. \tag{2.12}$$

The last term in Eq. 2.11 is obtained by assuming that gravity points in the negative z–direction. The interfacial boundary conditions introduce the capillary number, Ca, which gives the relative importance of viscous forces to interfacial forces and the Bond number, Bo, gives the relative significance of gravitational forces to interfacial forces. The capillary and Bond numbers are defined as

$$Ca = \frac{\mu_2 u_c}{\sigma_c}, \tag{2.13}$$

$$Bo = \frac{(\rho_2 - \rho_1)g l_c^2}{\sigma_c}. \tag{2.14}$$

2.2 Modeling Surfactants

In the absence of bulk fluid motion, surfactants adsorb at a two-phase interface to reach an interfacial concentration, Γ_{eq}^*, which is in equilibrium with the bulk surfactant concentration C_∞^*. In the presence of bulk fluid motion, the equilibrium is

16

disturbed due to convection, diffusion, and transport of surfactants from the bulk resulting in a surfactant concentration distribution, Γ^* along the interface. To use the interfacial tension, σ^* in Eq. 2.5, two pieces of information are needed. First, how the interfacial tension, σ^* is related to the interfacial concentration, Γ^* and second, how the interfacial concentration distribution, Γ^* is evolving with time. The surface equation of state describes the relationship between σ^* and Γ^* and the surface mass balance equation describes surfactant transport at the interface.

2.2.1 Surface Equation of State

A surface equation of state describes the relationship between the interfacial tension σ^*, and the surfactant concentration at the interface Γ^*. In the limit of low surfactant concentrations, a linear equation of state can be assumed. However, as the interface gets saturated with surfactants, the finite size of the surfactant restricts the maximum amount of surfactant that can be packed at the interface. This maximum surface packing limit is given by Γ_∞ which affects how surface tension changes with surfactant concentration. In addition, surfactants can interact either cohesively or repulsively, which further affects the form of the equation of state. For this study, the simplest non-linear equation of state accounting for surface saturation effects but no interactions between surfactant molecules, namely, the Langmuir equation of state is chosen.

Assuming that the surfactant is bulk soluble, the surfactant partitions between the interface and the bulk based on an adsorption isotherm. The Langmuir isotherm assumes that surfactant molecules are non-interacting and pack at the interface in a monolayer. The surfactant adsorption rate to the interface is linear in the bulk concentration, C_∞, and slows as the interfacial concentration approaches the maxi-

mum packing limit, Γ_∞. The desorption rate is assumed to be linear in surfactant concentration at the interface. Thus, the net adsorptive-desorptive flux to and from the interface, $\mathbf{j}^* \cdot \mathbf{n}$, is given by

$$\mathbf{j}^* \cdot \mathbf{n} = \beta_s C_\infty \left(\Gamma_\infty - \Gamma^* \right) - \alpha_s \Gamma^*. \tag{2.15}$$

Here, α_s and β_s are the desorption and adsorption kinetic rate constants, respectively. At equilibrium, $\mathbf{j}^* \cdot \mathbf{n} = 0$, and Γ^* can be solved from Eq. 2.15 as

$$\Gamma_{eq} = \Gamma_\infty \frac{K_L C_\infty}{1 + K_L C_\infty}. \tag{2.16}$$

The Langmuir equilibrium adsorption constant, $K_L = \beta_s / \alpha_s$.

The appropriate surface equation of state can then be derived from the adsorption isotherm using interfacial thermodynamics. The Gibbs adsorption equation at constant temperature T is given by

$$d\sigma^* = -RT\Gamma^* d \left(ln C_\infty \right). \tag{2.17}$$

Integrating the Gibbs adsorption equation with the Langmuir adsorption isotherm gives the relationship between the interfacial tension, σ^*, and the surfactant concentration at the interface, Γ^*, as

$$\sigma^* = \sigma_o + RT\Gamma_\infty ln \left(1 - \frac{\Gamma^*}{\Gamma_\infty} \right), \tag{2.18}$$

where σ_o is the interfacial tension of the clean interface. Eq. 2.18 is known as the Langmuir equation of state. It has been shown as a good fit to experimental data for a variety of two-phase flow systems with surfactant concentrations up to the critical micelle concetration where the integrity of the surfactant monolayer is about to be compromised [23]. Thus, the Langmuir equation of state is chosen in this work to describe the adsorption kinetics of the nonionic surfactants in a non-micellar solution.

The Langmuir equation of state is derived using the Gibbs adsorption equation which holds at equilibrium. However, it is assumed to be valid for systems with surfactant under flow, with Γ^* and σ^* representing local values and C_∞ representing the limit of the bulk concentration as the same point on the interface is approached [73]. In the dilute surfactant limit ($\Gamma^*/\Gamma_\infty \ll 1$), the Langmuir equation of state reduces to a linear equation of state, $\sigma^* = \sigma_o - RT\Gamma^*$, indicating that the interfacial tension decreases linearly with surfactant concentration at the interface. At high surfactant concentrations, the Langmuir equation of state captures important nonlinear behavior of surfactants. This is clearly seen in Fig. 2-2 where the interfacial tension, σ^*, decreases sharply as the interfacial concentration of surfactants, Γ^*, approaches the maximum packing limit, Γ_∞, from below. The Marangoni stress corresponding to Eq. 2.18 is given by

$$\nabla_s^* \sigma^* = \nabla_s^* \Gamma^* \frac{\partial \sigma^*}{\partial \Gamma^*} = \nabla_s^* \Gamma^* \frac{RT}{1 - \Gamma^*/\Gamma_\infty}. \tag{2.19}$$

At low surfactant concentrations, $\Gamma^* \ll \Gamma_\infty$, the coupling between the interfacial tension and surfactant concentration is weak. Large gradients in surfactant concentration are needed to see small Marangoni stresses. At high surfactant concentrations when Γ^* approaches the maximum packing limit, Γ_∞, from below, large Marangoni stresses are expected for perturbative gradients in surfactant concentrations [43].

2.2.2 Surface Mass Balance

While surfactants are transferred by convection and diffusion along the interface, they are also transported by adsorption-desorption and diffusion between the interface and the bulk as shown in Fig. 1-4. The surfactant concentration at the interface Γ^* varies along the interface and also changes with time under flow. It is governed by the
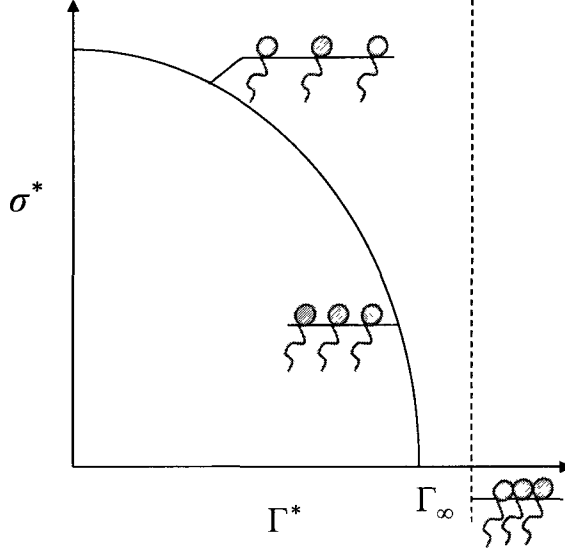
Figure 2-2: Schematic of nonlinear behavior of the Langmuir equation of state.

unsteady convective-diffusion equation [73, 117, 137] given by

$$\frac{\partial \Gamma^*}{\partial t^*} + \nabla_s^* \cdot (\Gamma^* u_t^* \mathbf{t}) + \Gamma^* (\nabla^* \cdot \mathbf{n}) u_n^* - D_s \nabla_s^{*2} \Gamma^* = \beta_s C_s (\Gamma_\infty - \Gamma^*) - \alpha_s \Gamma^*, \quad (2.20)$$

where D_s denotes the interfacial diffusivity of surfactants, and β_s and α_s are the kinetic constants for adsorption and desorption, respectively. The surfactant concentration, Γ^* at any point along the interface changes due to convection due to the local tangential velocity given by $\nabla_s^* \cdot (\Gamma^* u_t^* \mathbf{t})$. Local changes in interfacial area result in a "dilution" effect which is evaluated by the term $\Gamma^* (\nabla^* \cdot \mathbf{n}) u_n^*$. The surfactant redistributes along the interface due to an interfacial diffusion flux given by $-D_s \nabla_s^{*2} \Gamma^*$. Finally, the interface concentration also changes due to the adsorption-desorption flux between the interface and the bulk given by the right hand side of Eq. 2.20. The rate of desorption of surfactants from the interface depends on the surfactant concentration at the interface, Γ^*. This form of the adsorption flux of surfactants assumes that the adsorption rate is directly proportional to the space available on the interface given by $(\Gamma_\infty - \Gamma^*)$, and the surfactant concentration in the

20

sublayer immediately adjacent to the interface, C_s. The sublayer concentration is determined by solving the bulk convective-diffusion equation to determine the bulk concentration of surfactant everywhere in the fluid domain.

The relative timescales of the various transport processes of surfactants give rise to different asymptotic solutions to the problem. Three different asymptotic solutions are considered in this study to understand the effect of surfactant mass transfer on the drop formation and drop rising processes. First, if mass transport of surfactants to the interface is much faster than interfacial convection, the adsorptive-desorptive flux to the interface is very large. Thus, the interface is continuously replenished with surfactants and the surfactant concentration at the interface always remains at the equilibrium concentration. This results in a uniform reduction in interfacial tension along the interface. The surface mass balance in Eq. 2.20 is not applied and $\Gamma^* = \Gamma_{eq}$. Second, if surfactant mass transfer to the interface is much slower than interfacial convection, the adsorptive-desorptive flux to the interface is nearly zero. Thus, the surfactant essentially behaves as an insoluble surfactant which cannot adsorb or desorb from the interface. In this case, the surface mass balance equation in Eq. 2.20 reduces to

$$\frac{\partial \Gamma^*}{\partial t^*} + \nabla_s^* \cdot (\Gamma^* u_t^* \mathbf{t}) + \Gamma^* (\nabla^* \cdot \mathbf{n}) \, u_n^* - D_s \nabla_s^{*2} \Gamma^* = 0, \qquad (2.21)$$

Finally, if surfactant mass transport to the interface is comparable to interfacial convection, the surfactant behaves as a soluble surfactant. Furthermore, if the bulk diffusion of surfactants is fast compared to adsorption/desorption to the interface, the sublayer concentration is always maintained at the bulk concentration value, C_∞. A solution for the surfactant concentration in the bulk is not needed and the surfactant mass transfer is said to be adsorption-desorption limited. The surface mass

balance then becomes

$$\frac{\partial \Gamma^*}{\partial t^*} + \nabla_s^* \cdot (\Gamma^* u_t^* \mathbf{t}) + \Gamma^* (\nabla^* \cdot \mathbf{n}) u_n^* - D_s \nabla_s^{*2} \Gamma^* = \beta_s C_\infty (\Gamma_\infty - \Gamma^*) - \alpha_s \Gamma^*. \quad (2.22)$$

2.2.3 Dimensionless Surfactant Equations

To recast the interfacial mass balance in Eq. 2.22 and the Langmuir equation of state in Eq. 2.18 in dimensionless form, the characteristic quantities l_c, u_c, and l_c/u_c are used to scale the length, velocity, and time. The equilibrium interfacial tension, σ_{eq}, and the equilibrium surfactant concentration at the interface, Γ_{eq}, are chosen to scale the interfacial tension and surfactant concentration at the interface, respectively. The dimensionless Langmuir interfacial equation of state is given by

$$\sigma = \frac{1 + E ln (1 - x\Gamma)}{1 + E ln (1 - x)}. \quad (2.23)$$

The elasticity parameter, E, represents the sensitivity of the interfacial tension to the surfactant concentration, and is given by

$$E = \frac{RT\Gamma_\infty}{\sigma_o}. \quad (2.24)$$

The elasticity parameter for typical surfactants are found to be much less than unity [43]. The equilibrium coverage of surfactants at the interface, x, is given by

$$x = \frac{\Gamma_{eq}}{\Gamma_\infty}. \quad (2.25)$$

Assuming a soluble surfactant in the adsorption-desorption limit, the dimensionless surface mass balance at the interface is then written as

$$\frac{\partial \Gamma}{\partial t} + \nabla_s \cdot (\Gamma u_t \mathbf{t}) + \Gamma (\nabla \cdot \mathbf{n}) u_n - \frac{1}{Pe_s} \nabla_s^2 \Gamma = \frac{Bi}{1-x} (1 - \Gamma). \quad (2.26)$$

The interfacial Peclet number, Pe_s represents the ratio of the interfacial convection rate to the interfacial diffusion rate, and is given by

$$Pe_s = \frac{u_c l_c}{D_s}. \quad (2.27)$$

22

In general, the rate of diffusion is much slower than the rate of convection and for most practical systems $Pe_s \gg 1$. The Biot number, Bi, represents the ratio of the surfactant desorption rate to the interfacial convection rate, and is given by

$$Bi = \frac{\alpha_s l_c}{u_c}. \tag{2.28}$$

For insoluble surfactants, the transport to and from the interface is negligible and $Bi \approx 0$ and the surface mass balance in Eq. 2.26 reduces to

$$\frac{\partial \Gamma}{\partial t} + \nabla_s \cdot (\Gamma u_t \mathbf{t}) + \Gamma (\nabla \cdot \mathbf{n}) u_n - \frac{1}{Pe_s} \nabla_s^2 \Gamma = 0. \tag{2.29}$$

When surfactant transport to the interface is very fast, that is, $Bi \rightarrow \infty$, the interfacial surfactant concentration remains at its equilibrium value, $\Gamma = 1$.

2.3   Modeling Shear-thinning Fluids

Eq. 2.3 describes the deviatoric stress tensor for the fluid used in the momentum equation, Eq. 2.2. For a Newtonian fluid, the viscosity of phase i, μ_i is constant. The subscript $i = 1, 2$ depending on whether the drop fluid or bulk fluid is considered. However, for a shear-thinning fluid, μ_i decreases with increasing shear rate and an appropriate rheological model is needed to describe it. The simplest model for shear-thinning fluids is the power-law rheological model [14] giving the deformation-rate-dependent viscosity function as

$$\mu_i = K_i \left(\dot{\gamma}_i^* \right)^{n_i - 1}. \tag{2.30}$$

Here, K_i is the flow consistency index which is a measure of average viscosity and n_i is the power law exponent which is a measure of deviation from a Newtonian fluid. For shear-thinning fluids n_i has a value less than 1. $\dot{\gamma}_i^*$ is the shear rate or the magnitude of the rate of strain tensor $\dot{\boldsymbol{\gamma}}_i^*$ which is given by

$$\dot{\boldsymbol{\gamma}}_i^* = \nabla^* \mathbf{u}_i^* + \left(\nabla^* \mathbf{u}_i^* \right)^T. \tag{2.31}$$

Thus, the shear rate $\dot{\gamma}_i^*$ is given by

$$\dot{\gamma}_i^* = \sqrt{\frac{1}{2}\left(\dot{\boldsymbol{\gamma}}_i^* : \dot{\boldsymbol{\gamma}}_i^*\right)}.$$ (2.32)

The power-law model is often an inadequate viscosity model since it cannot represent the viscosity for the entire range of shear rates. For example, at zero shear rate, the power-law model predicts an infinite value for viscosity. A group of Carreau-type models have been developed to describe shear-thinning fluids that are capable of predicting the viscosity accurately [21, 29, 61]. In this work, the Carreau model which was first proposed by Pierre Carreau and his coworker [21] will be applied:

$$\mu_i\left(\dot{\gamma}_i^*\right) = (\mu_{i0} - \mu_{i\infty})\left[1 + (\alpha_i\dot{\gamma}_i^*)^2\right]^{\frac{n_i-1}{2}} + \mu_{i\infty}.$$ (2.33)

Here, μ_{i0} is the zero shear-rate viscosity and $\mu_{i\infty}$ is the infinite shear-rate viscosity. α_i is the Carreau time constant and $1/\alpha_i$ gives the characteristic shear rate at which the fluid transitions from behaving as a Newtonian fluid to a pseudoplastic fluid. At low shear rate ($\dot{\gamma}_i^* \ll 1/\alpha_i$), the Carreau fluid behaves as a Newtonian fluid, whereas at high shear rate ($\dot{\gamma}_i^* \gg 1/\alpha_i$), the fluid behaves as a power-law fluid. The Carreau power-law index, n_i takes on values less than 1 for shear-thinning fluids. The Carreau model in Eq. 2.33 can be nondimensionalized by the zero shear-rate viscosity of the bulk fluid, μ_{20}:

$$\mu_i = \bar{\mu}_{i0}\left(1 - \beta_i\right)\left[1 + (\alpha_i\dot{\gamma}_i)^2\right]^{\frac{n_i-1}{2}} + \bar{\mu}_{i0}\beta_i.$$ (2.34)

Here, $\bar{\mu}_{i0} = 1 + (\lambda_0 - 1)\,\delta_{1i}$ and $\lambda_0 = \mu_{10}/\mu_{20}$ gives the zero shear-rate viscosity ratio of drop to bulk fluids. For shear-thinning drop and bulk phases $\lambda = \lambda_0$. $\beta_i = \mu_{i\infty}/\mu_{i0}$ gives the ratio of the infinite shear-rate viscosity to the zero shear-rate viscosity for fluid phase i. α_i and n_i are the Carreau time constant and the Carreau power-law index, respectively. Eq. 2.34 reduces to a Newtonian fluid with $\mu_i = \mu_{i0}$ if $\alpha_i = 0$ or $\beta_i = 0$ or $n_i = 1$. For $n_i < 1$, the fluid is shear-thinning or pseudoplastic while for $n_i > 1$, the fluid is shear-thickening or dilatant.

To guide the choice of the Carreau model parameters used in this study, the effect of changing n_i, β_i, and α_i on the viscosity of the resulting fluid is investigated. The zero shear viscosity is set to $\bar{\mu}_{i0} = 0.9$. The effect of changing the power-law index, n_i, on the apparent fluid viscosity while keeping $\beta_i = 0.2$ and $\alpha_i = 0.5$ is seen in Fig. 2-3. $n_i = 1$ corresponds to a Newtonian fluid with a constant viscosity. For n_i values of 0.5 and 0.3, the fluid exhibits shear-thinning behavior with apparent viscosity decreasing with increasing shear rate as seen in Fig. 2-3. The apparent viscosity decreases more quickly with increasing shear rate as the power-law index decreases from 1 to 0.3 even though eventually both shear-thinning fluids reach the same infinite-shear viscosity. The effect of changing β_i on the apparent viscosity while keeping $n_i = 0.5$ and $\alpha_i = 0.5$ is seen in Fig. 2-4. Decreasing β_i reduces the ratio of the infinite shear-rate viscosity to the zero shear-rate viscosity. $\beta_i = 1$ corresponds to a Newtonian fluid as the zero-shear viscosity is the same as the infinite-shear viscosity. With a lower β_i, the apparent viscosity of the fluid is lower for the same applied shear rate as seen in Fig. 2-4. Finally, the effect of changing α_i from 0 to 10 on the apparent viscosity while keeping $n_i = 0.5$ and $\beta_i = 0.2$ is seen in Fig. 2-5. The Carreau time constant α_i changes the characteristic deformation rate at which the fluid transitions from a Newtonian to a pseudoplastic behavior. $\alpha = 0$ indicates a Newtonian fluid and as α_i increases, the transition to shear-thinning behavior occurs at lower shear rates as seen in Fig. 2-5. As a consequence, for the same shear rate, the viscosity of the shear-thinning fluid with a higher α_i is lower than that of a fluid with a higher α_i even though both fluids reach the same infinite-shear viscosity (same β_i). Based on these observations, two different shear-thinning fluids will be compared to the Newtonian fluid results - a weakly shear-thinning fluid with $\alpha_i = 0.5$, $\beta_i = 0.5$, and $n_i = 0.5$ and strongly shear-thinning fluid with $\alpha_i = 10$, $\beta_i = 0.002$, and $n_i = 0.3$. The viscosity of the shear-thinning fluid as a function of the shear rate for Newtonian,
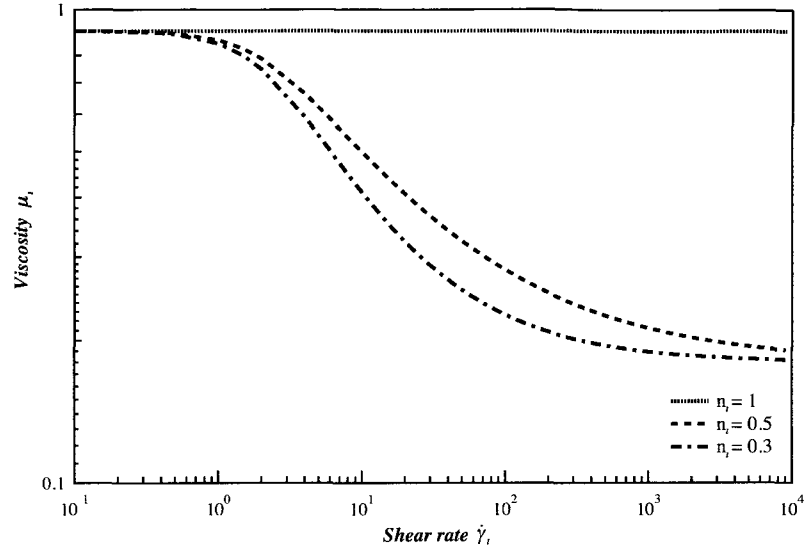
Figure 2-3: Effect of the power-law index n_i on the shear-thinning behavior while keeping $\beta_i = 0.2$ and $\alpha_i = 0.5$.

weakly shear-thinning, and strongly shear-thinning fluids is shown in Fig. 2-6.
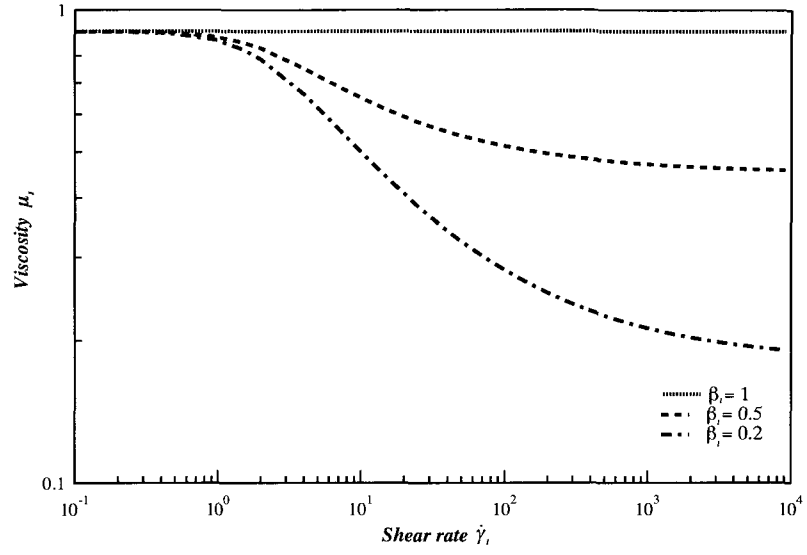
Figure 2-4: Effect of the ratio of the infinite shear-rate viscosity to the zero shear-rate viscosity β_i on the shear-thinning behavior while keeping $n_i = 0.5$ and $\alpha_i = 0.5$.
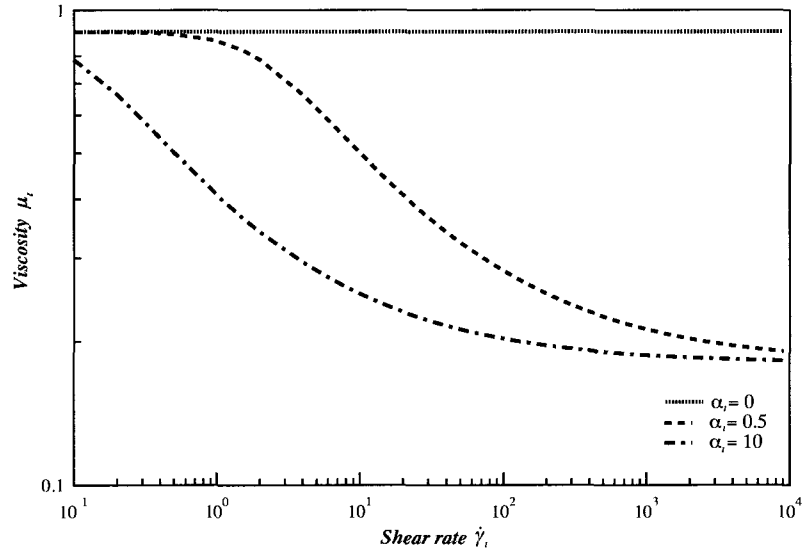
Figure 2-5: Effect of the ratio of the Carreau time constant α_i on the shear-thinning behavior while keeping $n_i = 0.5$ and $\beta_i = 0.2$.
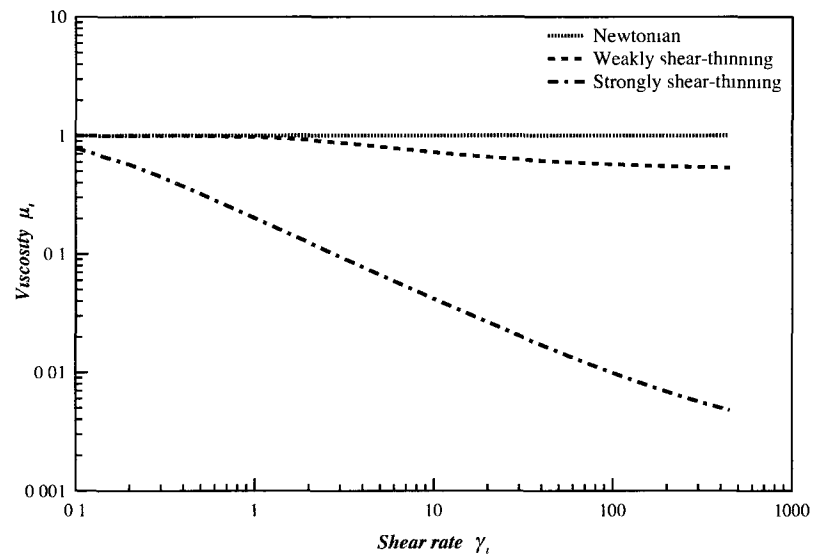
Figure 2-6: The characteristic viscosity as a function of shear rate based on the Carreau model for Newtonian ($n_i = 1$), weakly shear-thinning ($\alpha_i = 0.5$, $\beta_i = 0.5$, and $n_i = 0.5$), and strongly shear-thinning fluids ($\alpha_i = 10$, $\beta_i = 0.002$, and $n_i = 0.3$).

Chapter 3

Numerical Method

Numerical modeling of free surface flows is a challenging task as the location of the interface is not known *a priori* and must be calculated as part of the solution. When surfactants are present in the system, the problem becomes more complex as the flow field affects the distribution of surfactants, which in turn alters the interfacial tension and thus alters the flow field. Numerical modeling is a powerful tool to understand problems with complex effects as it allows one to isolate and explore each effect individually and determine quantities that may be difficult to measure experimentally. For example, the surfactant concentration on an evolving drop interface is challenging to measure experimentally, but can be easily visualized in the analysis of numerical simulation results. The interaction between the flow field and surfactants is highly non-linear and a robust numerical method is needed to accurately represent the interfacial forces on a rapidly expanding deformable interface in the presence surfactants.

3.1   Numerical Methods for Free Surface Flows

Two numerical strategies have been developed to study free boundary problems, moving-grid methods and fixed-grid methods as sketched in Fig. 3-1. In moving-grid methods such as boundary-fitted method, the two fluid phases are discretized

separately and the interface is tracked explicitly as a boundary between two subdomains of the grid. This treatment tracks the exact position of the interface with accurate representation of normals and curvatures at the interface. However, when the interface undergoes large and rapid deformation, this method becomes inefficient and inaccurate. As seen in Fig. 3-1(a), it can give rise to highly distorted element shapes near the highly deformed interface and frequent remeshing is required [111]. In the fixed-grid methods, the grid is predefined and does not move with the interface, and the entire domain is discretized as a single fluid. As seen in Fig. 3-1(b), the interface lies somewhere inside this grid and the position of the interface needs to be determined at every time step. Implementation of the governing equations is straightforward on the fixed grid but strategies are needed to represent the deforming interface. The interface can be represented either by implicitly tracking the location of the interface, also known as front-capturing, or explicitly tracking the location of the interface, also known as front-tracking. Front-capturing schemes allow large deformation but often give inaccurate normals and curvatures since tracking of the interface is not explicit. Front-tracking schemes are more complex to implement but provide accurate descriptions of the interface topology as the interface is tracked explicitly.

Two front-capturing methods, level-set [122] and volume-of-fluid (VOF) [60] methods are most commonly used to implicitly track the interface. The level-set method defines a signed distance function from the interface called the level-set function. The normal and curvature can be readily estimated from the level-set function. An advection scheme is developed for the evolution of the level set function to track the location of the evolving interface. The level-set method has good capability of handling large topology changes of the interface for two-phase flows [121]. The method, however, does not conserve mass well, and the loss of mass gets worse as the simulation time
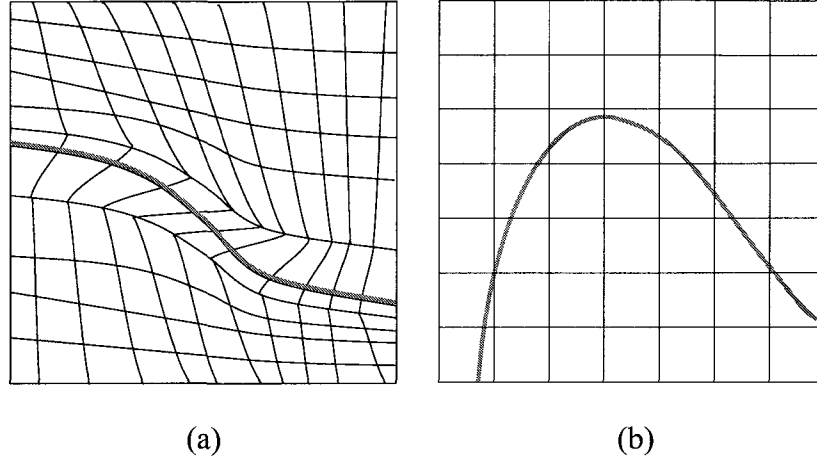
Figure 3-1: Schematic of (a) the moving grid method and (b) the fixed grid method for modeling deformable interface.

proceeds [95]. The VOF method also defines a color function in each cell of the flow domain based on the fraction of the cell occupied by one phase. Knowing only the volume fraction in all the cells in the flow domain, a reconstruction technique is needed to determine the location of the interface [111]. The simplest reconstruction technique is the simple line interface calculation (SLIC) which is a first-order accurate method [87] as seen in Fig. 3-2(a). A more accurate reconstruction technique is the piecewise linear interface construction (PLIC) which is second-order accurate [4] and is seen in Fig. 3-2(b). Again an advection scheme is developed for the evolution of the color function to locate the evolving interface. The main advantage of the VOF method is good mass conservation. It preserves mass in a natural way as a direct result of the development of transport equation of VOF function based on the mass conservation law [111]. It is robust when the curvature is small. For rapidly deforming interfaces, accurate normals and curvature are obtained only for very fine discretization due to the smeared interface reconstruction.
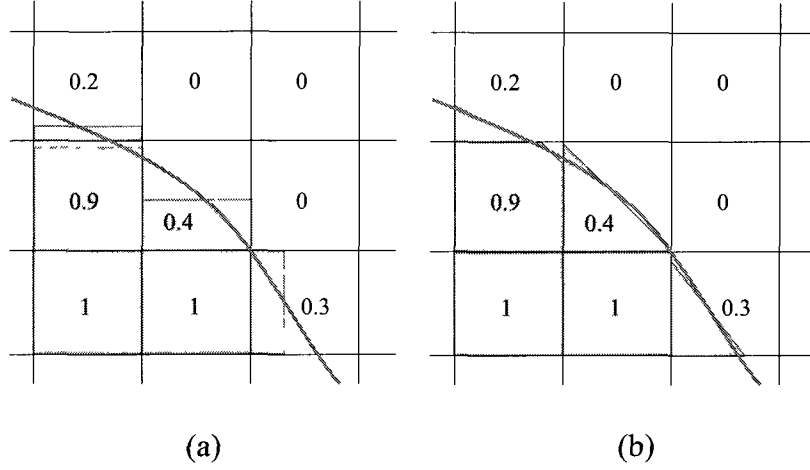
Figure 3-2: Schematic of (a) the first-order or the simple line interface calculation (SLIC) and (b) the second-order or the piecewise linear interface construction.

Tracking methods can be further divided into volume tracking and surface tracking. In volume tracking methods, a representation of the interface is not stored but can be reconstructed as needed. The marker-and-cell method is the simplest form of volume tracking [41]. In this method, massless marker particles identify different fluids and the interface is considered to be somewhere inside a cell that contains marker particles of both fluids. The marker-and-cell method does not determine the location, orientation, normals, or curvature of the interface. In the diffuse-interface method [40] and the immersed boundary method [99], the sharp interface is treated as a smeared interface with nonzero width which has continuous variations of parameters such as density. The surface tracking methods employ interfacial markers to track the location and shape of the interface explicitly [100, 130]. Even though they require larger data storage, they can resolve features of the interface that are smaller than the cell spacing of the fixed grid. Therefore, they can describe the location, orientation, normals, and curvatures of the interface and the interfacial forces

32

accurately. The immersed interface method [75] is an improvement on the immersed boundary method which enforces the discontinuities or the jump conditions exactly or approximately near the interface. It combines with some interface tracking / capturing methods such as surface tracking method and level-set method to describe the information of the interface. A standard finite difference or finite element method is used in discretizing the governing equations away from the interface while the numerical methods are modified according to the jump conditions only on the grid points or elements near or on the interface [78].

3.2 Hybrid VOF Numerical Method

For this work, a hybrid numerical methods based on a volume-of-fluid (VOF) method [54] with a front-tracking scheme [100] is implemented. It combines the mass conservation properties of the VOF method with the accuracy of defining the interface topology and stresses of the front-tracking method. The details of the numerical method for a $3D$-axisymmetric cylindrical co-ordinate system are described in the following sections.

3.2.1 Computational Grids

In this scheme, two computational grids are defined. The Navier-Stokes equations are solved using a VOF method on a fixed Eulerian grid and the interface is tracked by a moving Lagrangian grid as shown in Fig. 3-3. The physical domain is discretized into cells of size Δr and Δz in the $r-$ and $z-$ directions, respectively. In the fixed Eulerian grid, there are two common choices for variable arrangement on each cell: the colocated arrangement and the staggered arrangement. For a colocated arrangement, the pressure and velocities are defined at the center of the cell. For the

33

staggered arrangement, the pressure and velocities are defined at the center and the walls of the cell. A staggered arrangement of the pressure and velocity components on a single cell is shown in Fig. 3-4. The pressure, P is defined at the center of the cell, but the radial component of velocity, u_r and the axial component of velocity, u_z are defined along the cell boundary faces. The discretized forms of the governing equations are then implemented on different control volumes as shown in Figs. 3-4(a-c) depending on whether the equations are used for the evolution of pressure or the velocity components. For example, the $z-$component of the momentum equation is discretized on a control volume centered on u_z shown as the shaded region in Fig. 3-4(b). In this research, a staggered arrangement of the velocity and pressure fields is adopted because it prevents the occurrence of oscillations observed in the colocated arrangement.

The interface is represented by Lagrangian marker particles with a parametric representation $(r_s(s),\ z_s(s))$ where s is the arc length starting from the apex of the drop. The outward pointing unit normal and unit tangent to the interface and the curvature of the interface at any location on the interface are then given by

$$\mathbf{n} = -z_s'\mathbf{e_r} + r_s'\mathbf{e_z}, \tag{3.1}$$

$$\mathbf{t} = r_s'\mathbf{e_r} + z_s'\mathbf{e_z}, \tag{3.2}$$

$$\nabla \cdot \mathbf{n} = -\frac{z_s''}{r_s'} - \frac{z_s'}{r}, \tag{3.3}$$

where r_s' and z_s' represent the first derivatives of r_s and z_s with respect to the arclength s while z_s'' represents the second derivative of z_s with respect to s.

3.2.2 Single-fluid VOF Formulation

By applying the idea of the VOF method, the two fluids with different densities and viscosities are treated as a single fluid with varying density $\bar{\rho}$ and viscosity $\bar{\mu}$. The
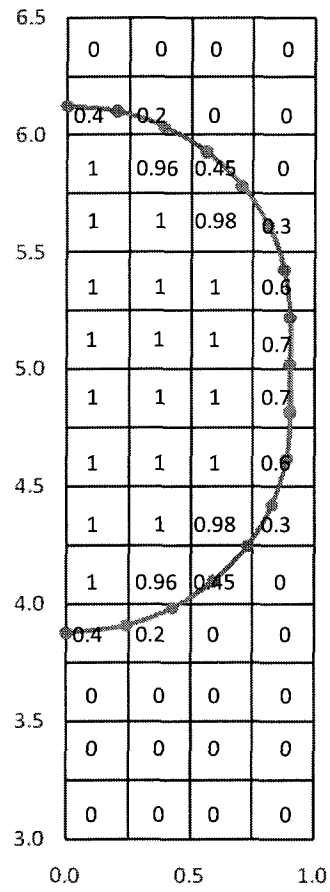
Figure 3-3: Schematic of the fixed Eulerian grid and the moving Lagrangian grid for solving two-phase free boundary problems.
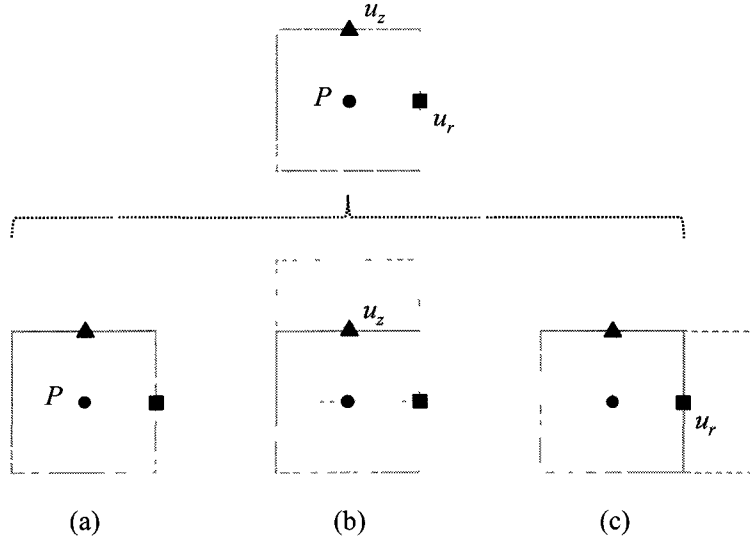
Figure 3-4: Schematic of the staggered arrangement on a grid cell, and the control volumes used for implementing the governing equations for (a) pressure, (b) axial velocity, and (c) radial velocity.

method keeps track of the fluid properties by using a VOF function, ϕ, which gives the volume fraction of drop phase in the grid cell shown in Fig. 3-5. If the cell is completely in the drop phase, the VOF function has a value of 1 and if the cell is completely in the bulk phase, the VOF function has a value of 0. For a cell with a two-phase interface, the VOF function has a value between 0 and 1 depending on how much fraction of the cell is occupied by the drop phase. A continuous surface force (CSF) method [19] is adopted to express the interfacial stress jump with an interfacial delta function, δ_s, which takes the value 1 at the interface and 0 everywhere else. The CSF method treats interfacial tension as a continuous, three-dimensional effect across the interface, instead of a boundary condition at the interface. In this way, the interfacial boundary condition in Eq. 2.5 is incorporated into the momentum equation, Eq. 2.2 to obtain the single-fluid VOF. A detailed derivation of the single-fluid VOF formulation in dimensionless form is shown in Appendix A and the final
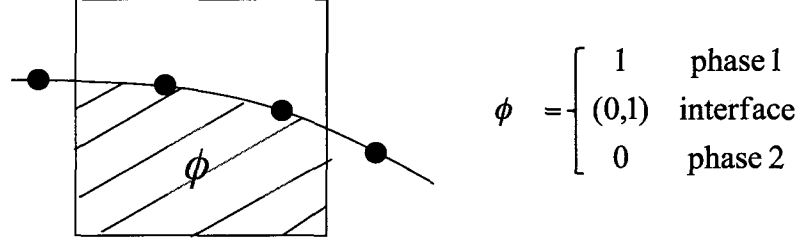
Figure 3-5: Schematic of the volume-of-fluid (VOF) function ϕ with an interface represented by moving Lagrangian markers is across the fixed Eulerian grid.

form is shown here:

$$\nabla \cdot \mathbf{u} = 0, \tag{3.4}$$

$$\bar{\rho} Re \left(\frac{\partial \mathbf{u}}{\partial t} + \mathbf{u} \cdot \nabla \mathbf{u} \right) = -\nabla P + \nabla \cdot \left(\bar{\mu} \left[(\nabla \mathbf{u}) + (\nabla \mathbf{u})^T \right] \right)$$
$$+ \frac{1}{Ca} \left[\nabla_s \sigma - \sigma \mathbf{n} \left(\nabla \cdot \mathbf{n} \right) + Bozn \right] \delta_s. \tag{3.5}$$

Here, $\bar{\rho} = 1 - (1 - \chi) \phi$ and $\bar{\mu} = 1 - (1 - \lambda) \phi$, with $\chi = \rho_1/\rho_2$ and $\lambda = \mu_1/\mu_2$ representing the density and viscosity ratio of drop to bulk fluids, respectively.

3.2.3 Solution of the Governing Equations

Several techniques have been developed to solve the continuity and momentum equations. In this study of unsteady flow problems, a time-splitting method is implemented to solve the incompressible mass and momentum equations for velocity and pressure fields. It introduces an intermediate velocity field, $\mathbf{u}^{**}$, that does not have

37

to be divergence-free. The single-fluid VOF formulation in Eq. 3.5 is split into two equations to solve for the velocity, $\mathbf{u}^{n+1}$, and pressure, P^{n+1}, at the new time step $n+1$ as

$$\bar{\rho}Re\left(\frac{\mathbf{u}^{**} - \mathbf{u}^n}{\Delta t}\right) = -\bar{\rho}Re\left(\mathbf{u}^{n+1} \cdot \nabla \mathbf{u}^{n+1}\right) + \nabla \cdot \left(\bar{\mu}\left[\left(\nabla \mathbf{u}^{n+1}\right) + \left(\nabla \mathbf{u}^{n+1}\right)^T\right]\right)$$

$$+\frac{1}{Ca}\left[\nabla_s \sigma^n - \sigma^n \mathbf{n}\left(\nabla \cdot \mathbf{n}\right) + Bo z \mathbf{n}\right]\delta_s, \quad (3.6)$$

$$\bar{\rho}Re\left(\frac{\mathbf{u}^{n+1} - \mathbf{u}^{**}}{\Delta t}\right) = -\nabla P^{n+1}. \quad (3.7)$$

To ensure that $\mathbf{u}^{n+1}$ is divergence-free, that is, $\nabla \cdot \mathbf{u}^{n+1} = 0$, taking the divergence of Eq. 3.7 gives the pressure Poisson equation,

$$\bar{\rho}Re\left(\frac{-\nabla \cdot \mathbf{u}^{**}}{\Delta t}\right) = -\nabla^2 P^{n+1}. \quad (3.8)$$

Here, the superscripts n and $n+1$ refer to the successive time steps. The velocity field at the nth time step, $\mathbf{u}^n$, is used to solve for the intermediate velocity, $\mathbf{u}^{**}$ from Eq. 3.6. Then the pressure Poisson equation, Eq. 3.8, is solved to get pressure field at the $(n+1)^{st}$ time step. Finally, the divergence-free velocity field at the $(n+1)^{st}$ time step, $\mathbf{u}^{n+1}$ is obtained from Eq. 3.7. Eqs. 3.6 - 3.8 are solved iteratively at each time step to solve for $\mathbf{u}^{n+1}$ and P^{n+1}.

3.2.4 Differencing Scheme

To solve for the pressure and velocity fields at each time step, the differential equations in Eqs. 3.6 - 3.8 are discretized in the computational domain. In this study, the governing equations are discretized using a finite volume method, which has first-order accuracy in time and second-order accuracy in space on the fixed Eulerian grid. For the temporal discretization, a first-order backward Euler differencing scheme is used in the time-splitting method. In the finite volume method, the governing equations are integrated over control volumes around the computational nodes and time [47].

For example, the $r-$ component of Eq. 3.6 would be integrated on a control volume between the co-ordinates, r and $r + \Delta r$ and z and $z + \Delta z$ and times t and $t + \Delta t$ as

$$\int_t^{t+\Delta t} \int_r^{r+\Delta r} \int_z^{z+\Delta z} \{\bar{\rho} Re \frac{\partial u_r}{\partial t}\} 2\pi r dr dz dt$$

$$= \int_t^{t+\Delta t} \int_r^{r+\Delta r} \int_z^{z+\Delta z} \{-\bar{\rho} Re u_r \frac{\partial u_r}{\partial r} - \bar{\rho} Re u_z \frac{\partial u_r}{\partial z} + \frac{\partial}{\partial r} \left(\frac{\bar{\mu}}{r} \frac{\partial}{\partial r} (r u_r) \right) $$

$$+ \frac{\partial}{\partial z} \left(\bar{\mu} \frac{\partial u_r}{\partial z} \right) + \frac{1}{Ca} [\nabla_s \sigma - \sigma \mathbf{n} (\nabla \cdot \mathbf{n}) + Bozn] \mathbf{e}_r \delta_s\} 2\pi r dr dz dt. \qquad (3.9)$$

where $\frac{\partial u_r}{\partial t}$ is discretized as $\frac{u_r^{**} - u_r^n}{\Delta t}$. The first-order partial derivatives with respect to spatial coordinate r or z are estimated by the central differencing scheme with second-order accuracy. For example,

$$\frac{\partial u_r}{\partial r} = \frac{u_r(i+1, j) - u_r(i-1, j)}{2\Delta r} + O \left((\Delta r)^2 \right). \qquad (3.10)$$

Here, i and j denote the indices for $r-$ and $z-$ directions, Δr is the unit discretization length for $r-$ direction, and $O \left((\Delta r)^2 \right)$ is the second-order truncation error. Similarly, the second-order partial derivatives with respect to r or z are estimated by the differencing scheme with second-order accuracy. For example,

$$\frac{\partial^2 u_r}{\partial z^2} = \frac{u_r(i, j+1) - 2u_r(i, j) + u_r(i, j-1)}{2\Delta z} + O \left((\Delta z)^2 \right), \qquad (3.11)$$

where Δz is the unit discretization length for $z-$ direction. Sometimes an average operation is needed to estimate quantities at the specific point using the corresponding values in the surrounding cells.

3.2.5 Interfacial Stress Term

Accurate evaluation of the interfacial stress term, the last term of Eq. 3.9, is critical for the success of the proposed numerical method. To compute this term on a computational cell containing the interface as seen in Fig. 3-6, the volume integral

39

with respect to r and z is first converted into a surface integral with respect to arclength s as

$$\int_t^{t+dt} \int_r^{r+dr} \int_z^{z+dz} \{\frac{1}{Ca} [\nabla_s \sigma - \sigma \mathbf{n} (\nabla \cdot \mathbf{n}) + Bozn] \mathbf{e_r} \delta_s\} \, 2\pi r dr dz dt$$

$$= \int_t^{t+dt} \int_{s_A}^{s_B} \{\frac{1}{Ca} [\nabla_s \sigma - \sigma \mathbf{n} (\nabla \cdot \mathbf{n}) + Bozn] \mathbf{e_r}\} \, 2\pi r ds dt. \qquad (3.12)$$

Here, s_A and s_B represent the arclengths of the start and end points of the interface that cross a cell as shown in Fig. 3-6. Since the interface is represented by Lagrangian marker particles with parametric representation, (r_s, z_s), the normal, tangent, and curvature of the interface are known along the interface. In surfactant-free systems, the interfacial tension along the interface is 1 and the Marangoni stress term, $\nabla_s \sigma$ is zero. In surfactant-laden systems, a parametric representation of the interfacial tension, $\sigma(s)$ can also be written such that $\nabla_s \sigma = \sigma' \mathbf{t}$, where σ' is the first derivative of σ with respect to the arc length, s. Eq. 3.12 can then be further reduced to

$$\int_t^{t+dt} \int_{s_A}^{s_B} \{\frac{1}{Ca} [\nabla_s \sigma - \sigma \mathbf{n} (\nabla \cdot \mathbf{n}) + Bozn] \mathbf{e_r}\} \, 2\pi r ds dt$$

$$= \frac{2\pi \Delta t}{Ca} \int_{s_A}^{s_B} \{\sigma' r_s r_s' + \sigma r_s r_s'' - \sigma (z_s')^2 - Bor_s z_s z_s'\} ds. \qquad (3.13)$$

3.2.6 Solution of Discretized Equations

Discretization of the governing equations on the computational cells results in a system of linear equations. For example, when discretizing the pressure Poisson equation (Eq. 3.8) on a single cell centered around $P_{i,j}$ using a central difference scheme can be rearranged to give

$$A_s^{i,j} P_{i,j-1} + A_w^{i,j} P_{i-1,j} + A_p^{i,j} P_{i,j} + A_e^{i,j} P_{i+1,j} + A_n^{i,j} P_{i,j+1} = Q^{i,j}. \qquad (3\ 14)$$

These equations for all i and j can be written as a system of linear equations of the form $\mathbf{AP} = \mathbf{Q}$ to solve for the pressure solution vector, $\mathbf{P}$. The sparse square
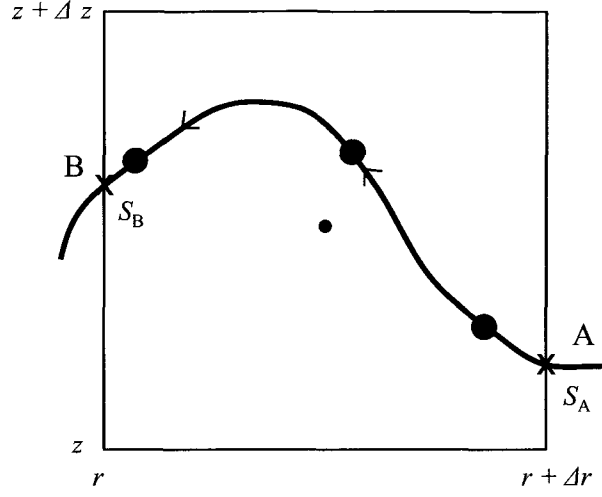
Figure 3-6: Schematic of the Lagrangian grid intersecting the Eulerian grid at points A and B.

coefficient matrix A has non-zero elements only on the main diagonal, the two neighboring diagonals, and the two other diagonals removed by N positions from the main diagonal where N is the number of computational nodes in one direction. Q is the discretized right-hand side of Eq. 3.8. A successive over-relaxation (SOR) scheme is employed to solve for pressure field. The SOR method is an accelerated version of the Gauss-Seidel method developed for solving linear sparse large systems [47]. The iterative SOR structure of Eq. 3.14 can be written as

$$P_{i,j}^{k+1} = \omega \frac{Q^{i,j} - A_s^{i,j} P_{i,j-1}^{k+1} - A_w^{i,j} P_{i-1,j}^{k+1} - A_n^{i,j} P_{i,j+1}^k - A_e^{i,j} P_{i+1,j}^k}{A_p^{i,j}} + (1-\omega) P_{i,j}^k, \quad (3.15)$$

where k and $k+1$ are successive iterative steps. ω is the over-relaxation factor such that if $\omega = 1$, the SOR method is reduced to the Gauss-Seidel method.

3.3 Interface Tracking

The velocity field calculated on the Eulerian grid is used to advect the marker particles on the Lagrangian interfacial grid. The location of the drop interface is given by (r_s, z_s), parameterized by the arclength s measured from the drop apex. The marker particles are advected as material particles based on the kinematic condition shown in dimensionless form as

$$\frac{d\mathbf{x}_s}{dt} = \mathbf{u}_s,$$ (3.16)

where $\mathbf{x}_s$ is the location of the interface and $\mathbf{u}_s$ is the interfacial velocity which can be expressed as

$$\mathbf{x}_s = r_s\mathbf{e_r} + z_s\mathbf{e_z},$$ (3.17)

$$\mathbf{u}_s = u_{s,r}\mathbf{e_r} + u_{s,z}\mathbf{e_z} = u_n\mathbf{n} + u_t\mathbf{t},$$ (3.18)

where u_n and u_t are the normal and tangential components. The velocities of the marker particles on the moving grid (u_{sr}, u_{sz}) at the interface can be determined by employing a bilinear interpolation based on the velocity fields obtained on the fixed grid (u_r, u_z). The bilinear interpolation is a $2D$ extension of linear interpolation for interpolating functions of two variables. For example, to estimate the velocities of the mth marker on the moving grid at ($r_{s,m}, z_{s,m}$) which is to be determined, the bilinear interpolation formulation is as below:

$$g_{s,m} = \frac{(r_{i+1,j} - r_{s,m})(z_{i,j+1} - z_{s,m})}{(r_{i+1,j} - r_{i,j})(z_{i,j+1} - z_{i,j})} f_{i,j} + \frac{(r_{s,m} - r_{i,j})(z_{i,j+1} - z_{s,m})}{(r_{i+1,j} - r_{i,j})(z_{i,j+1} - z_{i,j})} f_{i+1,j}$$
$$+ \frac{(r_{s,m} - r_{i,j})(z_{s,m} - z_{i,j})}{(r_{i+1,j} - r_{i,j})(z_{i,j+1} - z_{i,j})} f_{i+1,j+1} + \frac{(r_{i+1,j} - r_{s,m})(z_{s,m} - z_{i,j})}{(r_{i+1,j} - r_{i,j})(z_{i,j+1} - z_{i,j})} f_{i,j+1}, \quad (3.19)$$

where g_s represents the velocity of the marker particle, u_{sr} or u_{sz} and f represents the corresponding velocity of the surrounding Eulerian grid nodes, u_r or u_z.

Next, the normal and tangential velocities of the interface, u_n and u_t for any

42
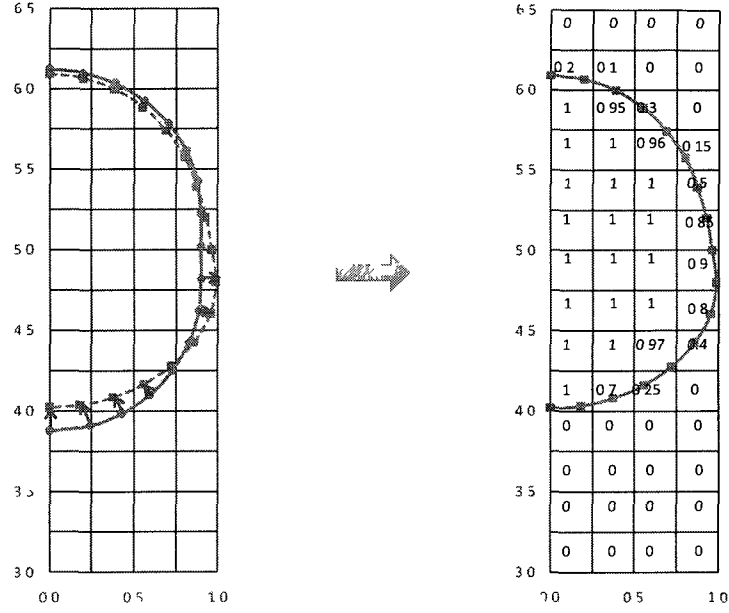
Figure 3-7: Schematic of advection of the interface marker particles to the new locations and the updated interface shape with the updated ϕ field.

marker particle can be calculated by

$$u_n = \mathbf{u}_s \cdot \mathbf{n} = -z_s' u_{s,r} + r_s' u_{s,z}, \qquad (3.20)$$

$$u_t = \mathbf{u}_s \cdot \mathbf{t} = -r_s' u_{s,r} + z_s' u_{s,z}. \qquad (3.21)$$

Finally, the new interface location $(r_s^{n+1},\ z_s^{n+1})$ at the $(n+1)^{st}$ time step can be determined based on the old interface location $(r_s^n,\ z_s^n)$ and normal and tangential velocities at the nth time step. This is done using the kinematic conditions in Eq. 3.16 and Eq. 3.18 and an explicit Euler scheme,

$$r_s^{n+1} = r_s^n + \Delta t \left(r_s' u_t - z_s' u_n \right)^n, \qquad (3.22)$$

$$z_s^{n+1} = z_s^n + \Delta t \left(r_s' u_n + z_s' u_t \right)^n. \qquad (3.23)$$

This is schematically shown in Fig. 3-7.

43

3.3.1 Remeshing the Interface

As the simulation proceeds, marker particles come close together in regions where the interface is contracting and move very far apart where the interface is expanding. Furthermore, for processes such as drop formation, the interface is rapidly expanding and the initial number of marker particles is not sufficient. To keep the discretization of the interface relatively uniform throughout the evolution of the interface, the interface is remeshed at each time step and marker particles are added or deleted to maintain the same level of discretization Δs. To do this the interface locations $(r_s(s), z_s(s))$ are represented by cubic spline functions,

$$r_s(s) = ar(1) s^3 + ar(2) s^2 + ar(3) s + ar(4), \qquad (3.24)$$

$$z_s(s) = az(1) s^3 + az(2) s^2 + az(3) s + az(4), \qquad (3.25)$$

where $ar(i)$ and $az(i)$ are the constant polynomial coefficients for r_s and z_s, respectively. Using cublic spline interpolation, the marker particles can be added or redistributed to maintain a homogeneous distribution of marker particles along the interface. The cubic splines are also used to accurately determine the first and second derivatives of r_s and z_s along the interface to calculate the normals, tangents, and curvatures [101].

3.3.2 Surfactant Systems

In the presence of surfactants, the interfacial surfactant concentration $\Gamma(s)$ and the interfacial tension $\sigma(s)$ are also determined along the interface. The surfactant mass balance in Eq. 2.26 is used to update the surfactant concentration $\Gamma(s)$ and interfacial tension $\sigma(s)$ is determined using the Langmuir equation of state in Eq. 2.23. Similar to Eq. 3.24 and Eq. 3.25 at a certain time t, Γ and σ are also represented by cubic

splines as

$$\Gamma\left(s\right) = ag\left(1\right)s^3 + ag\left(2\right)s^2 + ag\left(3\right)s + ag\left(4\right), \tag{3.26}$$

$$\sigma\left(s\right) = as\left(1\right)s^3 + as\left(2\right)s^2 + as\left(3\right)s + as\left(4\right), \tag{3.27}$$

where $ag(i)$ and $as(i)$ are the constant polynomial coefficients for Γ and σ, respectively. The surfactant mass balance equation in Eq. 2.26 can be discretized along the interface using a finite difference formulation. The temporal term is discretized using backward Euler differencing scheme while second-order accurate central differencing schemes are used for the spatial discretizations. The partial differential equation in Eq. 2.26 is then converted into algebraic equations that can be written in a general tri-diagonal matrix form after rearrangement as

$$a_i\Gamma_{i-1}^{n+1} + b_i\Gamma_i^{n+1} + c_i\Gamma_{i+1}^{n+1} = r_i^n, \tag{3.28}$$

where a, b, and c denote the elements of the sub-diagonal, diagonal and super-diagonal. This matrix is solved using the tri-diagonal matrix algorithm [101]. The initial dimensionless surfactant concentration at any Lagrangian marker along the interface is set to be 1, that is, the initial dimensional surfactant concentration is equal to the equilibrium surfactant concentration. At the first and last marker particles, $\partial\Gamma/\partial s = 0$ are applied as the boundary conditions to solve the surfactant mass balance equation at each time step.

3.3.3 Shear-thinning Fluids

If either of the phases is shear-thinning, the Carreau model is used to describe the viscosity of the fluid. Both drop and bulk phases in the two-phase flows can be treated as Carreau shear-thinning fluids with the viscosities expressed by Eq. 2.34.

45

In the cylindrical co-ordinate system, the dimensionless shear rate, $\dot{\gamma}_i$ is expressed as

$$\dot{\gamma}_i = \sqrt{2\left(\frac{\partial u_{ri}}{\partial r}\right)^2 + 2\left(\frac{u_{ri}}{r}\right)^2 + 2\left(\frac{\partial u_{zi}}{\partial z}\right)^2 + \left(\frac{\partial u_{ri}}{\partial z} + \frac{\partial u_{zi}}{\partial r}\right)^2}. \qquad (3.29)$$

The first derivatives are estimated using a second-order accurate differencing scheme.

3.4 Solution Algorithm

An iterative procedure is used to simulate two-phase flow problems using the hybrid VOF technique.

1. A fixed Eulerian grid is generated for the complete flow domain.

2. An initial drop shape is assumed and the interface is represented by Lagrangian marker particles. The initial volume of function, ϕ is calculated based on the initial interface shape.

3. The interfacial stress terms acting on the cells containing the interface are calculated using Eq. 3.13. For the shear-thinning case, the viscosities in the domain are updated using the Carreau model.

4. The velocity and pressure on the fixed grid are solved at the given time step based on the discretized form of the single-fluid VOF formulation using the time-splitting method, Eqs. 3.6 to 3.8.

5. The marker particles are advected with the velocities interpolated from the velocity field on the fixed grid. The shape is updated and the new VOF function, ϕ is calculated for the new shape. If surfactants are present, the surfactant concentration and the surface tension are updated using the surfactant mass balance and the equation of state.

46

6. The interface is remeshed to maintain the same level of discretization.

7. Steps 3 to 6 are repeated until the end of simulation is reached, that is, the drop breaks for the drop formation process or the drop reaches a steady state for the drop rising process.

The Eulerian and Lagrangian mesh sizes and time step are chosen to ensure convergence of drop shape, velocity and pressure fields for a chosen set of dimensionless parameters. For most of the simulation results presented in this study, a mesh size of at least 0.025 and a time step of at least 10^{-4} are used. Smaller mesh sizes and time steps are sometimes needed to obtain a converged solution.

Chapter 4

Drop Formation in Co-flowing

Fluids

Microfluidic devices are miniaturized systems which consume very small quantities of samples/reagents, require much less time for operation, and are easier to automate and control. Several applications of microfluidic technology such as inkjet printing, microcapsule fabrication, microarraying, and screening and diagnosis require generation and dispensing of drops of controlled size [123]. Several strategies have been developed using microfluidics to generate monodisperse drops in an immiscible ambient fluid [9]. The simplest way to generate uniform drops involves injecting a liquid at a constant flow rate through an orifice [37, 66, 67, 81] or a needle [88, 138, 139, 147] into a quiescent fluid. A co-flowing stream of immiscible fluid at a constant flow rate is often used to generate smaller monodisperse drops [22, 30, 55, 62, 63, 64, 65, 82, 88, 120, 129, 131, 132, 134, 147, 149]. Further reduction in drop size can be achieved by flow focusing where an orifice is placed downstream of the co-flowing geometry [2, 48, 49]. As the co-flowing geometry is easy to build and implement for drop formation with far-reaching impact in microfluidics technology, it is a good flow type to choose for this study.

4.1 Model Problem

The co-flowing system of two immiscible viscous fluids is illustrated in Fig. 4-1. An axisymmetric drop of density ρ_1 and viscosity μ_1 is formed at the tip of an inner tube of inner radius R_1 with the inner fluid flowing at a constant flow rate Q_1. The outer fluid of density ρ_2 and viscosity μ_2 flows at a constant flow rate Q_2 in a concentric cylindrical tube of inner radius R_2. The length and width of the inner tube are represented by L_n and W_n respectively. The subscripts 1 and 2 are used to denote parameters corresponding to the inner and outer fluids/tubes, respectively. Both phases are treated as incompressible Newtonian fluids. The flow field is described in a cylindrical coordinate system (r^*, z^*). The location of the drop interface is parameterized by the arc length s^* measured from the drop apex. The gravitational vector $\mathbf{g} = -g\mathbf{e}_z$, points in the negative $z-$direction. It is assumed that both the inner and outer fluids flow in at the inlet $(z^* = 0)$ with fully developed laminar flow profiles.

The numerical model presented in Chapters 2 and 3 are implemented to study the process of drop formation at the tip of a needle in the presence of a co-flowing stream. Specifically, the numerical model will be used to:

- predict the effect of fluid properties, geometry, and flow conditions on drop size at breakup and the breakup time,

- determine how surfactants adsorbed at the drop interface affect the drop formation process by investigating the effects of surfactant mass transfer, the equilibrium interfacial coverage, and the adsorption-desorption kinetics, and

- investigate the effects of a shear-thinning drop fluid rheology on the drop formation process in co-flowing fluids.
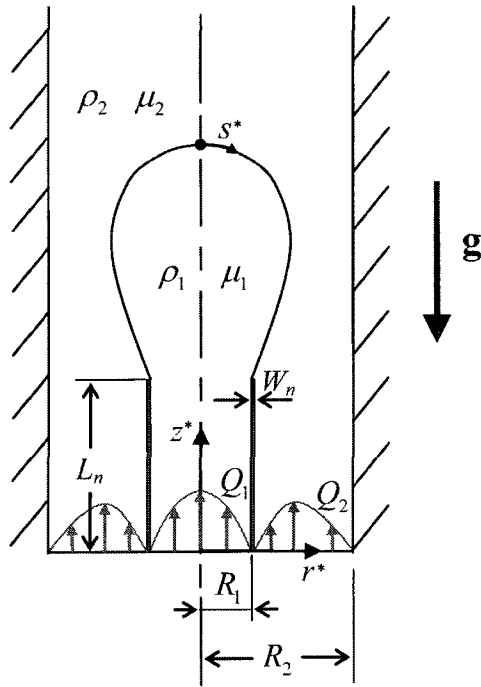
Figure 4-1: Schematic of the drop formation process from the tip of an inner tube in an immiscible co-flowing outer fluid.

In Section 4.1, the modification to the mathematical formulation presented in Chapter 2 to solve the drop formation problem is discussed. The numerical algorithm used to obtain the solution is presented in Section 4.3. The current state of knowledge for the co-flowing flow problem is discussed in Section 4.4 and the results of this work are presented in Section 4.5.

4.2 Mathematical Formulation

As seen in Fig. 4-1, the flow domain is axisymmetric about the z–axis and the solution is obtained for the fluid on one rz–plane with the bounds $0 \leq r^* \leq R_2$ and $0 \leq z^* \leq Z_{max}$. Z_{max} is chosen such that the axial length of the simulation domain does not affect the results. The two-phase flow is governed by the mass and momentum conservation equations given by Eqs. 2.1 - 2.3. If either phase is non-Newtonian, the Carreau model in Eq. 2.33 is used to describe the viscosity of the shear-thinning fluid. In the presence of surfactants, the Langmuir interfacial equation of state in Eq. 2.18 is applied to describe the relationship between the local interfacial tension σ^* and local surfactant interfacial concentration Γ^*. The convective-diffusion equation in Eq. 2.22 is used to solve for the local surfactant concentration Γ^*. The governing equations are solved subject to initial conditions and boundary conditions prescribed at the fluid domain boundaries and the two-phase interface. Initially, the drop is described by a hemispherical interface at the tip of the inner tube. If surfactants are present, the initial surfactant concentration at the interface is set equal to the equilibrium interfacial concentration, that is, $\Gamma^* = \Gamma_{eq}$ along the drop interface.

The boundary conditions imposed at the two-phase interface are described in Eqs. 2.4 - 2.6. In addition, boundary conditions at the flow domain boundaries are

51

needed. It is assumed that the drop fluid entering the inner tube at $z^* = 0$ is laminar and fully developed given by

$$\left.\begin{array}{l} u_{1r}^* = 0 \\[2mm] u_{1z}^* \left(r^*\right) = \frac{2Q_1}{\pi R_1^2}\left[1 - \left(\frac{r^*}{R_1}\right)^2\right] \end{array}\right\} \text{ at } z^* = 0, 0 \leq r^* \leq R_1. \qquad (4.1)$$

Similarly, a fully developed laminar flow is assumed for the outer bulk phase in the outer tube at the tube entrance, that is,

$$\left.\begin{array}{l} u_{2r}^* = 0 \\[2mm] u_{2z}^* \left(r^*\right) = \frac{2Q_2}{\pi\left(R_2^2 - R_1^2\right)}\dfrac{1 - \left(\frac{r^*}{R_2}\right)^2 + \frac{1-(R_1/R_2)^2}{ln(R_2/R_1)}ln\left(\frac{r^*}{R_2}\right)}{1 + \frac{R_1}{R_2} - \frac{1-(R_1/R_2)^2}{ln(R_2/R_1)}} \end{array}\right\} \text{ at } z^* = 0, R_1 \leq r^* \leq R_2. \qquad (4.2)$$

At $z^* = 0$, zero pressure gradient is prescribed,

$$\frac{\partial P^*}{\partial z^*} = 0. \qquad (4.3)$$

At the solid tube walls, no-slip and impermeable boundary conditions are applied,

$$\mathbf{u}_i^* = 0, \qquad (4.4)$$

$$\frac{\partial P^*}{\partial r^*} = \frac{\partial P^*}{\partial z^*} = 0. \qquad (4.5)$$

The contact line is assumed to be pinned at the inner edge of the inner tube. Along the central axis ($r^* = 0$), a symmetry boundary condition is applied along the central axis giving

$$\frac{\partial \mathbf{u}_i^*}{\partial r^*} = 0, \qquad (4.6)$$

$$\frac{\partial P^*}{\partial r^*} = 0. \qquad (4.7)$$

Finally, far downstream at $z^* = Z_{max}$, zero gradients of velocity and pressure are prescribed, that is,

$$\frac{\partial \mathbf{u}_i^*}{\partial z^*} = 0, \qquad (4.8)$$

$$\frac{\partial P^*}{\partial z^*} = 0. \qquad (4.9)$$

52

For non-dimensionalizing the governing equations, the inner tube radius R_1 is chosen for l_c and the average velocity of the inner flow $U_1 = Q_1/\pi R_1^2$ is chosen for u_c. The clean interfacial tension, σ_o, in the surfactant-free case or the equilibrium interfacial tension, σ_{eq}, for the surfactant-laden case is chosen for σ_c. The dimensionless governing equations are then given by Eqs. 2.7 and 2.8 defined between $0 \leq r \leq R_2/R_1$ and $0 \leq z \leq Z_{max}/R_1$. The dimensionless interfacial boundary conditions are given by Eq.s 2.10 - 2.12. The Reynolds, capillary, and Bond numbers are then defined as

$$Re = \rho_2 U_1 R_1/\mu_2, \tag{4.10}$$

$$Ca = \mu_2 U_1/\sigma_c, \tag{4.11}$$

$$Bo = (\rho_2 - \rho_1)g R_1^2/\sigma_c. \tag{4.12}$$

If either phase is non-Newtonian, the dimensionless Carreau model in Eq. 2.34 is used to describe the viscosity of the shear-thinning fluid. In the presence of surfactants, Eqs. 2.26 and 2.23 are applied to determine the local interfacial tension along the interface, Γ. The surface Peclet number and the Biot number are then defined as

$$Pe_s = \frac{U_1 R_1}{D_s}, \tag{4.13}$$

$$Bi = \frac{\alpha_s R_1}{U_1}. \tag{4.14}$$

The elasticity number and equilibrium surface coverage have the same definition as Eqs. 2.24 and 2.25.

The dimensionless velocity boundary conditions at the entrance of the inner and outer tubes at $z = 0$ are given by

$$\left.\begin{array}{l} u_{1r} = 0 \\ u_{1z}(r) = 2(1-r)^2 \end{array}\right\} \text{at } z = 0, 0 \leq r \leq 1, \tag{4.15}$$

$$u_{2r} = 0$$

$$\left.\begin{array}{l} u_{2r} = 0 \\[2mm] u_{2z}(r) = 2\left(\dfrac{Q_2}{Q_1}\right)\dfrac{1}{(R_2/R_1)^2-1}\dfrac{1-r^2\left(\frac{R_1}{R_2}\right)^2+\frac{1-(R_1/R_2)^2}{ln(R_2/R_1)}ln\left(r\left(\frac{R_1}{R_2}\right)\right)}{1+\frac{R_1}{R_2}-\frac{1-(R_1/R_2)^2}{ln(R_2/R_1)}} \end{array}\right\} \text{ at } z = 0, 1 \le r \le R_2/R_1.$$

$$(4.16)$$

At the solid tube walls,

$$\mathbf{u} = 0, \qquad (4.17)$$

$$\frac{\partial P}{\partial r} = \frac{\partial P}{\partial z} = 0. \qquad (4.18)$$

Far downstream at $z = Z_{max}/R_1$,

$$\frac{\partial \mathbf{u}}{\partial z} = 0, \qquad (4.19)$$

$$\frac{\partial P}{\partial z} = 0. \qquad (4.20)$$

At the symmetry axis at $r = 0$,

$$\frac{\partial \mathbf{u}}{\partial r} = 0, \qquad (4.21)$$

$$\frac{\partial P}{\partial r} = 0. \qquad (4.22)$$

4.3 Solution Procedure

The hybrid VOF technique discussed in Chapter 3 is now modified and applied to solve the problem of drop formation in co-flowing fluids. An initially hemispherical drop shape is assumed at the needle tip with an equilibrium concentration of surfactant, $\Gamma = 1$. The interface is represented by moving Lagrangian marker particles with a parameter representation $(r(s), z(s))$ where s is the arc length starting from the apex of the drop. The VOF function ϕ, the volume fraction of the drop phase occupied in a cell presented in Fig. 3-5, is calculated based on the initial drop shape on the fixed Eulerian grid. Then the time-splitting method in Eqs. 3.6 to 3.8 is applied to solve the single-fluid VOF formulation (Eqs. 3.4 and 3.5) for the velocity and pressure fields on the fixed grid. The velocities of the marker particles on the moving grid

at the interface are determined by employing a bilinear interpolation presented in Eq. 3.19 based on the velocity fields obtained on the fixed grid. The marker particles are advected as material particles based on the kinematic condition in Eq. 3.16 to determine the new interface location using an explicit Euler scheme. As the interface is continuously expanding, marker particles are added at each time step to maintain the same level of discretization. Once the updated drop shape is obtained, a new ϕ field is calculated for next time step. For the surfactant cases, the surfactant concentration at the interface and interfacial tension are updated using Eqs. 2.23 and 2.26. The surfactant mass balance Eq. 2.26 is discretized using a finite difference formulation into the form of Eq. 3.28 and solved for the surfactant concentration at the interface. For the cases with shear-thinning drop fluid, the viscosities are updated via the Carreau model for the drop phase in Eq. 2.34. This algorithm is repeated until the neck radius that forms beneath the primary drop is smaller than 0.01. The mesh sizes of the fixed Eulerian grid and the moving Lagrangian grid and the time step are chosen to ensure convergence of drop shape, velocity and pressure fields for a chosen set of non-dimensional parameters. A mesh size of at least 0.025 and a time step of at least 10^{-4} is used.

4.4 Literature Review

Drop formation in co-flowing fluid streams has been studied experimentally [22, 30, 55, 65, 82, 88, 129, 131, 132, 147, 149], as well as numerically using boundary integral methods [147], finite element methods [120], volume-of-fluid and front-tracking methods [62, 64, 149], and FLUENT [63, 134]. Two modes of drop formation have been observed experimentally in co-flowing systems, namely, dripping and jetting [22, 30, 55, 65, 82, 131, 132, 149], and have been simulated numerically [62, 63, 64].

In the dripping mode, drops breakup close to the capillary tube while in the jetting mode, drop detachment takes place at the end of long threads. A third mode of break-up was numerically predicted by Suryo and Basaran [120] in the Stokes flow limit where the drop fluid took on a conical shape and a thin fluid jet emanated from the conical tip shedding drops. They referred to this mode of breakup as tip-streaming. Recently, Marin et al. [82] have observed the tip-streaming in their experiments. Prediction of drop size at the breakup and the breakup pattern is critical in a variety of applications mentioned in Chapter 1. The drop size and breakup pattern depend on flow rates, fluid viscosities, and interfacial tension which is captured by the Bond number and the capillary number which give the relative significance of viscous forces and gravitational forces as compared to interfacial forces respectively.

Most of studies above investigated the effect of the flow rates of the outer and inner fluids on the drop size [30, 62, 63, 64, 88, 120, 147, 149], the drop breakup time [30], and the dripping-jetting transition [30, 62, 63, 64, 132, 149]. Smaller primary drop (detaching drop) and longer detachment length are seen with co-flowing flows even in the absence of a confining wall [30, 88, 147]. As the flow rate of the outer fluid increases compared to the inner fluid flow rate, the viscous shear stress on the inner drop fluid increases. This reduces the primary drop size and the time required for the drop to break up [30, 63, 64, 120, 147, 149]. Oguz and Prosperetti [88] used a boundary integral method to study the dynamics of bubble growth and detachment from a submerged needle. They assumed the flow was inviscid and irrotational, and there was no confining wall around. In the last part of their study, they introduced an outer fluid flowing parallel to the needle and showed that bubble formation in a co-flowing outer liquid with a considerably smaller bubble size and less breakup time than in a quiescent liquid. Motivated by Oguz and Prosperetti's work,

Zhang and Stone [147] also applied the boundary integral method to study a drop dripping from the tip of a vertical circular capillary tube into an outer co-flowing immiscible fluid still in the absence of a confining wall but extended to viscous flows in the creeping flow limit (low Reynolds number). They studied the impact of the outer viscous flow on the drop size and showed that the volume of the primary drop reduced as the velocity of the outer fluid increased due to the higher drag force. Later, Zhang [149] conducted both experimental and numerical work to study the formation of a viscous liquid drop growing upwards at the tip of a vertical circular inner tube into an ambient viscous fluid in another cylindrical tube. Zhang developed a numerical model to predict the evolution of the drop shape and its breakup using the volume-of-fluid/continuum-surface-force (VOF/CSF) method. Two coaxially aligned cylindrical tubes were set up in the simulations. The Navier-Stokes equations were fully solved by applying a finite difference formulation on a fixed Eulerian grid. In order to verify the numerical results, Zhang also designed experiments to observe the dynamics of drop formation of a liquid-liquid system of 2-ethyl-1-hexanol (2EH) drops breaking into distilled water and compared the experimental measurements with the numerical results. Zhang's numerical work accounted for the effects of inertia, capillary, viscous, and gravitational forces as well as the confining wall effect on the drop formation and satellite drop generation in a quiescent or flowing ambient fluid. It showed that the introduction of an external flow led to a decrease in the drop size but an increase in the limiting length of drop (the length of the drop from its apex to the tube exit at breakup) at a low Reynolds number in the presence of confining wall [149]. Cramer et al. [30] systematically conducted experiments to study the dynamics of drops expanding at a capillary tip and dripping into a co-flowing ambient fluid. A cylindrical capillary was placed inside a much larger outer rectangular channel, so the wall effect of outer channel can be neglected. The outer fluid was sunflower

oil, and the inner fluid was κ-Carrageenan solution which was a shear-thinning fluid. They assumed the shear-thinning behavior had no impact on the drop formation. A discontinuity in drop size was found when increasing the velocity of the outer flow showing two distinct modes: dripping and jetting. Then they only focused on dripping, and showed the effects of the flow rates of the continuous and the disperse phases, drop viscosity, and interfacial tension on drop formation and satellite drop generation. As the velocity of the continuous phase increased, the primary drop size and the drop formation time both decreased, but the satellite drop size increased. As the velocity of the dispersed phase increased, the drop size slightly increased but the drop formation time slightly decreased. More numerical work on the drop formation in co-flowing fluids has been done since then. Suryo and Basaran [120] used the Galerkin/finite element method to numerically demonstrate the dynamics of drop formation downwards into a co-flowing ambient fluid under creeping flow condition. Two coaxially aligned cylindrical tubes were set up in the simulations with the radius ratio of outer to inner tubes of 2. They focused on the effect of the flow rate ratio of outer fluid to inner fluid (Q_2/Q_1) on the drop formation when viscosity ratio was set to 1 and capillary number was fixed at 0.01. They identified three flow regimes, namely, slug flow, dripping, and tip streaming while increasing Q_2/Q_1. The slug flow occurred when Q_2/Q_1 was small where the primary drop in this region was elongated axially and tended to occupy the entire cross section of the outer tube, so its aspect ratio L_p/D_p (defined as the ratio of its axial length to its maximum diameter) $\gg 1$. As Q_2/Q_1 increased, the dynamics showed a transition to dripping regime, where the aspect ratio was close to 1. As Q_2/Q_1 increased, the importance of viscous drag force by the outer fluid to the surface tension increased, resulting in the increasing limiting length L_d (measured from the tube exit to the drop tip at breakup) while the primary drop volume V_p decreased. As Q_2/Q_1 further increased, the viscous stress became so

large that tip streaming occurred. Hua et al. [64] numerically studied drop formation in co-flowing immiscible liquids in a microchannel with negligible gravitational effects using front tracking/finite volume method. Two coaxially aligned cylindrical tubes with the radius ratio of outer to inner tubes of 3 were set up in the simulations. They investigated the effects of the outer continuous phase flow speed, viscosity, and the interfacial tension on the droplet size with Re_1 defined as $\rho_1 u_1 R_1 / \mu_1$ and ρ_2/ρ_1 fixed to 0.1 and 0.8, respectively. For the parameters they studied, they observed the drop size decreased with the increase of the continuous phase flow rate and viscosity, and with the decrease of the interfacial tension. For the effect of the flow rate of the continuous liquid phase, they observed the sharp transition of dripping to jetting with a sudden drop of the drop size, and drew two main correlations of the drop size with the continuous phase flow parameters for dripping and jetting from a scaling analysis. Their results indicated that drop formation in a co-flowing system depended on the balance between the viscous shear force from the outer fluid and interfacial tension on the droplet. Hong and Wang [63] numerically studied the flow rate effect on drop formation in a co-flowing microfluidic device by FLUENT simulation software. They set up two coaxially aligned cylindrical tubes with the radius ratio of outer to inner tubes of 2 in the simulations, and assumed the inertia and gravitation effects could be neglected. For the flow rate ratio of outer to inner fluids (Q_2/Q_1) smaller than 10, drop size seemed approximately independent of the flow rate ratio and drop size decreased almost linearly with the increase of capillary number of the outer fluid ($Ca_2 = \mu_2 u_2/\sigma$). For the flow rate ratio larger than 10, four drop patterns were observed: laminar flow, polydisperse, and monodisperse with larger and smaller drops compared to the tip size. Four corresponding demarcated regions indicated that polydisperse pattern could be avoided by selecting $Ca_2 < 0.177$, and laminar flow pattern could be avoided by selecting $Ca_2 < 0.133$. Recently, Homma et al. [62]

employed a front-tracking/finite difference method to numerical simulate the jet and drop formation in co-flowing streams. Two coaxially aligned cylindrical tubes with the radius ratio of outer to inner tubes of 3 were set up in the simulations, and also the inertia and gravitational effects were neglected. For density ratio and viscosity ratio of outer to inner fluids set to 0.8 and 1.5, Reynolds and Weber numbers of inner fluid as 0.2 and 0.002, respectively, they showed drop diameter decreased as the velocity of ambient fluid increased. A jump in drop diameter was observed indicating a dripping to jetting transition. This result was consistent with the numerical results of Hua et al. [64].

Several studies have investigated the influence of fluid viscosities and interfacial tension captured by the Bond number and the capillary number on the drop formation process in a quiescent or a co-flowing outer fluid. Even without the outer co-flowing fluid, the viscosity of the drop phase plays a very important role in stabilizing an expanding drop by damping interfacial oscillations resulting in increasing length of the liquid thread with increased drop viscosity, but has no obvious effect on the size of the primary drop [147, 149, 150]. Zhang and Basaran [150] conducted a comprehensive experimental study on the dynamics of a viscous drop dripping into ambient quiescent air. The effects of the thickness of the tube wall, the flow rate of the drop phase, and the physical properties of the drop phase on the primary drop volume and limiting length and the creation of the satellite drops were investigated in detail. Water and glycerol solutions were selected for different viscosities of the drop phase. It was found that larger variations in viscosity could result in significant differences in evolution of the drop shapes. The capillary number describes the relative importance of viscous forces to interfacial forces. Larger capillary number indicating larger drop viscosity and lower interfacial tension gave rise to longer liquid thread at breakup [150]. Most of their work focused on the study of dynamics of drops dripping into a quiescent

ambient fluid at low Reynolds number in the absence of a confining wall. They investigated the effects of the viscosity ratio of inner to outer fluids, the Bond number and the capillary number on the volume of the primary drop and the fluid column length at breakup by changing one dimensionless number while keeping the other two dimensionless parameters. It was shown that the viscosity ratio had a much larger impact on liquid thread length than on the drop size. Drops with larger viscosity ratio showed longer liquid thread lengths at breakup. As the Bond number increased, the volume of the primary drop reduced and the remaining liquid thread changed from convex to narrow tapered due to the increasing pulling force by gravitation relative to interfacial tension. With the increasing capillary number, drops took longer time to break up with a larger volume of primary drop and longer liquid thread length. Similarly, Zhang's numerical work [149] which applied VOF-CSF method mentioned in the last paragraph also concentrated on the drop formation upwards into another quiescent immiscible fluid filled in the outer tube. Zhang investigated the interplay between the effect of inertial, capillary, viscous, and gravitational forces and confining wall effect in the absence of outer flow. The length of the thread and the primary drop size decreased with decreased Reynolds number and capillary number, and with increased Bond number in a quiescent ambient fluid. The drop size showed a slight increase and then decreased when increasing the viscosity ratio of inner to outer fluids. The confinement effect of outer tube wall on drop formation in the absence of outer flow resulted in larger detaching drop volumes and shorter thread length [149]. In the presence of co-flowing fluid, drop fluid resisted the squeezing and shearing of the outer fluid resulting in larger drops with longer remnant drop lengths as the viscosity of the drop phase increased [30, 64]. The experimental work done by Cramer et al. [30] also confirmed that the drop viscosity had no obvious impact on the drop size, but did affect the length of liquid thread for co-flowing fluid systems. Higher

61

viscosity of the disperse phase gave a longer thread between the capillary tip and the drop because the viscous pressure in the thread opposed to the capillary pressure. The extended thread enhanced the satellite drop generation. The interfacial tension also played an important role. Smaller drops were generated for the system having lower interfacial tension. In the numerical work done by Hua et al. [64], they also observed that the drop size decreased with increasing viscosity of continuous phase and decreasing interfacial tension.

Surfactants are present or added intentionally to a variety of applications involving emulsions and drop formation to facilitate breakup, influence the sizes of detached and satellite drops, and prevent their coalescence after formation. Soluble surfactants are transported to the interface by bulk diffusion and interface adsorption/desorption and distribute along the interface by interfacial convection and diffusion. At equilibrium in the absence of flow, surfactant molecules adsorb on the fluid interface establishing an equilibrium surfactant concentration resulting in an equilibrium interfacial tension that is lower than the clean interfacial tension. Non-uniform surfactant distributions result in the presence of imposed flow when surfactant mass transfer from the interface is slow compared to the interfacial convective flux. Local variation of interfacial tension along the interface alters the normal and tangential stress balances at the interface. Marangoni stresses due to the non-uniform surfactant distributions result in a flow that opposes the flow driving the local variation in interfacial concentration.

Both experimental [150] and numerical [66, 67, 140] work has been done to study the drop formation in a quiescent ambient fluid in the presence of surfactants. Zhang and Basaran [150] conducted experiments on the dynamics of a viscous drop dripping into ambient quiescent air in the presence of surfactants. To investigate the surfactant effects on the drop formation dynamics, they used a water-soluble surfactant Triton X-100 while keeping drop viscosity and density unchanged. The surface

tension that affected the drop formation became dynamic and locally related to accumulation and distribution of surfactants on an expanding and stretching surface. Marangoni stresses generated by the surface tension gradients could alter the drop deformation and breakup. With slow expansion of the drop surface at low flow rates of the drop phase, the surfactants had enough time to transport to the surface and lower the surface tension until equilibrium, so the primary drop volume and the limiting length decreased as surfactant concentration increased. With fast expansion of the surface at high flow rates, the surfactants were highly diluted so the reduction of the primary drop volume and the limiting length became much less with the same increase of surfactant concentration. The volume of the satellite drops generated by the breakup of the liquid thread increased with increasing surfactant concentration because the presence of surfactants stabilized the thread and increased the volume of the liquid thread. In the presence of surfactants, the drop necking process can be very complex [66, 67, 140]. Jin et al. [66] numerically studied the effects of adsorption-desorption controlled soluble surfactants on a buoyant viscous drop injected into a quiescent viscous ambient fluid through an orifice by a front-tracking scheme. The incompressible Navier-Stokes equations for both inner and outer fluids were fully solved using the continuum surface force (CSF) method. They used finite-difference method to discretize the computational domain into a fixed, uniform staggered grid. They studied the effects of the equilibrium surface coverage $(0 < x < 0.9)$ and adsorption-desorption kinetics reflected by the Biot number $(0 < Bi < 10)$ on necking dynamics. Surfactants accumulated just above the neck where the interface contraction was the fastest. For low surface coverage $(x < 0.3)$, a weak Marangoni flow was generated, and the primary neck was still the detachment point. As x increased $(0.3 < x < 0.5)$, the primary neck first formed but slowed down by an increasing Marangoni flow, and the secondary neck formed later at a faster rate, thus a symmetric neck shape was

achieved. As they further increased x to 0.6, the thinning rate of the secondary neck became dominant since the primary neck was suppressed by the accumulation of surfactants above the neck. An inverted neck shape was formed and the drop detached at the secondary neck. Finally when they increased x to a sufficiently high value of 0.9, a strong Marangoni flow inhibited the necking and the drop failed to neck. They also investigated the importance of Bi on necking dynamics at a high surface coverage of $x = 0.9$. If the sorption kinetics were very slow ($Bi = 0$), the surfactants were highly diluted as the drop expanded, and the drop broke at the primary neck. As Bi increased, the sorption kinetics became faster and more surfactants accumulated onto the expanding interface, the neck shapes changed from breaking at the primary neck ($Bi = 10^{-4}$), to approximately symmetric necks ($Bi = 10^{-3}$), and to inverted necks ($0.01 < Bi \leq 0.05$) until the necks failed to thin ($0.1 < Bi \leq 0.2$). As Bi further increased, the sorption kinetics were faster than the dilatation rate, thus the necks experienced the inverted shape, the symmetric shape, and then the thinning of the primary neck again. Later, Jin and Stebe [67] presented a numerical study of the effects of diffusion controlled soluble surfactants (where diffusion became the limiting step instead of adsorption-desorption) on a buoyant viscous drop injected into a quiescent viscous ambient fluid through an orifice. They studied the necking dynamics and drop formation for equilibrium surface coverage ranging from 0.5 to 0.95 ($0.5 < x < 0.95$) as a function of Ψ, the ratio of surfactant diffusion rate between the interface and the bulk to the surface contraction/convection rate. The drop evolved starting from a planar interface, followed by expansion and the neck formation. The surfactant interfacial concentration became above its equilibrium value when the interface contracted fast above the neck. Then the surfactant started to desorb into the region near the interface having few surfactants. The rapid diffusion fluxes from the neck to the bulk thus created, removed the surfactant effectively from the neck

region and avoided the strongly non-equilibrium effects (local strong reduction in the surface tension). Thus, even up to high surface coverages of $x = 0.9$, neck dynamics were still altered weakly. Only for very high surface coverages close to the maximum packing ($x = 0.92$) and for slow diffusion fluxes, strong non-equilibrium effects could develop to alter the neck dynamics and even lead to the failure of the necking. Various neck shapes and regimes where drops failed to detach were observed while tuning the ratio of surfactant diffusion rate (between the interface and the bulk) to the rate of interface contraction. Xu et al. [140] raised a question if surfactant could be present at pinch-off of a liquid filament, and analyzed the dynamics of a filament loaded with a monolayer of insoluble surfactant in a quiescent ambient gas using theory and simulation by finite element method. The amount of surfactant remaining at the location where a filament broke up related to the Peclet number, the ratio of convection to diffusion between the interface and the bulk, since the Peclet number was proportional to the filament radius. Thus, it was customary to think that almost no surfactant would be present when a macroscale filament broke. In their work, Xu et al. showed that the surfactant concentration at breakup is not zero but uniform on the filament when the Peclet number is very small or the diffusion rate is much faster then the convection rate.

Limited work has been conducted to study the surfactant effect on drop formation in a co-flowing system [129, 132]. Utada et al. [132] experimentally investigated the dripping-to-jetting transitions in co-flowing liquid streams. Coaxially aligned capillary tubes were used: an inner cylindrical tube with a tapered tip and an outer square tube (a second cylindrical tube was placed inside the square tube and surrounded the inner tip when high velocity was needed). The inertial, gravitational and outer tube wall effects could be neglected. They observed two classes of dripping-to-jetting transitions indicating two different mechanisms controlling drop size. The first tran-

sition to thinning (or narrowing) jetting was driven by the flow rate of the outer fluid. The viscous shear stresses on the drop was balanced by surface tension where the jets became thinner. The capillary number of the outer fluid Ca_{out}, dictated this balance. The second transition to widening jetting was driven by the flow rate of the inner fluid. The inertial forces of inner fluid were balanced by the surface tension where the jets became wider. The Weber number of the inner fluid, We_{in}, dictated this balance. Thus, the dripping-to-jetting transition could be characterized in a state diagram as a function of Ca_{out} and We_{in}. They added surfactant sodium dodecyl sulfate (SDS) to the continuous phase to lower the surface tension, but did not look at the surfactant effects on drop breakup dynamics in detail. Umbanhowar et al. [129] developed an experimental technique to produce highly monodisperse emulsions via drop formation at the end of a tapered capillary tube in a co-flowing stream. They focused on dripping with negligible inertial and gravitational effects. The viscous drag was balanced by surface tension, so drops would detach when the drag exceeded the surface tension. They added surfactant sodium dodecyl sulfate (SDS) to the continuous phase to lower the surface tension to prevent droplet coalescence and form stable emulsions. For the parameters they studied, they showed the drop diameter was a decreasing function of the outer flow velocity in the presence of SDS. Control of the velocity of outer flow allowed precise selection of drop size. They were only interested in how the surfactants stabilized the emulsion, but did not further their research about how surfactants affected drop breakup dynamics.

In recent years several studies have been conducted to determine the effect of non-Newtonian rheology on the drop formation process by adding polymers into solutions. Polymeric solutions can exhibit various non-Newtonian behavior such as shear-thinning, flow history dependence as well as elastic stresses [13]. Most of the previous studies with non-Newtonian fluids deal with drop formation in a quiescent

66

ambient fluid [27, 38, 39, 115, 143], and more recently have been extended to the co-flowing system [61]. The presence of polymers in Newtonian solvents can exhibit viscoelastic property. Even adding a small amounts of polymers can have a significant impact on the behavior of two-phase systems especially in extension-dominated flows shown in some recent experimental work [27, 115]. Shore and Harrison [115] used a high-speed camera to observe the formation of low viscosity elastic drops from a nozzle into quiescent air to study the effect of elasticity on the on-demand drop formation process. They observed that the drop fluids containing polymers (PEO) had a longer thread, a longer time to separation, and a lower velocity but suppressed satellite drops (with sufficient polymers) compared to the Newtonian drop fluids with similar shear viscosity. Clasen et al [27] experimentally studied the breakup of capillary jets of dilute polymer solutions into quiescent air and the dripping to jetting transition. They found that the interplay of gravity, inertial forces, and surface tension mainly determined the dynamics of the terminal drop growth and trajectory, while the thinning process of viscoelastic ligaments controlled drop breakup by a constant axial force driven by surface tension and resisted by the viscoelasticity of polymer molecules.

Stiffer polymer molecules (ideally like rods) in solution have diminishing memory effects [42] like a simple case of 'generalized Newtonian liquid' described by the Carreau model in Eq. 2.33. If $n < 1$, the liquid behaves shear-thinning such as the Xanthan gum solution. Since the viscosity decreases as pinching progresses, the breakup of the shear-thinning liquid is expected to speed up. Davidson and Cooper-White conducted numerical studies to predict the dynamics of shear-thinning drops dripping into a quiescent air from a circular orifice using a VOF method [38, 39]. The shear-thinning drop fluid was described by the Carreau model. They validated their numerical method by comparing their results of the breakup of a Newtonian

drop (milli-Q water at $21°C$) between experiments and numerical calculations. For the parameters they studied, they showed a more rapid breakup and less secondary drops and the drop limiting length was reduced with increasing shear-thinning. The shear-thinning effect on the reduction of drop length was shown more obvious with a high drop viscosity than a low drop viscosity. Yildirim and Basaran [143] computationally studied the dynamics of non-Newtonian drops dripping into quiescent air. They employed the Carreau-type models which accounted for both shear-thinning and shear-thickening for the drop fluids and solved the slender-jet equations using Galerkin/finite element method. They suggested that the shear-thickening effect built in the model could mimic the behavior expected in viscoelastic fluids in an extensional flow though the viscoelastic effects were not account for in the model. Their results indicated that the effect of shear-thickening contributed to the observed bead-on-string patterns along the threads close to breakup which were typically attributed to viscoelastic effects, while the effect of shear-thinning contributed to reduced thread length.

Homma et al. [61] numerically studied the breakup of a laminar jet into drops in a co-flowing shear-thinning liquid-liquid system using a front-tracking/finite difference method. They used the Carreau-Yasuda model [59, 142] to describe the shear-thinning viscosities. This model just replaced both 2 in the indices in Eq. 2.33 by a general parameter x which was usually 2 but sometimes was adjusted to fit specific experimental data [52]. They validated their method by computing a steady flow in a circular tube for a single-phase shear-thinning fluid with same parameters and compared the numerical results with experimental data [52]. They set the velocities of inner and outer fluids to be the same for the co-flowing condition. Their results showed that the breakup length of the jet became larger when shear-thinning occurred inside the jet, while the jet became shorter when shear-thinning occurred in

the continuous phase.

The only study of the drop formation process in a non-Newtonian two-phase system in the presence of surfactants was the numerical study conducted by Xue et al. [141]. They used a finite element method on the capillary breakup of shear-thinning liquid jets with soluble surfactants. They applied the Carreau model to simulate the shear-thinning drop liquid which was surrounded by an inert gas, and a nonlinear equation of state to describe the surfactants. Their results indicated that a strong synergistic interaction between shear-thinning rheology and surfactant parameters played a critical role in the formation of satellite drops. They showed a satellite drop could be present during breakup when the drop was shear-thinning and coated with insoluble surfactant for a set of Carreau parameters $\beta = 0.002$ and $\alpha = 10$ whereas no satellite drop formed when either only the drop was shear-thinning or only insoluble surfactant was present.

4.5   Results and Discussion

In this section, the numerical results for the surfactant-free and surfactant-laden Newtonian [33, 34] as well as the shear-thinning fluids are presented. In all the simulations, the needle geometry is set to $L_n/R_1 = 2$ and $W_n/R_1 = 0.1$. Studies were conducted for varying needle lengths to establish that for $L_n/R_1 \geq 2$ the drop evolution was independent of the needle length. First, a typical surfactant-free case of drop formation in co-flowing Newtonian fluids is presented in Fig. 4-2. The stages of drop formation in a surfactant-free system for $R_2/R_1 = 3$, $\chi = \lambda = 0.1$, $Re = 10$, $Ca = 0.1$, $Bo = 1$ and $Q_2/Q_1 = 10$ are shown in Fig. 4-2(a). The normal and tangential velocities along the drop for the drop shape close to breakup is shown in Fig. 4-2(b). The drop starts with an initially hemispherical shape and then distends

due to gravity and outer fluid flow and eventually necks and breaks. The detaching drop is defined as the primary drop and the cone (or thread) behind the breakup point is defined as the remnant drop. As the drop enters a necking regime, two neck regions appear as shown in the expanded view in Fig. 4-2(a). The neck closest to the detaching drop is designated as the primary neck which thins the fastest and is typically the point of detachment in experiments. The normal and tangential interfacial velocities are also highest in the vicinity of the primary neck region as seen in Fig. 4-2(b). The secondary neck appears as an inflection above the remnant drop. The effect of dimensionless parameters on the drop formation process is quantified by comparing the time for breakup, t_b, and the volume of the primary drop at breakup, V_p. Results are also presented in terms of the length of the remnant drop at breakup, L_r, and the limiting length, L_d, which is defined as the length of the drop from its apex to the tube exit at the time of breakup [120] as show in the schematic in Fig. 4-3.

4.5.1 Validation of Numerical Method

In order to validate the numerical method, the numerical results from this study are compared with the experimental results of Zhang [149]. In Zhang's experiments, 2-ethyl-1-hexanol (2EH) drops were formed at the tip of a capillary tube submerged in a container of distilled water. Wall effects were neglected as the container was large compared to the capillary tube radius. The viscosity and density of the drop phase and the bulk phase were 8.9 cP and 0.83 g/cm^3 and 1 cP and 1.0 g/cm^3, respectively with an interfacial tension of 13.2 $dynes/cm$. Since Zhang reported dimensional time and it was not clear what the initial interface shape was, the following procedure is used to compare the numerical results to their experimental shapes. The experimental time before breakup is defined as $\tau = (t^* - t_b^*)$ where t^* and $t_b^* = 1.2712s$ are the dimensional time and breakup time reported by Zhang [149]. The experimental

70
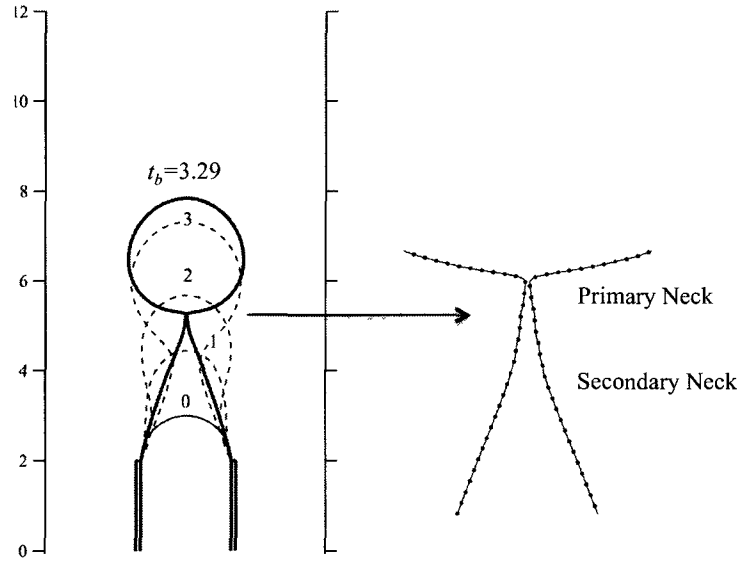
(a)
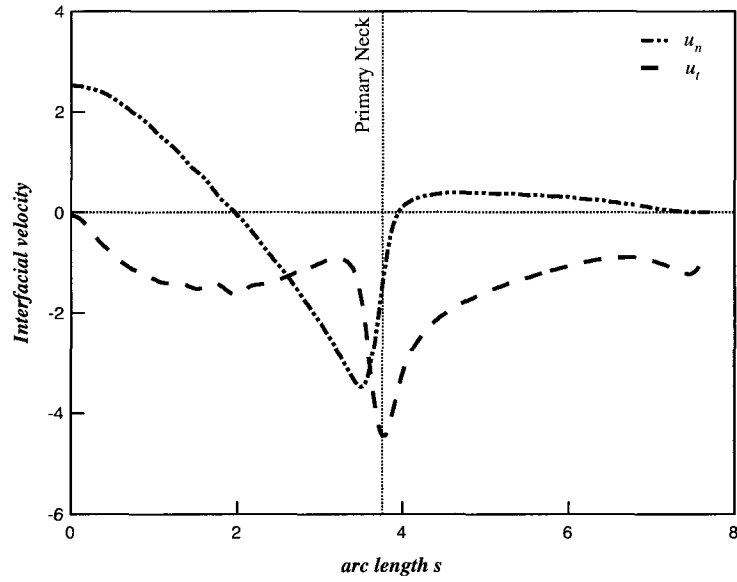
(b)

Figure 4-2: (a) Drop formation dynamics for a surfactant-free system with an expanded view of the primary and secondary necks and (b) interface velocity as a function of arc length at $t = 3$ for $R_2/R_1 = 3$, $\chi = \lambda = 0.1$, $Re = 10$, $Ca = 0.1$, $Bo = 1$, and $Q_2/Q_1 = 5$. Shapes at every dimensionless time of 1 along with the final shape are shown.

71
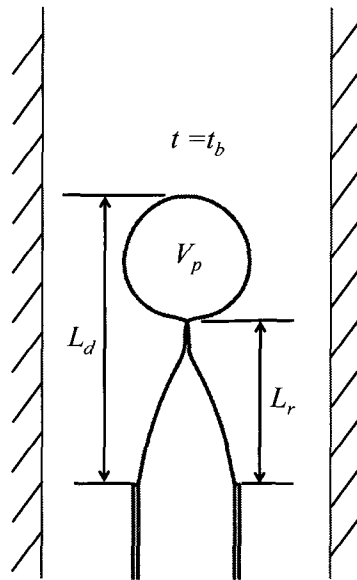
Figure 4-3: The schematic of characteristic parameters for the description of the drop shapes at breakup time, t_b.

$\tau = -0.672$ s $\tau = -0.362$ s $\tau = -0.062$ s $\tau = -0.022$ s $\tau = -0.002$ s $\tau = 0$ s
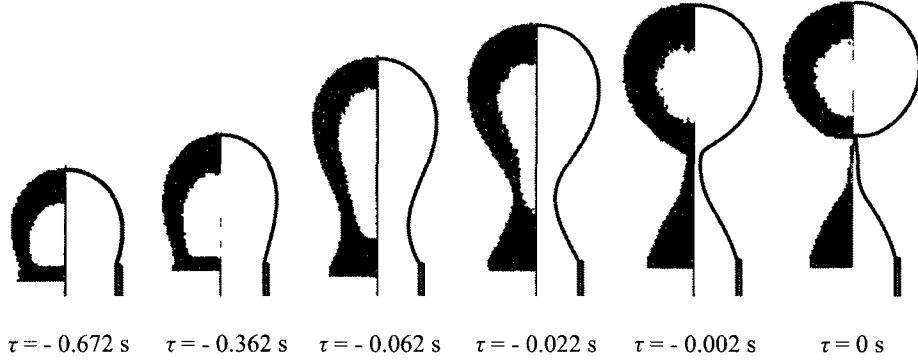
Figure 4-4: The comparison of drop evolution observed in Zhang's [149] experimental work (left half) and predicted in our numerical simulation (right half).

shapes observed by Zhang at different times between $\tau = -0.672s$ and $\tau = 0s$ are shown on the left half of the comparisons in Fig. 4-4. Based on Zhang's experimental data, the non-dimensional parameters for the numerical simulations are chosen as $\chi = 0.832$, $\lambda = 8.9$, $Re = 16.53$, $Ca = 7.85 \times 10^{-4}$, and $Bo = 0.317$. Since there is no outer flow, Q_2/Q_1 is set to 0 in the simulations. R_2/R_1 is set to 6 to eliminate the effect of confining wall and the needle dimensions as $W_n/R_1 = 0.1$ and $L_n/R_1 = 2$. Numerical simulations are conducted using the set parameters till the drop breaks up at $t_b = 5.62$. Then the numerical drop shapes are determined corresponding to the dimensional times τ shown in Fig. 4-4 by defining $\tau = (t - t_b) \times t_c$ where $t_c = R_1^*/U_1^* = 0.154s$ is the characteristic time scale based on Zhang's experimental data. The numerical drop shapes obtained by this procedure are shown on the right half of Fig. 4-4. As is seen in Fig. 4-4, the numerical simulations agree well with the experimental results of Zhang [149] for drop formation in a quiescent fluid in the absence of wall effects.

73

4.5.2   Surfactant-free Results for Newtonian Fluids

In this section, the results for drop formation in co-flowing Newtonian fluids are presented. The effects of the confining wall of outer tube, the flow rate ratio Q_2/Q_1, the viscosity ratio λ, the Bond number Bo, and the capillary number Ca on the drop formation process are discussed. For these simulations, the density ratio is set to $\chi = 0.1$ and the Reynolds number is set to $Re = 10$. Even in the absence of an outer flow, the presence of a solid wall near the evolving drop affects the drop breakup dynamics. Fig. 4-5(a) shows the effect of changing the diameter of the outer wall on the stages of drop evolution for $\chi = \lambda = 0.1$, $Re = 10$, $Ca = 0.1$, $Bo = 1$, and $Q_2/Q_1 = 0$. As the diameter of outer tube (or R_2/R_1) is reduced, the additional wall shear results in more prolate shapes for the evolving drop which take longer to break, and the primary drop volume increases consistent with the numerical simulations by Zhang [149]. In the absence of the outer flow, the remnant drop appears to be unaffected by the presence of the wall. When the outer co-flowing fluid with $Q_2/Q_1 = 5$ is applied, the confinement effect of outer wall enhances the impact of the outer flow on the drop formation process. With decreasing diameter of outer tube, increasing viscous shear stresses are applied on the inner fluid and make it break up sooner with smaller drop volumes as shown in Fig. 4-5(b).

To investigate the effect of the outer co-flowing flow on the drop formation process, the flow rate ratio Q_2/Q_1 is changed from 0 to 20 for $R_2/R_1 = 3$, $\chi = \lambda = 0.1$, $Re = 10$, $Ca = 0.1$, and $Bo = 1$. The effect of increasing the outer fluid flow on the primary drop volume at breakup and the time required for breakup are shown in Fig. 4-6(a). For $Q_2/Q_1 = 0, 5, 15$, and 20, the interface shape at breakup is also shown as insets in Fig. 4-6(a). As the flow rate of outer flow increases (i.e. Q_2/Q_1 increases), the outer fluid applies increasing viscous shear stress on the inner fluid and results
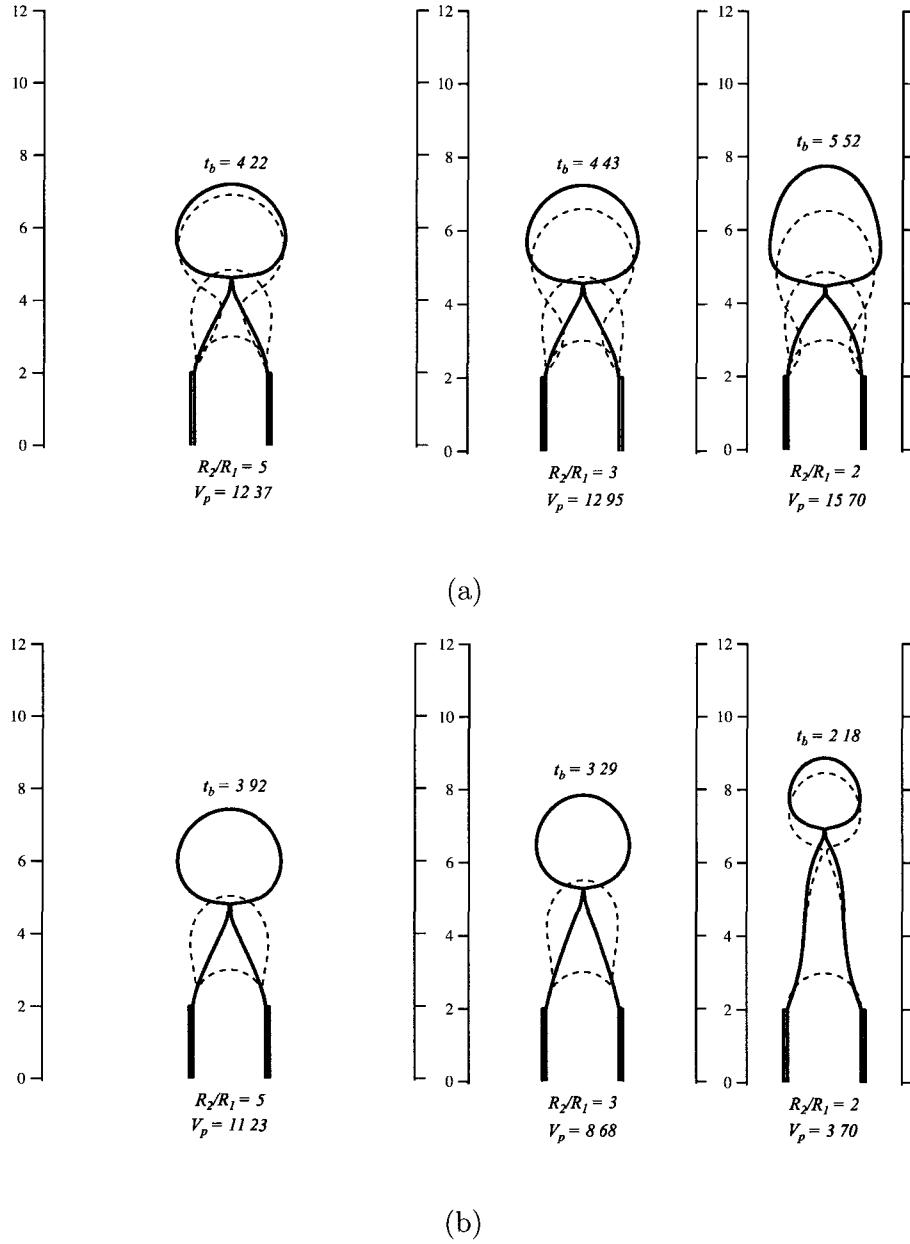
Figure 4-5: The effect of outer tube diameter on drop evolution dynamics in the surfactant-free system for $\chi = \lambda = 0.1$, $Re = 10$, $Ca = 0.1$, and $Bo = 1$ (a) without outer flow, $Q_2/Q_1 = 0$, and (b) with outer flow, $Q_2/Q_1 = 5$. Shapes at every dimensionless time of 2 along with the final shape are shown.

in more prolate drop shapes and longer remnant drop shapes underneath the neck region. As a result, the time for breakup reduces and the volume of the primary drop at breakup is smaller. This result is consistent with the existing experimental and numerical co-flowing studies in the absence of surfactants [30, 63, 120, 129, 147, 149]. For flow rate ratios above 17, the breakup time decreases but the primary drop volume remains almost unchanged. The limiting drop length and the length of the remnant drop first increases as developing a jetting thread and then decreases at the higher flow rate ratios due to the strong and fast squeezing of the outer flow. This is clearly seen in Fig. 4-6(b) where the limiting drop length, L_d and the length of the remnant drop, L_r are plotted as a function of the flow rate ratio.

The viscosity ratio λ gives the ratio of viscosities of the inner drop fluid to the outer bulk fluid. Numerical simulations were conducted for λ ranging from 0.03 to 1 for $R_2/R_1 = 3$, $\chi = 0.1$, $Re = 10$, $Ca = 0.1$, $Bo = 1$, and $Q_2/Q_1 = 5$. The breakup time and volume of the drop as a function of λ and the interface shape of drops at breakup for $\lambda = 0.03$, 0.1, 0.5, and 1 are presented in Fig. 4-7(a). The viscosity ratio plays an important role in the dynamic process of drop formation by resisting the shearing and squeezing of the outer fluid. As the viscosity of the drop phase increases (i.e. λ increases), the drop necking process slows down to cause the remnant drop to form long threads as seen in Fig. 4-7(b). The drop dynamics again shows a transition from dripping to jetting, and the drop becomes oblate before breaking up with larger volumes. These results are consistent with drop formation in a quiescent or co-flowing ambient viscous liquid [120, 149].

The Bond number, Bo, represents the importance of gravitational forces relative to capillary forces. The effect of Bo on the drop formation for $R_2/R_1 = 3$, $\chi = \lambda = 0.1$, $Re = 10$, $Ca = 0.1$, and $Q_2/Q_1 = 5$ is investigated. Larger Bo indicates larger gravitational forces compared to interfacial tension exerted on the drop to dislodge
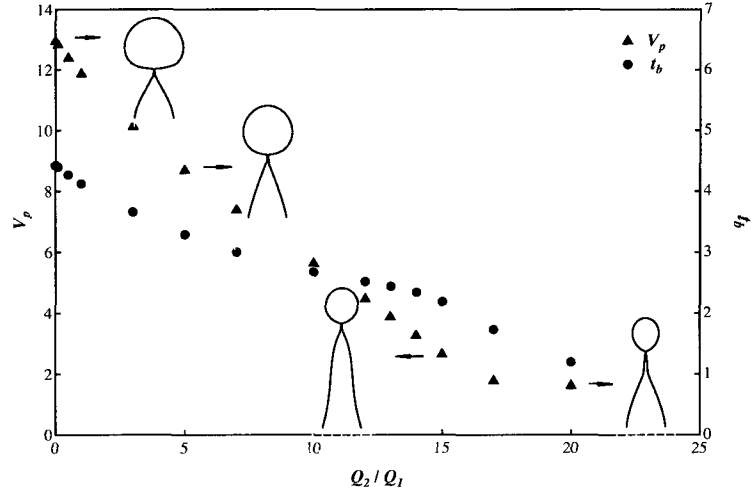
(a)
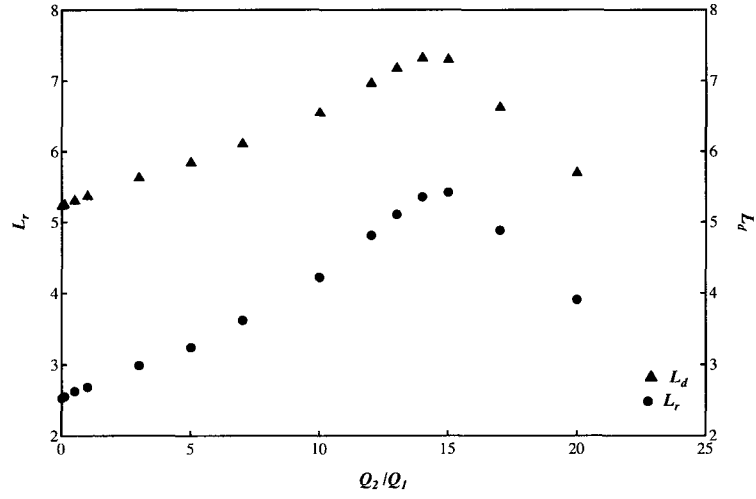
(b)

Figure 4-6: The effect of flow rate ratio on the (a) primary drop volume, breakup time, (b) remnant drop length, and limiting drop length at breakup for $R_2/R_1 = 3$, $\chi = \lambda = 0.1$, $Re = 10$, $Ca = 0.1$, and $Bo = 1$.

(a)

(b)

Figure 4-7: The effect of viscosity ratio on the (a) primary drop volume, breakup time, (b) remnant drop length, and limiting drop length at breakup for $R_2/R_1 = 3$, $\chi = 0.1$, $Re = 10$, $Ca = 0.1$, $Bo = 1$, and $Q_2/Q_1 = 5$.

the drop from the inner tube. Hence, drops breakup faster with smaller primary drop volumes and shorter and sharper remnant drop shapes. This is clearly seen in Fig. 4-8(a) where primary drop volume at breakup and breakup time are plotted as a function of Bo. Below a Bond number of 3, the primary drop volume at breakup, V_p and breakup time, t_b decline rapidly with increasing Bond number. However, for $Bo > 3$, V_p and t_b remain nearly unchanged for increasing Bond number values. The interface shapes at drop breakup for drops with $Bo = 0.05, 1, 2$, and 3 are shown as insets in Fig. 4-8(a). For small Bond numbers, the remnant drop has a more convex shape as more drop fluid is pumped into it while the drop takes longer to break. As Bo increases, the remnant drop becomes shorter but more tapered due to larger driving force to pull the drop liquid out of the tube and reduce the liquid volume remaining on the tube [147, 149]. The numerical simulations show that drops with a negative curvature in the rear are observed for $Bo \geq 3$. Such mushroom-shaped drops were also observed by Zhang [149] for $Bo \geq 10$ in the absence of outer co-flowing fluid. The length of the remnant drop and the limiting drop length are also plotted as a function of Bo in Fig. 4-8(b). As expected, both curves show that the remnant drop length and the limiting drop length reduces as Bo increases.

The effect of capillary number, Ca, on the drop breakup time, primary drop volume, remnant drop length, and limiting drop length at breakup are shown in Fig. 4-9 for $R_2/R_1 = 3$, $\chi = \lambda = 0.1$, $Re = 10$, $Bo = 1$, and $Q_2/Q_1 = 5$. Interface drop shapes at breakup for $Ca = 0.01, 0.1, 0.3$, and 0.5 are also shown in Fig. 4-9(a). As Ca increases, viscous forces become more dominant as compared to interfacial forces. As seen in Fig. 4-9 drop breakup slows down as Ca increases resulting in long remnant drop shapes. For larger Ca values, capillary forces are small enough to make more oblate detached drops with larger volumes. The dripping and jetting modes are clearly seen in Fig. 4-9(a). These results are consistent with the drop
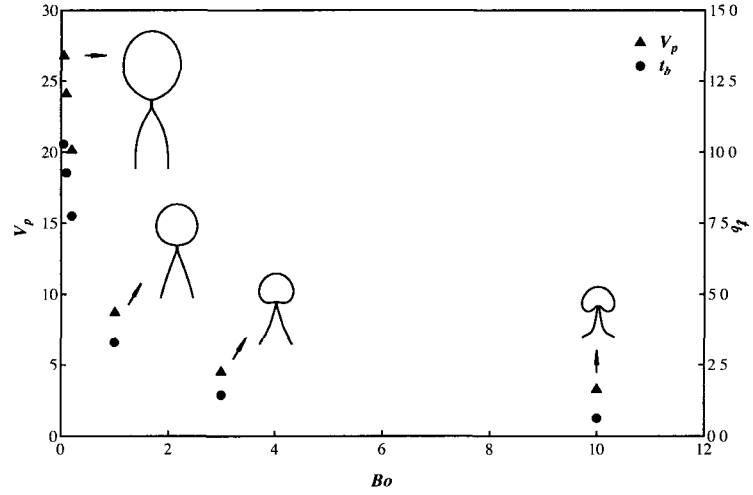
(a)
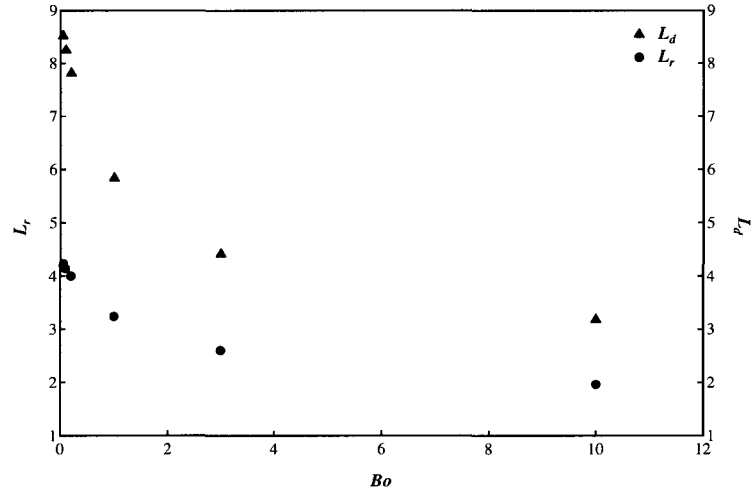
(b)

Figure 4-8: The effect of Bond number on the (a) primary drop volume, breakup time, (b) remnant drop length, and limiting drop length at breakup for $R_2/R_1 = 3$, $\chi = \lambda = 0.1$, $Re = 10$, $Ca = 0.1$, and $Q_2/Q_1 = 5$.

shapes observed for drop formation into a quiescent liquid [147, 149]. The remnant drop length and limiting drop length increase almost linearly with increasing Ca as seen in Fig. 4-9(b).

4.5.3   Surfactant Results for Newtonian Fluids

In this section, the effect of surfactants on the drop breakup and necking dynamics will be discussed. The density and viscosity ratios are set to $\chi = \lambda = 0.1$, the Reynolds number is set to $Re = 10$, the capillary number is set to $Ca = 0.1$, and the Bond number is set to $Bo = 1$ in all the simulations. The elasticity number is set to $E = 0.164$ as the typical value is much less than 1 and the interfacial Peclet number to $Pe_s = 10$ in the simulations in the presence of surfactants. The effects of surfactant mass transfer, the flow rate ratio, Q_2/Q_1, the proximity of confining walls, R_2/R_1, the equilibrium surfactant coverage, x, and the Biot number, Bi, on the drop breakup and necking dynamics are investigated.

Surfactant mass transfer plays an important role in the necking and breakup process [66]. When mass transport of surfactants to the interface is much faster than interfacial convection, the surfactant concentration at the interface remains almost at the equilibrium concentration and results in a uniform reduction in interfacial tension. This scenario is designated as 'uniform σ' for which $\sigma = 1$. For soluble surfactants in the adsorption-desorption limit, the rate of the surfactant mass transport to the interface is comparable to the interfacial convection rate and the adsorption/desorption rate of surfactants is much slower than the bulk diffusion rate. This scenario is designated as 'non-uniform σ' and a comparison of the drop evolution with the 'uniform σ' case is shown in Fig. 4-10. For this comparison, $\chi = \lambda = 0.1$, $Re = 10$, $Ca = 0.1$, $Bo = 1$, and $Q_2/Q_1 = 5$. For the 'non-uniform σ' case, $Pe_s = 10$, $x = 0.667$,
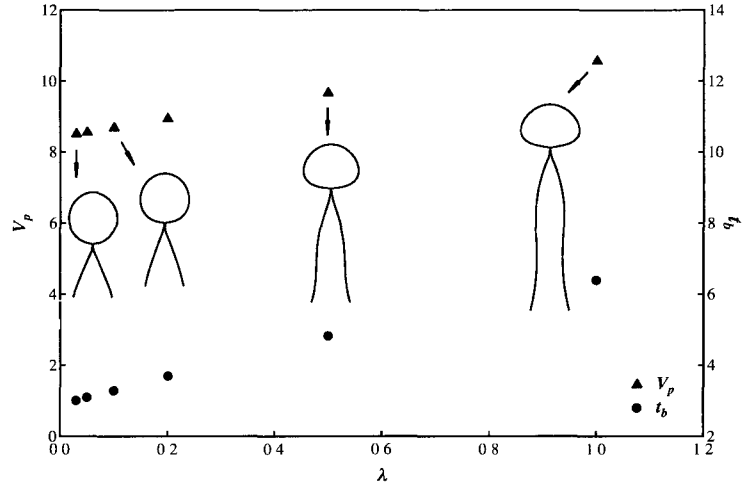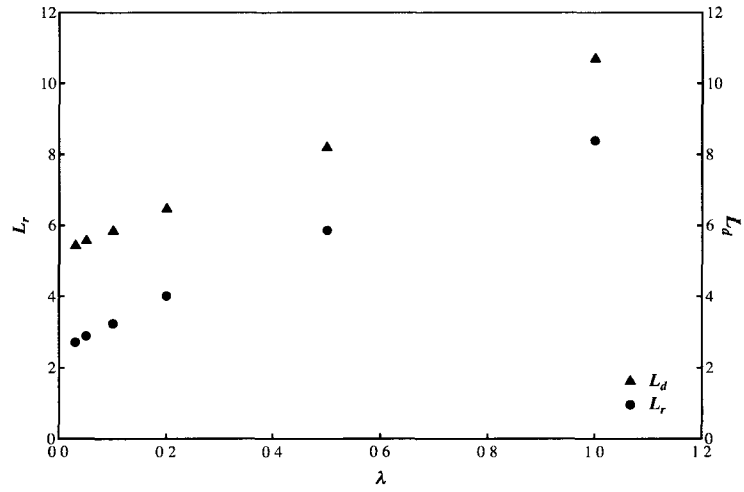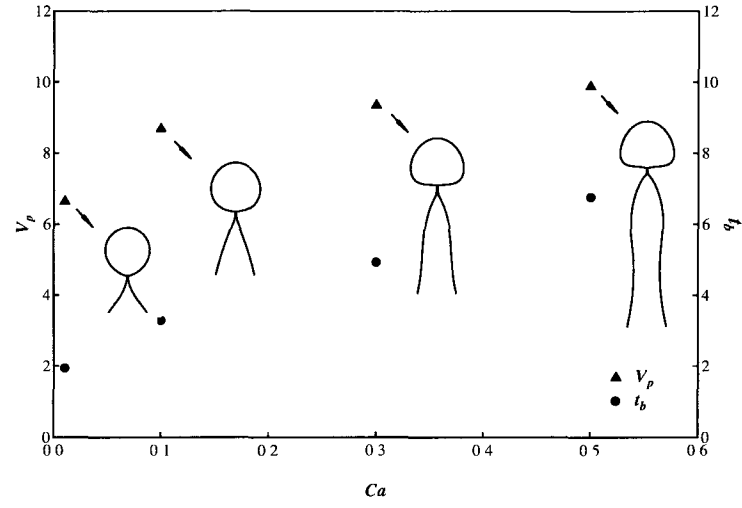
(a)
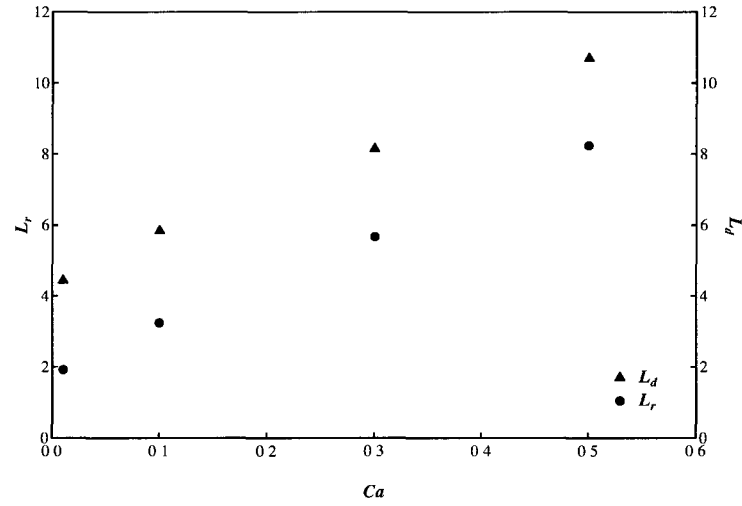
(b)

Figure 4-9: The effect of capillary number on the (a) primary drop volume, breakup time, (b) remnant drop length, and limiting drop length at breakup for $R_2/R_1 = 3$, $\chi = \lambda = 0.1$, $Re = 10$, $Bo = 1$, and $Q_2/Q_1 = 5$.

and $Bi = 0.1$. In both cases, the drop starts with an initially hemispherical shape and then distends due to the buoyancy force and the outer fluid flow. As the drop enters a necking regime, similar to the surfactant-free case, the primary neck and the secondary necks appear as shown in the expanded view in Fig. 4-10. The surface contraction is fastest in the vicinity of the neck as the normal velocity in this region is strongly negative and the tangential flow above the neck region is slower as is shown in Fig. 4-2(b) and by Jin et al. [66]. This causes the surfactants to accumulate just above the primary neck as shown in Fig. 4-11. For this case the maximum packing limit of surfactants is $\Gamma_\infty = 1/x = 1.5$. The surfactant concentration just above the primary neck approaches this limit from below. When surfactant concentration approaches the maximum packing limit, very small gradients in surfactant concentration result in large gradients in interfacial tension as seen in Fig. 4-11. As a result large Marangoni stresses are expected for perturbative gradients in surfactant concentrations [43].

The presence of surfactants just above the primary neck affects the rate of thinning of the primary neck [66, 67]. The primary neck radius versus time left to breakup is shown in Fig. 4-12 to compare the primary neck thinning process between the 'uniform σ' and the 'non-uniform σ' cases for the drop shape evolution shown in Fig. 4-10. The zoomed-in view close to breakup shown as an inset in Fig. 4-12 clearly indicates that with interfacial tension variation along the interface, the rate at which the primary neck forms slows down as the drop approaches breakup. The slowing down of the primary neck thinning rate has two consequences. First, it increases the time required for breakup of the primary drop in the presence of surfactants. Second, as the drop fluid is flowing at a constant flow rate, it increases the volume of the primary drop due to the increased time for breakup. It should be noted that in the above comparison both drops have the same equilibrium interfacial tension. For a clean drop in the
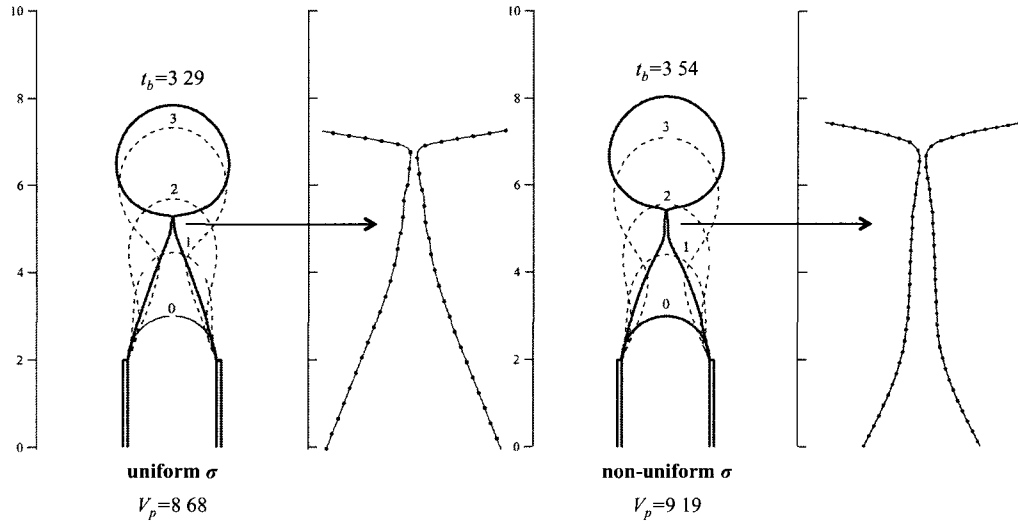
Figure 4-10: Comparison of drop shape evolution for (a) uniform σ and (b) non-uniform σ with $Pe_s = 10$, $x = 0.667$, and $Bi = 0.1$ is shown with an expanded view of the primary and secondary necks. $R_2/R_1 = 3$, $\chi = \lambda = 0.1$, $Re = 10$, $Ca = 0.1$, $Bo = 1$, and $Q_2/Q_1 = 5$. Shapes at every dimensionless time of 1 along with the final shape are shown.
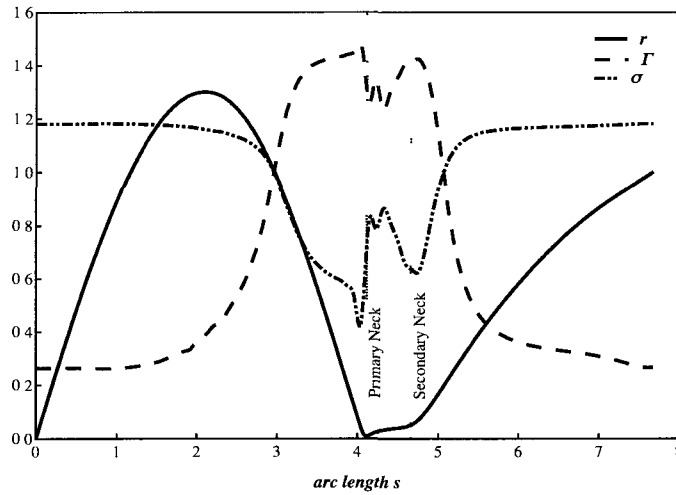
Figure 4-11: Drop shape, interfacial concentration, and interfacial tension as a function of arc length at breakup ($t = 3.54$) for $R_2/R_1 = 3$, $\chi = \lambda = 0.1$, $Re = 10$, $Ca = 0.1$, $Bo = 1$, $Q_2/Q_1 = 5$, $Pe_s = 10$, $x = 0.667$ and $Bi = 0.1$. The maximum packing limit is $\Gamma_\infty = 1.5$.

84
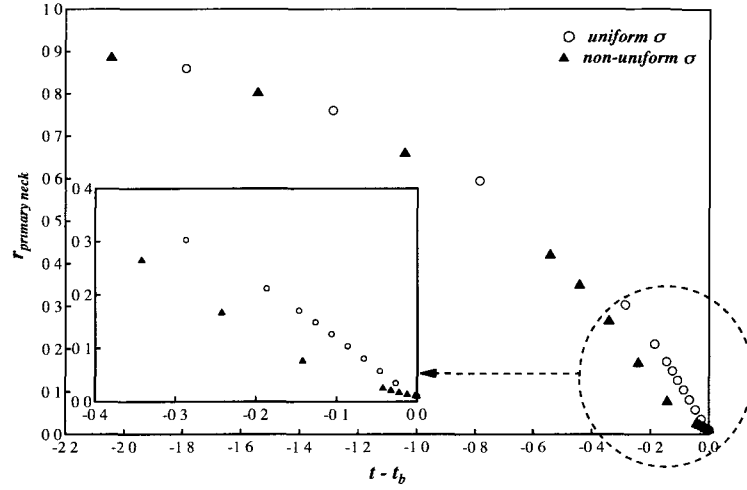
Figure 4-12: Primary neck radius versus time left to break up for the surfactant-free case and soluble surfactant case for $R_2/R_1 = 3$, $\chi = \lambda = 0.1$, $Re = 10$, $Ca = 0.1$, $Bo = 1$, $Q_2/Q_1 = 5$, $Pe_s = 10$, $x = 0.667$, and $Bi = 0.1$ (the last three parameters are for the soluble surfactant case).

absence of surfactants, the clean interfacial tension would be higher with $Bo = 0.82$ and $Ca = 0.08$ and the primary drop volume, $V_p = 9.87$ as well as the drop breakup time, $t_b = 3.64$ would be higher than the surfactant-laden drops.

To investigate the effect of the outer co-flowing flow on the drop formation process in the presence of soluble surfactants in the adsorption-desorption limit, the flow rate ratio Q_2/Q_1 is changed from 0 to 20 for $R_2/R_1 = 3$, $\chi = \lambda = 0.1$, $Re = 10$, $Ca = 0.1$, $Bo = 1$, $Pe_s = 10$, $x = 0.667$, and $Bi = 0.1$. The effect of increasing the outer fluid flow on the volume of the primary drop, breakup time, remnant drop length, and limiting drop length at breakup for the 'uniform σ' and 'non-uniform σ' cases are shown in Figs. 4-13 and 4-14. For $Q_2/Q_1 = 0$, 5, 15, and 20, the interface shapes at breakup for the 'non-uniform σ' case are also shown as insets in Fig. 4-13(a). The interface for the 'uniform σ' case at breakup are qualitatively similar to the corresponding 'non-uniform σ' shapes presented in Fig. 4-13(a). Similar to the

85

surfactant-free results explained earlier, the outer co-flowing fluid applies increasing viscous shear stress on the inner fluid as the flow rate ratio increases. As a result, drops breakup faster with primary drops of smaller size as seen in Fig. 4-13 and longer lengths of remnant drop shapes which first increase and then decrease as seen in Fig. 4-14.

The presence of Marangoni stresses slows down the primary neck formation and causes the time for breakup to increase for all flow rate ratios studied as seen in Fig. 4-13. However, as the outer flow rate is increased, the retardation of drop break up caused by surfactants reduces. As the flow rate ratio increases, the stronger outer flow pulls more of the surfactants away from the neck region as seen in Fig. 4-15 where the surfactant concentration along the interface at breakup is compared for $Q_2/Q_1 = 0$ and 15. For $Q_2/Q_1 = 15$, the surfactants accumulate at the apex of the drop and not nearly as much near the neck region compared to the drop with no co-flowing flow. The increased breakup time for the 'non-uniform σ' case results in larger primary drop volumes for all the flow rate ratios studied. The increase in primary drop volume due to the surfactant mass transfer effect reduces as the flow rate ratio increases with the primary drop volume being nearly identical for the 'uniform σ' and 'non-uniform σ' cases for $Q_2/Q_1 = 20$. The limiting drop length and the length of remnant drop at breakup is also higher for the 'non-uniform σ' case and the difference is more pronounced for $Q_2/Q_1 > 15$.

Next, the equilibrium fractional coverage of the surfactants is increased from $x = 0.1$ to $x = 0.9$ to determine its effect on the drop and necking dynamics. In this comparison, while the equilibrium fractional coverage changes, the equilibrium interfacial tension for all the drops is the same. This implies that the drop with the higher equilibrium fractional coverage, say $x = 0.9$, has a higher clean interfacial tension ($\sigma_c = 1.61$) while a drop with a lower equilibrium fractional coverage, say
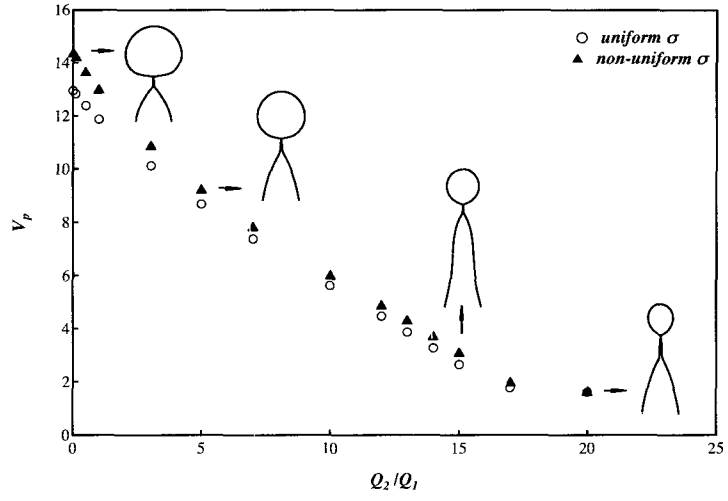
(a)
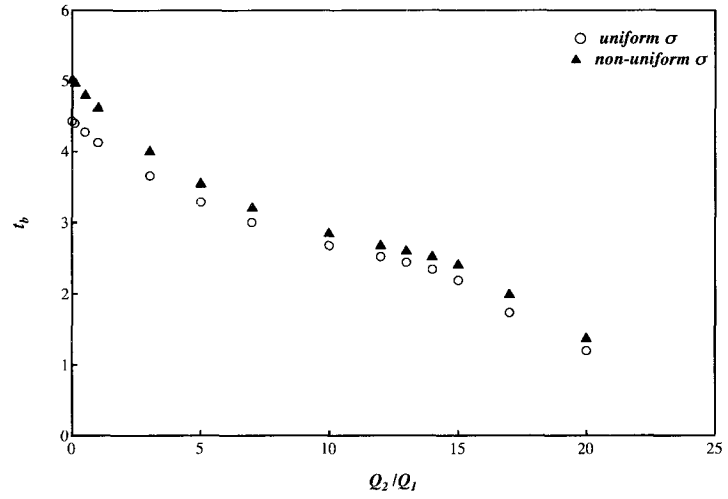
(b)

Figure 4-13: The effect of flow rate ratio on the (a) primary drop volume and (b) breakup time for $R_2/R_1 = 3$, $\chi = \lambda = 0.1$, $Re = 10$, $Ca = 0.1$, $Bo = 1$, $Pe_s = 10$, $x = 0.667$, and $Bi = 0.1$ (the last three parameters are for the soluble surfactant case).
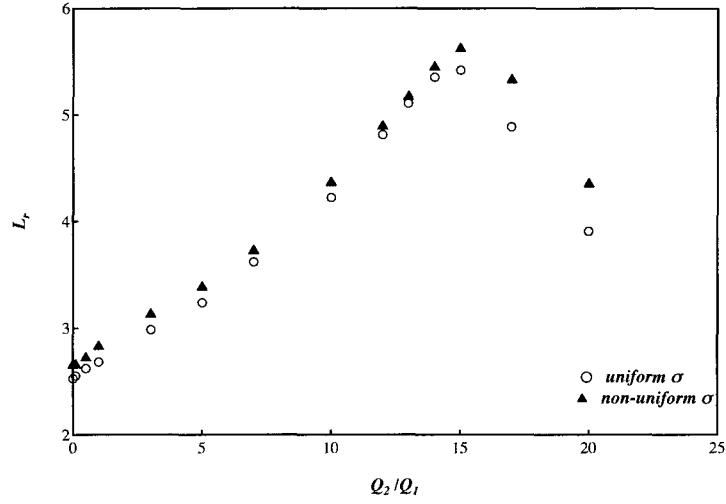
(a)
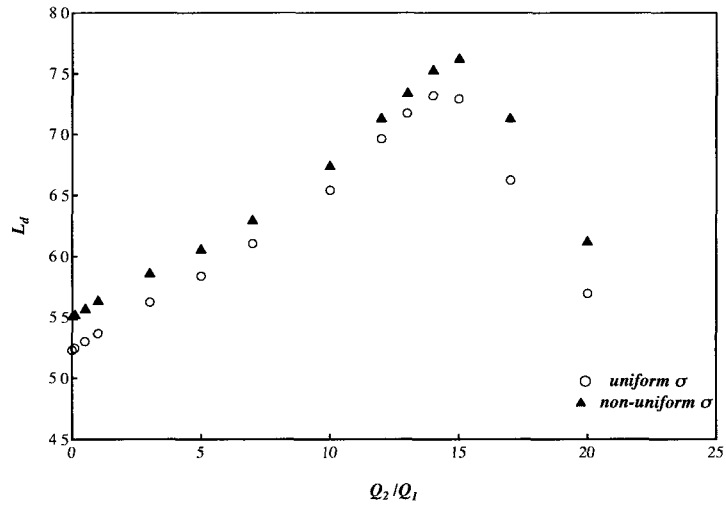
(b)

Figure 4-14: The effect of flow rate ratio on the (a) length of remnant drop and (b) limiting drop length at breakup for $R_2/R_1 = 3$, $\chi = \lambda = 0.1$, $Re = 10$, $Ca = 0.1$, $Bo = 1$, $Pe_s = 10$, $x = 0.667$, and $Bi = 0.1$ (the last three parameters are for the soluble surfactant case).

88
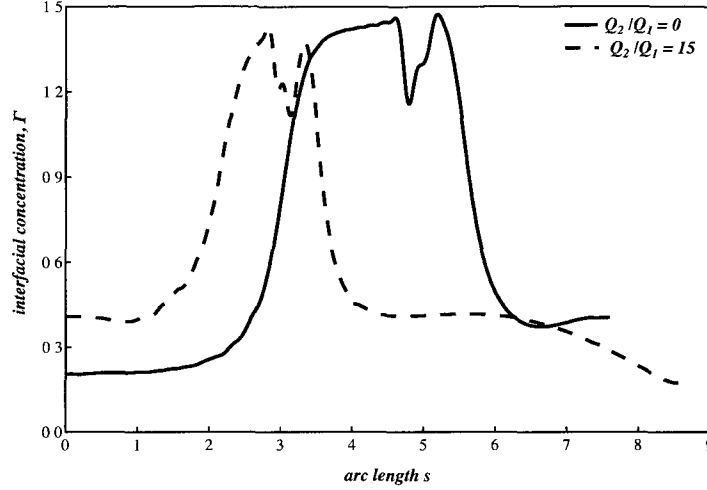
Figure 4-15: The surfactant concentration along the interface at breakup for $Q_2/Q_1 = 0$ and $Q_2/Q_1 = 15$ for $R_2/R_1 = 3$, $\chi = \lambda = 0.1$, $Re = 10$, $Ca = 0.1$, $Bo = 1$, $Pe_s = 10$, $x = 0.667$ and $Bi = 0.1$.

$x = 0.4$ has a lower clean interfacial tension ($\sigma_c = 1.09$). Since the surfactants get washed away from the apex of the drop and accumulate in the neck region, the average interfacial tension of the drop with $x = 0.9$ is higher than that of a drop with $x = 0.4$. This is seen more clearly in Fig. 4-16 where the interfacial tension along the interface at breakup is plotted for two drops with equilibrium interfacial coverages of 0.4 and 0.9. The average interfacial tension for the drops with $x = 0.4$ and 0.9 at breakup are 1.06 and 1.11 respectively. The effect of increasing the equilibrium fractional coverage, x on the drop volume and breakup time are shown in Fig. 4-17 and the limiting length and length of remnant drop are shown in Fig. 4-18 for $R_2/R_1 = 3$, $\chi = \lambda = 0.1$, $Re = 10$, $Ca = 0.1$, $Bo = 1$ $Pe_s = 10$ and $Bi = 0.1$. The results are shown in the absence ($Q_2/Q_1 = 0$) and presence ($Q_2/Q_1 = 5$) of co-flowing flow. The corresponding drop shapes at breakup are also shown as insets in Fig. 4-17(a). Due to the higher average interfacial tension at higher fractional coverages it is seen that as x increases, the primary drops are larger with more convex remnant drops and
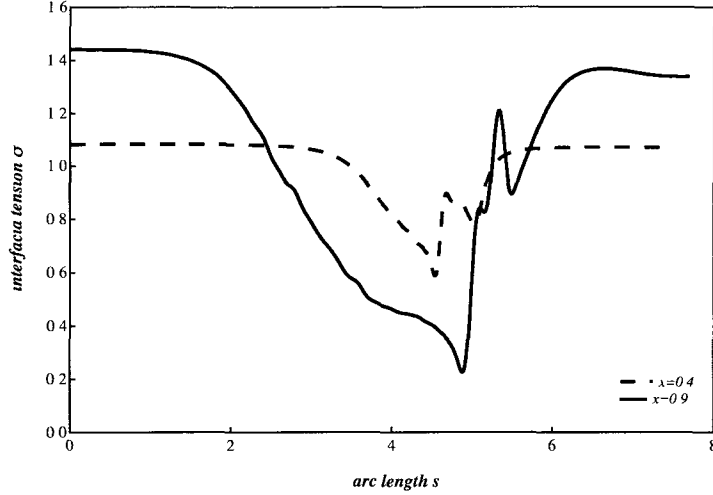
Figure 4-16: The interfacial tension along the interface at breakup for $x = 0.4$ and $x = 0.9$. Here, $R_2/R_1 = 3$, $Q_2/Q_1 = 0$, $\chi = \lambda = 0.1$, $Re = 10$, $Ca = 0.1$, $Bo = 1$, $Pe_s = 10$, and $Bi = 0.1$.

longer breakup times. The remnant drop length at breakup increases till $x = 0.667$ and then decreases. The limiting drop length at breakup increases for all coverages studied. Even though the trends for V_p, t_b, L_r, and L_d are similar in the absence and presence of outer co-flowing flow, the effect of equilibrium interfacial coverage is more pronounced in the absence of outer flow

As surfactants accumulate near the primary neck region, Marangoni flow slows down the necking rate of the primary neck as seen in Fig. 4-12. The secondary neck is also a site of fast interface contraction where surfactants will accumulate as can be seen in Fig. 4-11. This site, however, develops later, is much weaker with a lower surfactant accumulation than the primary neck region. As the primary neck thinning rate slows down close to breakup, the secondary neck formation catches up and the drop can now break either at the primary or the secondary neck. For a high enough equilibrium fractional coverage, the primary neck is completely suppressed and the drop breaks at the secondary neck [66]. It is observed that the breakup position

90
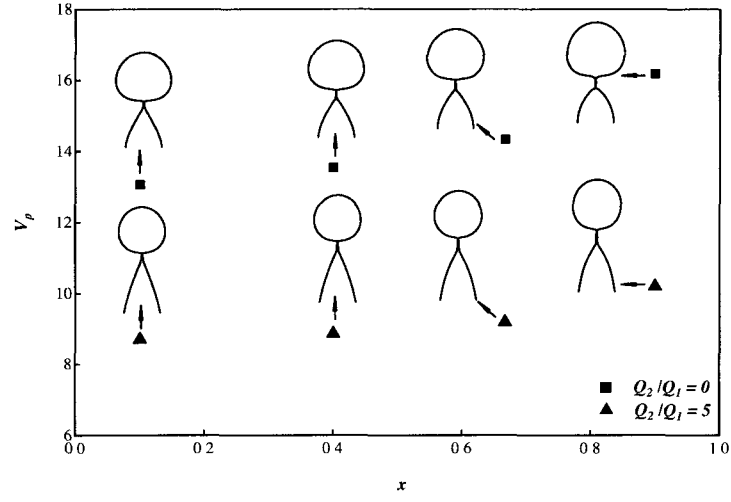
(a)
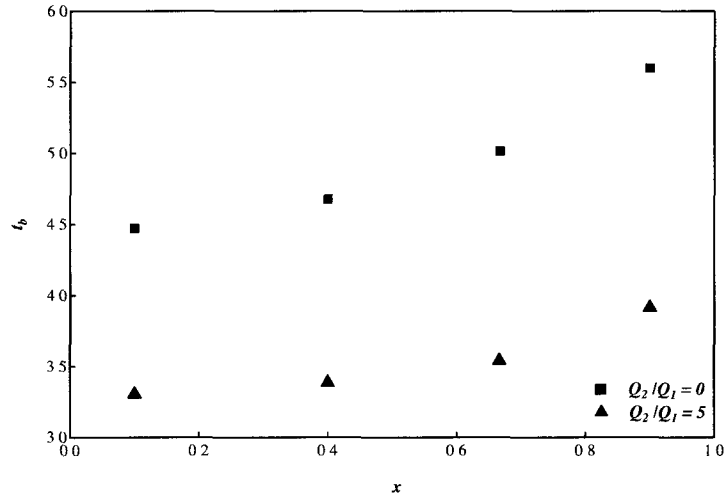
(b)

Figure 4-17: The effect of initial surface coverage on the (a) primary drop volume and (b) breakup time for $R_2/R_1 = 3$, $\chi = \lambda = 0.1$, $Re = 10$, $Ca = 0.1$, $Bo = 1$, $Pe_s = 10$, and $Bi = 0.1$ in the absence $(Q_2/Q_1 = 0)$ and presence $(Q_2/Q_1 = 5)$ of outer co-flowing fluids.
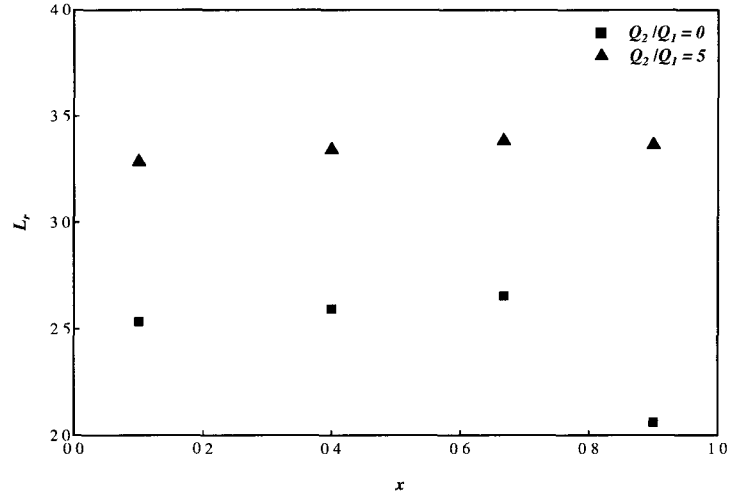
(a)
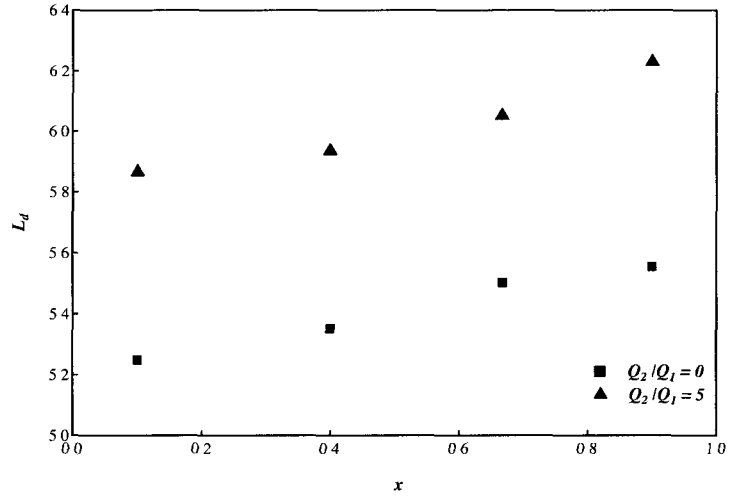
(b)

Figure 4-18: The effect of initial coverage on the (a) length of the remnant drop and (b) limiting drop length at breakup for $R_2/R_1 = 3$, $\chi = \lambda = 0.1$, $Re = 10$, $Ca = 0.1$, $Bo = 1$, $Pe_s = 10$, and $Bi = 0.1$ in the absence $(Q_2/Q_1 = 0)$ and presence $(Q_2/Q_1 = 5)$ of outer co-flowing fluids.

can be changed from the primary neck to the secondary neck when increasing x from 0.4 to 0.9 while keeping $Q_2/Q_1 = 0$ as seen in Fig. 4-19(a). As x increases from 0.4 to 0.9, more surfactants adsorb above the primary neck reducing the interfacial tension near the primary neck region. This can be seen in the large region near the primary neck with the lowest interfacial tension for $x = 0.9$ in Fig. 4-16. Larger Marangoni stresses at $x = 0.9$ retard the drop breakup, slow down the necking rate of the primary neck, and allow the secondary neck to develop more rapidly. As a result, the drop breaks at the primary neck for $x = 0.4$ and at the secondary neck for $x = 0.9$. Breakup of drop at the secondary neck turns out to be beneficial in suppressing satellite drop formation [66, 149]. As seen earlier, the outer co-flowing flow washes away surfactants from the neck region, weakening the Marangoni stresses. At the high fractional coverage of $x = 0.9$, if an outer co-flowing fluid is introduced, the break up position for the drop can be changed back from the secondary neck to the primary neck. This can be seen in Fig. 4-19(b) where starting with the case of $x = 0.9$ and $Q_2/Q_1 = 0$, the outer flow rate ratio is increased to $Q_2/Q_1 = 10$.

The impact of adsorption-desorption kinetics of soluble surfactants on the drop shape and necking process is investigated by varying Bi from 0.0001 to 5 while keeping the equilibrium surface coverage, $x = 0.9$. For these drops, the clean interfacial tension in the absence of surfactants is 1.61. The primary drop volume at breakup and the breakup time as a function of Bi for both $Q_2/Q_1 = 0$ and 5 are shown in Fig. 4-20. The dashed lines in Fig. 4-20 show the values of the limiting cases. The insoluble surfactant limit corresponds to $Bi = 0$ and $Bi = \infty$ corresponds to the 'uniform σ' case. The interface shapes at breakup for small ($Bi = 0.0001$), moderate ($Bi = 0.1$) and high ($Bi = 5$) Biot numbers are shown as insets in Fig. 4-20. In the insoluble limit ($Bi = 0$), no surfactant can be added to the drop after time $t = 0$. As the drop evolves, its surface area increases several-fold while the

x = 0.4   x = 0.667   x = 0.9

(a)

$Q_2/Q_1 = 0$ $Q_2/Q_1 = 5$ $Q_2/Q_1 = 10$

(b)
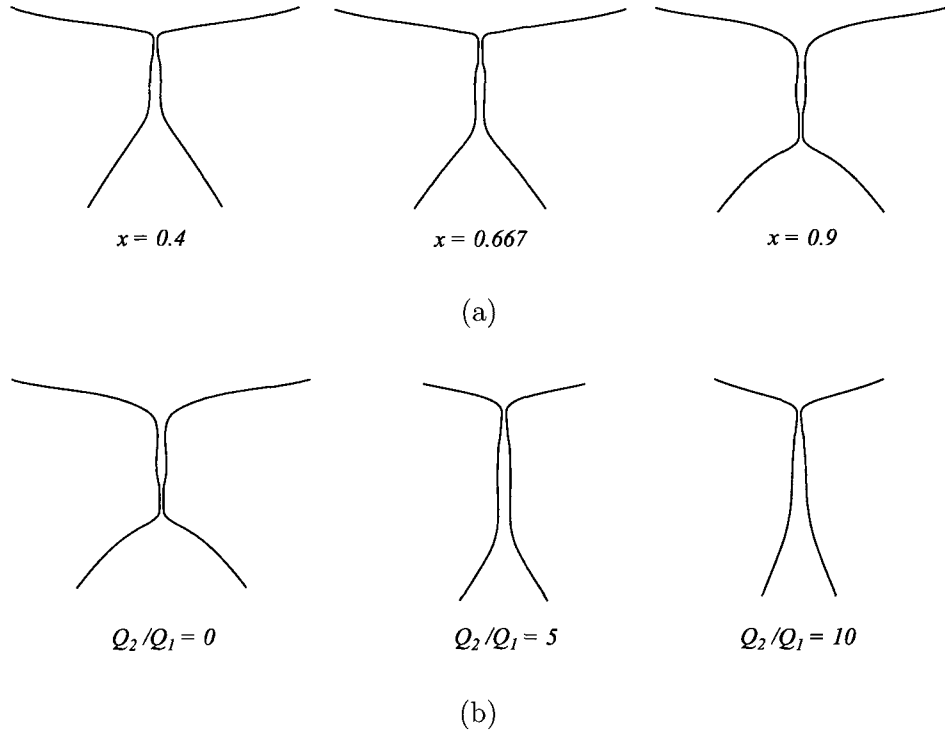
Figure 4-19: Neck formation modes are affected by (a) the interfacial coverage x and (b) the flow rate ratio Q_2/Q_1. for $R_2/R_1 = 3$, $\chi = \lambda = 0.1$, $Re = 10$, $Ca = 0.1$, $Bo = 1$, $Pe_s = 10$, and $Bi = 0.1$.

total amount of surfactant remains the same. Hence, the average interfacial tension for this drop is close to the clean interfacial tension everywhere except in the neck region where the surfactants accumulate. As the Biot number increases, the rate of adsorption-desorption to the interface increases and the average interfacial tension of the interface reduces leading to smaller primary drop volumes. In Fig. 4-20, for small to moderate Biot numbers, the primary drop volume decreases marginally with increasing Bi and decreases more rapidly for $Bi > 0.05$. On the other hand, the breakup time increases marginally with Biot number for $Bi < 0.05$ and decreases more rapidly for $Bi > 0.05$. The trends are similar in the absence ($Q_2/Q_1 = 0$) and presence ($Q_2/Q_1 = 5$) of co-flowing outer flow. However, the effect of Biot number is more pronounced in the absence of the outer co-flowing flow. This is due to the weakening effect of the co-flowing fluid on the surfactant distribution in the neck region.

For the range of parameters considered in this study, the effect of changing the adsorption-desorption kinetics has a stronger effect on the necking process. The length of the remnant drop and the limiting drop length at breakup as a function of Biot number are seen in Fig. 4-21 in the absence ($Q_2/Q_1 = 0$) and presence ($Q_2/Q_1 = 5$) of outer co-flowing flow. In the absence of outer flow, the remnant drop length decreases with Biot number till $Bi = 0.1$ and then increases with increasing Biot number. The limiting drop length on the other hand increases marginally with Biot number for $Bi < 0.1$ and then decreases more rapidly with Biot number. For $Bi < 0.05$ and $Bi > 0.5$, the drops break at the primary neck whereas for $0.05 \leq Bi \leq 0.5$, the drops break at the secondary neck. This transition from primary to secondary to primary neck is seen clearly in the neck profiles at breakup shown for $Bi = 0.0001$, 0.1, and 5 in Fig. 4-22 for $R_2/R_1 = 3$, $\chi = \lambda = 0.1$, $Re = 10$, $Ca = 0.1$, $Bo = 1$, $Q_2/Q_1 = 0$, $Pe_s = 10$, and $x = 0.9$. This trend was also observed
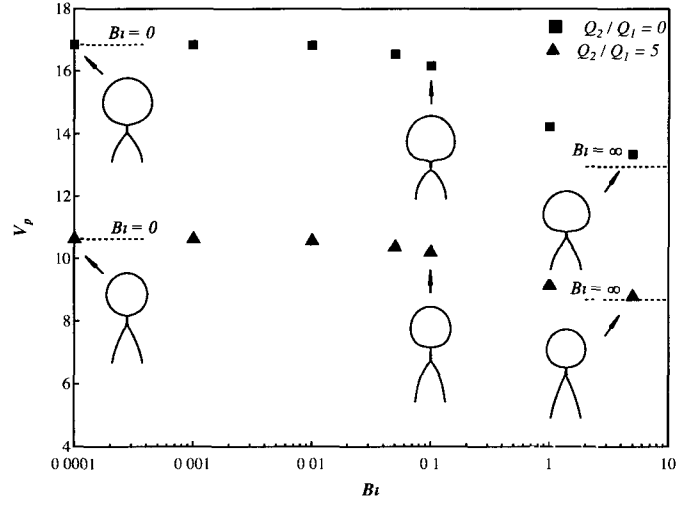
(a)
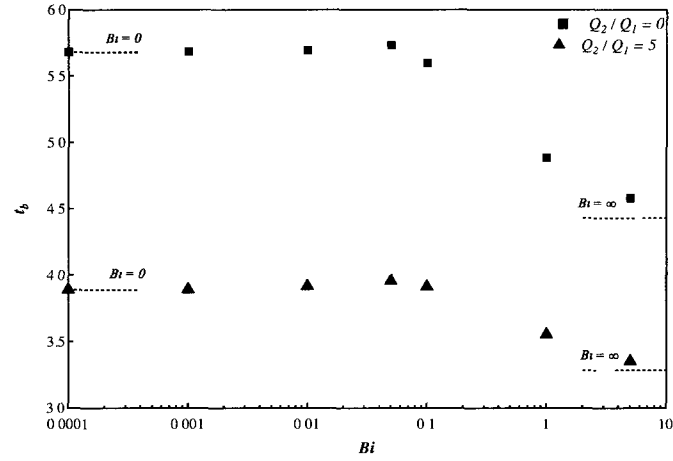
(b)

Figure 4-20: The effect of Biot number on the (a) primary drop volume and (b) breakup time for $R_2/R_1 = 3$, $\chi = \lambda = 0.1$, $Re = 10$, $Ca = 0.1$, $Bo = 1$, $Pe_s = 10$, and $x = 0.9$ in the absence and presence of outer co-flowing fluids. The dashed lines show the values for the 'uniform σ' limit $(Bi = \infty)$ and insoluble limit $(Bi = 0)$.

in the recent work on the effect of adsorption-desorption kinetics of soluble surfactants on the drop necking in a quiescent liquid [66]. In the presence of outer co-flowing flow, the Marangoni stresses are diluted and all the drops break at the primary neck. The remnant drop length at breakup first increases with Biot number for $Bi < 1$ and then decreases with Biot number. The limiting drop length at breakup also increases with Biot number for $Bi < 0.1$ and then decreases with Biot number.

Surfactants can also completely suppress the formation of a neck. Jin et al. [66] developed a phase diagram for the no-necking regime as a function of fractional coverage of surfactant, x versus the Biot number, Bi. For any given Bi value, a critical fractional coverage exists beyond which the drop dynamics enters a no-necking regime. Here it is shown that the phase diagram can be shifted to lower coverage, x values by confining the flow between walls even in the absence of outer co-flowing flow. Fig. 4-23 shows the effect of the outer tube diameter on the drop evolution for drops with $\chi = \lambda = 0.1$, $Re = 10$, $Ca = 0.1$, $Bo = 1$, $Q_2/Q_1 = 0$, $Pe_s = 10$, $x = 0.667$, and $Bi = 0.1$. As the diameter of the outer tube is reduced from $R_2/R_1 = 5$ to $R_2/R_1 = 3$, the additional wall shear results in a more prolate primary drop and a more convex remnant drop. The drop takes longer to break and the primary drop volume increases consistent with the numerical simulations by Zhang [149]. If the diameter of the outer tube further is decreased to $R_2/R_1 = 2$, the formation of the neck is completely suppressed. This is more clearly seen in the plot of neck radius as a function of time for $R_2/R_1 = 2$, $\chi = \lambda = 0.1$, $Re = 10$, $Ca = 0.1$, $Bo = 1$ $Q_2/Q_1 = 0$, $Pe_s = 10$, $x = 0.667$ and $Bi = 0.1$ in Fig. 4-24 where the neck starts to form at t 6.5, t 9.5, and t 12.5 but eventually fails. The simulations were stopped at $t = 14$ as it was certain that the drop would not break. As the outer co-flowing fluid has the effect of weakening Marangoni stresses, it is expected that as the flow rate ratio increases, the critical equilibrium coverage at which the drop fails
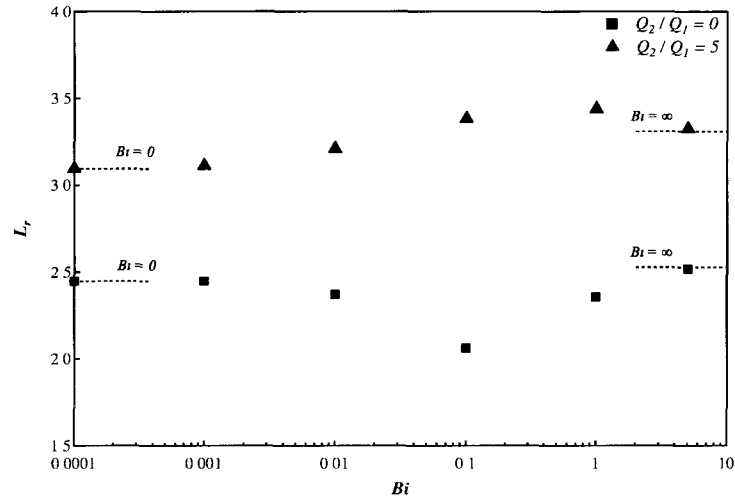
(a)
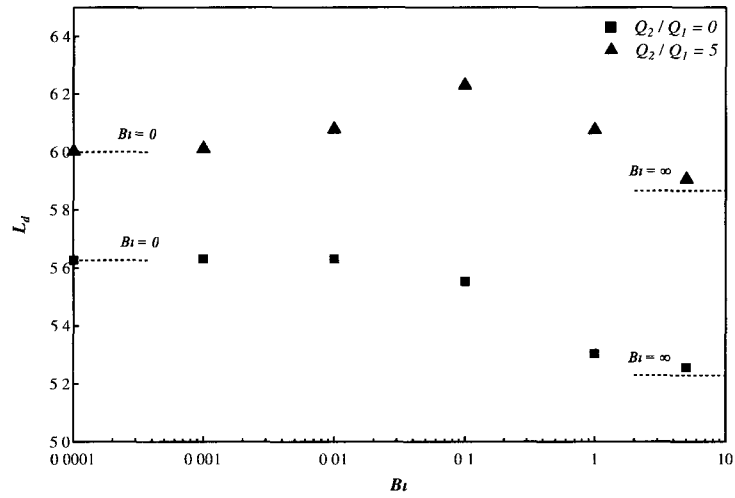
(b)

Figure 4-21: The effect of Biot number on the (a) length of the remnant drop and (b) limiting drop length for $R_2/R_1 = 3$, $\chi = \lambda = 0.1$, $Re = 10$, $Ca = 0.1$, $Bo = 1$, $Pe_s = 10$, and $x = 0.9$ in the absence and presence of outer co-flowing fluids.
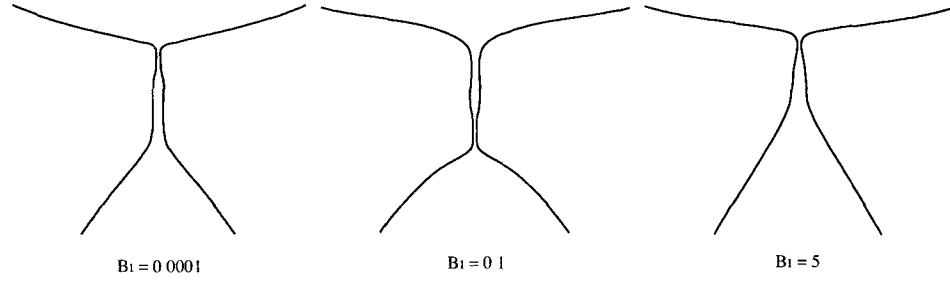
Figure 4-22: Necking dynamics is affected by Bi for $R_2/R_1 = 3$, $\chi = \lambda = 0.1$, $Re = 10$, $Ca = 0.1$, $Bo = 1$, $Q_2/Q_1 = 0$, $Pe_s = 10$, and $x = 0.9$.

to neck increases.

4.5.4 Results for Shear-thinning Fluids

While the numerical code developed can be used to simulate situations where either drop or bulk or both phases are shear-thinning, here results are presented for the formation of a shear-thinning drop in a co-flowing Newtonian fluid. The apparent drop viscosity as a function of shear rate is described by the Carreau model Eq. 2.34. The effect of a shear-thinning drop phase is discussed by considering three sets of Carreau model parameters as described in Section 2.3. First, a Newtonian drop fluid with $n_1 = 1$ is considered. Second, a weakly shear-thinning drop fluid with $\alpha_1 = 0.5, \beta_1 = 0.5$, and $n_1 = 0.5$ is considered. Finally, a strongly shear-thinning drop fluid with $\alpha_1 = 10, \beta_1 = 0.002$, and $n_1 = 0.3$ is considered. The apparent viscosity as a function of shear rate for these three fluids is shown in Fig. 2-6. The effect of surfactants and the flow rate ratio Q_2/Q_1 on the drop formation dynamics for these three fluid types is presented and discussed. For these simulation results, density ratio, $\chi = 0.1$, viscosity ratio, $\lambda_0 = 1$, Reynolds number, $Re = 10$, capillary number, $Ca = 0.1$, Bond number, $Bo = 1$, and $R_2/R_1 = 3$. For surfactant systems, the elasticity number, $E = 0.164$, and surface Peclet number, $Pe_s = 10$.

99
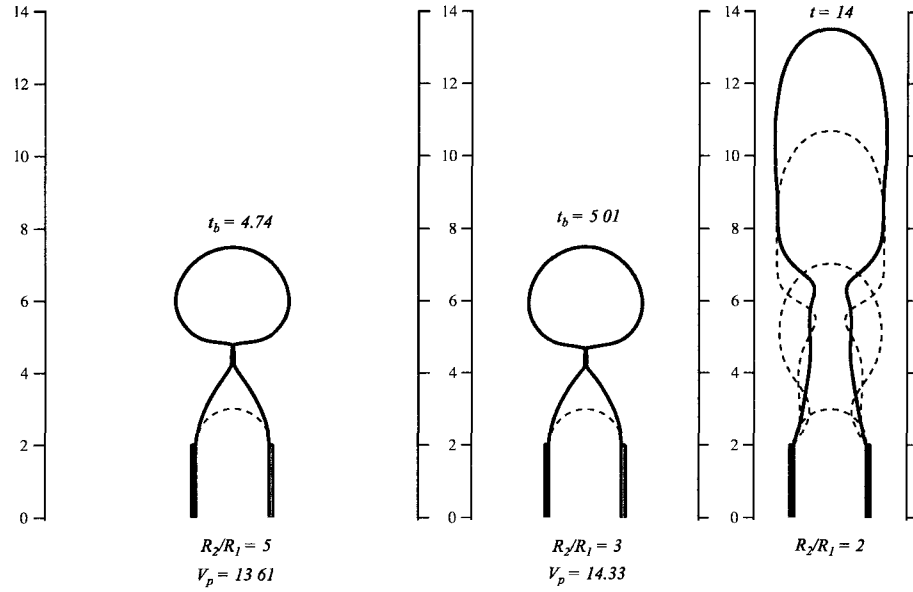
Figure 4-23: The effect of outer tube diameter on drop evolution dynamics in the surfactant-laden system for $\chi = \lambda = 0.1$, $Re = 10$, $Ca = 0.1$, $Bo = 1$, $Pe_s = 10$, $x = 0.667$, $Bi = 0.1$, and $Q_2/Q_1 = 0$. Shapes at every dimensionless time of 5 along with the final shape are shown.
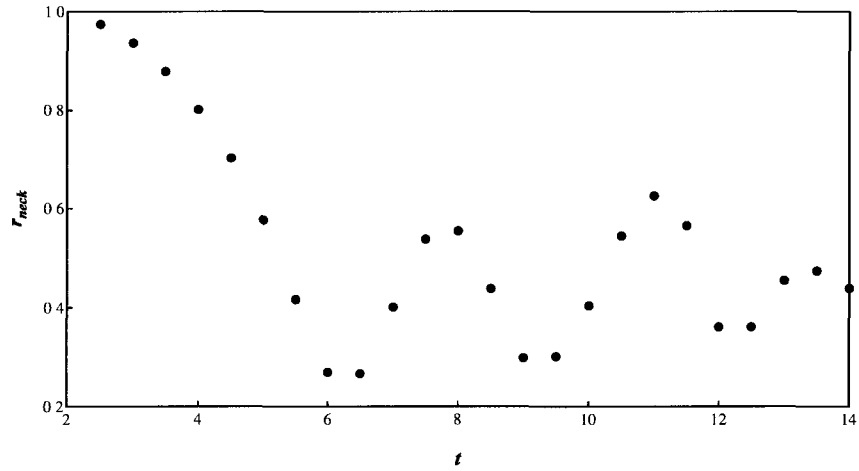
Figure 4-24: Neck radius as a function of time for $R_2/R_1 = 2$, $\chi = \lambda = 0.1$, $Re = 10$, $Ca = 0.1$, $Bo = 1$, $Q_2/Q_1 = 0$, $Pe_s = 10$, $x = 0.667$, and $Bi = 0.1$.

In the absence of surfactants, the evolution of drop shapes for the Newtonian, weakly shear-thinning, and strongly shear-thinning drop fluids is shown in Fig. 4-25 for $Q_2/Q_1 = 5$. In the absence of surfactants, the highly viscous Newtonian drop breaks with a long thread as shown in Fig. 4-7(a). For a weakly shear-thinning drop fluid, the drop breaks faster and the length of the thread is reduced. This result is consistent with the Newtonian results about the viscosity ratio effect shown in Fig. 4-7(a). It has also been observed in previous studies on drop formation in the absence of outer co-flowing fluid [39, 38, 143]. As the drop phase becomes strongly shear-thinning, the drop breaks even faster with a much shorter thread. The viscosity distribution inside the drop for the strongly shear-thinning drop is also shown on the right of the result in Fig. 4-7(c). Blue color for viscosity indicates regions of low viscosity and red color indicates regions of high viscosity. As expected, near the centerline of the inner tube, the shear rate is the smallest and the corresponding viscosity is the largest. For the bulk of the drop, the viscosity is very low, $\mu_1 < 0.1$ while the viscosity of the bulk fluid is 1. The drop phase is unable to resist the shearing of the outer fluid causing it to break easily.

Effect of surfactants on the drop formation process for Newtonian, weakly shear-thinning, and strongly shear-thinning drops are presented in Fig. 4-26 and Table 4.1. Similar to the Newtonian results, two scenarios are considered. If the mass transport of surfactants to the interface is fast compared to convection, the surfactant concentration remains constant with $\sigma = 1$, defined earlier as the 'uniform σ' case. When the surfactant transport is slow as compared to surface convection, the 'non-uniform σ' case is realized. For these results, $R_2/R_1 = 3$, $\chi = 0.1$, $\lambda_0 = 1$, $Re = 10$, $Ca = 0.1$, $Bo = 1$, $Q_2/Q_1 = 5$, $Pe_s = 10$, $x = 0.667$, and $Bi = 0.1$. The comparison of shapes at breakup between the 'uniform σ' case and the 'non-uniform σ' case in Fig. 4-26 shows that surfactants in general have a retarding effect on the drop formation pro-
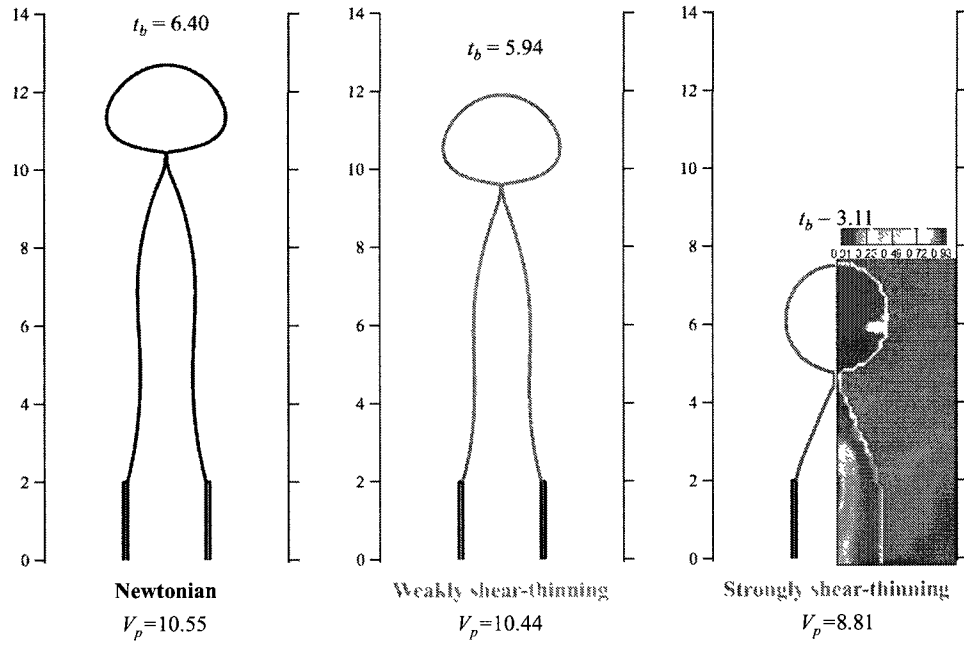
Figure 4-25: The shapes at breakup for Newtonian ($n_1 = 1$), weakly shear-thinning ($n_1 = 0.5$, $\beta_1 = 0.5$, and $\alpha_1 = 0.5$), and strongly shear-thinning ($n_1 = 0.3$, $\beta_1 = 0.002$, and $\alpha_1 = 10$) drops for $R_2/R_1 = 3$, $\chi = 0.1$, $\lambda_0 = 1$, $Re = 10$, $Ca = 0.1$, $Bo = 1$, and $Q_2/Q_1 = 5$. The contour plot of viscosity is also shown on the right hand of the third shape.
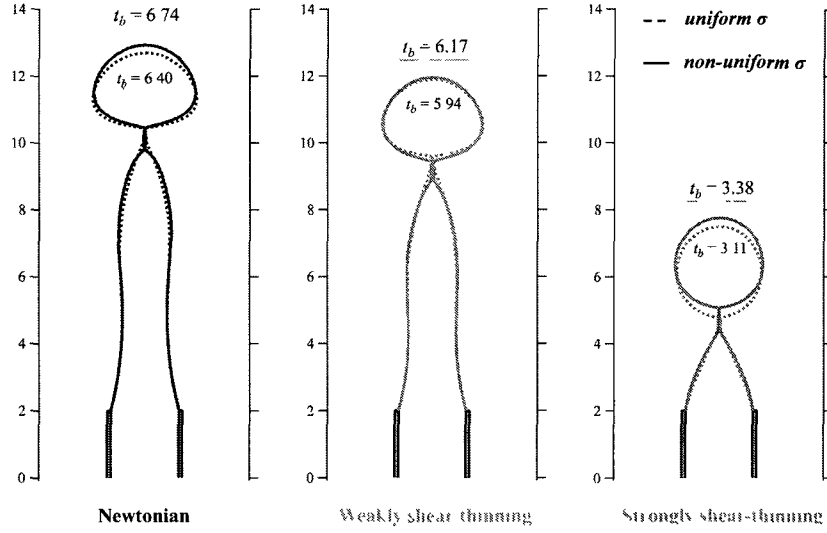
Figure 4-26: The comparison of shapes at breakup between the 'uniform σ' case and the 'non-uniform σ' case for Newtonian, weakly shear-thinning, strongly shear-thinning drops for $R_2/R_1 = 3$, $\chi = 0.1$, $\lambda_0 = 1$, $Re = 10$, $Ca = 0.1$, $Bo = 1$, $Pe_s = 10$, $x = 0.667$, and $Bi = 0.1$ (the last three parameters are for the soluble surfactant case). The solid line indicates the 'non-uniform σ' case, and the dash line indicates the 'uniform σ' case.

cess. This retardation effect of non-uniform distribution of soluble surfactants on the breakup is also seen clearly in the comparison of t_b, V_p, L_r, and L_d in Table 4.1. Only for weakly shear-thinning drop phase, the length of remnant drop is slightly shorter for 'non-uniform σ' case than 'uniform σ' case. The retarding effect is most pronounced for the strongly shear-thinning drop fluid as seen in Fig. 4-26 and only these drop fluids are considered for studying the effect of flow rate ratio.

The effect of the outer co-flowing flow on the drop formation process is presented for the 'uniform σ' and the 'non-uniform σ' case for flow rate ratio Q_2/Q_1 from 0.1 to 15. The effect of increasing the outer fluid flow on the primary drop volume, breakup time, remnant drop length, and limiting drop length at breakup for the 'uniform σ' and 'non-uniform σ' cases is shown in Figs. 4-27 and Fig. 4-28. For $Q_2/Q_1 = 0.1$,

103

Table 4.1: The effect of shear-thinning drop rheology on the primary drop volume, breakup time, length of remnant drop, and limiting drop length at breakup for $R_2/R_1 = 3$, $\chi = 0.1$, $\lambda_0 = 1$, $Re = 10$, $Ca = 0.1$, $Bo = 1$, $Pe_s = 10$, $x = 0.667$, and $Bi = 0.1$ (the last three parameters are for the soluble surfactant case).

		t_b	V_p	L_r	L_d
Newtonian	uniform σ	6 39	10 55	8 405	10 687
	non-uniform σ	6 74	10 94	8 408	10 926
Weakly shear-thinning	uniform σ	5 94	10 44	7 557	9 904
($n_1 = 0\ 5$, $\beta_1 = 0\ 5$, $\alpha_1 = 0\ 5$)	non-uniform σ	6 17	10 81	7 415	9 963
Strongly shear-thinning	uniform σ	3 11	8 81	2 713	5 492
($n_1 = 0\ 3$, $\beta_1 = 0\ 002$, $\alpha_1 = 10$)	non-uniform σ	3 38	9 31	3 034	5 754

5, and 15, the interface shapes at breakup for the 'non-uniform σ' case are also shown as insets in Fig. 4-27(a). The interface for the 'uniform σ' case at breakup are qualitatively similar to the corresponding 'non-uniform σ' shapes presented in Fig. 4-27(a) In the absence of surfactants, the shear stress caused by increasing the outer flow increases and drops break faster with smaller drop sizes as seen in Fig. 4-27. Due to the squeezing action of the outer flow, remnant drop length and limiting drop length at breakup also increase with increasing outer flow as seen in Fig. 4-28. When surfactants are present, they retard the thinning of the primary neck leading to longer breakup times and larger drop volumes as seen in Newtonian fluids. Furthermore, as the outer flow is increased, surfactants are washed away from the neck region reducing the Marangoni stresses at higher flow rate ratios. This is confirmed by Fig. 4-29 where the surfactant distribution on the drop interface at breakup is plotted for $Q_2/Q_1 = 0.1$ and $Q_2/Q_1 = 15$. The retardation effect of surfactants is diminished at higher flow rate ratios as the difference between the 'uniform σ' and 'non-uniform σ' results decreases for $Q_2/Q_1 = 15$ compared to $Q_2/Q_1 = 0.1$.

Finally, the shear-thinning drop rheology also affects necking dynamics for drops.
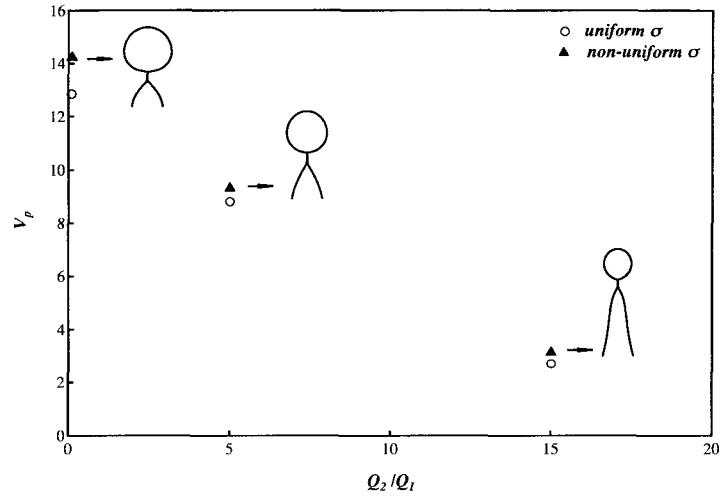
(a)
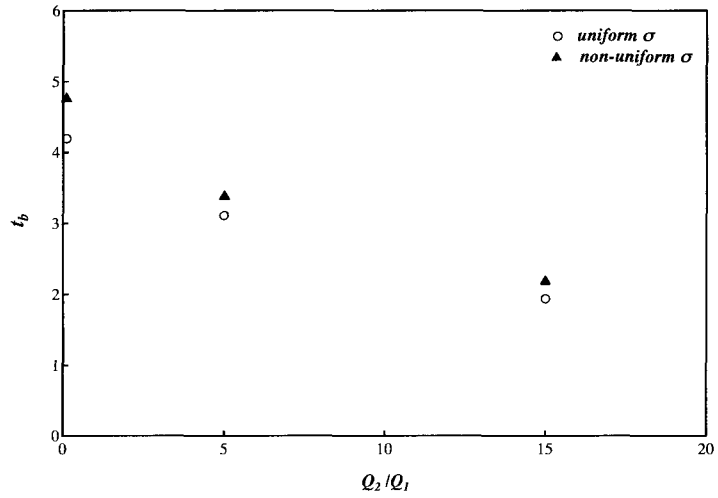
(b)

Figure 4-27: The effect of flow rate ratio on the (a) primary drop volume and (b) breakup time for the formation of the strongly shear-thinning drops in a Newtonian co-flowing fluid with $n_1 = 0.3$, $\beta_1 = 0.002$ and $\alpha_1 = 10$, $R_2/R_1 = 3$, $\chi = 0.1$, $\lambda_0 = 1$, $Re = 10$, $Ca = 0.1$, $Bo = 1$, $Pe_s = 10$, $x = 0.667$, and $Bi = 0.1$ (the last three parameters are for the soluble surfactant case).
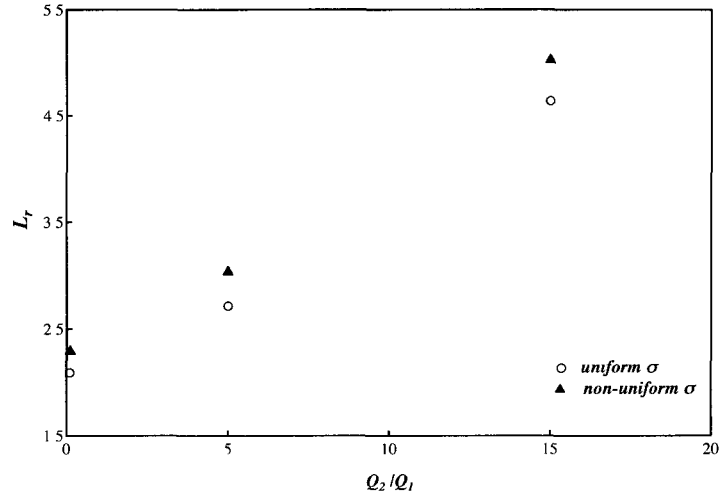
(a)
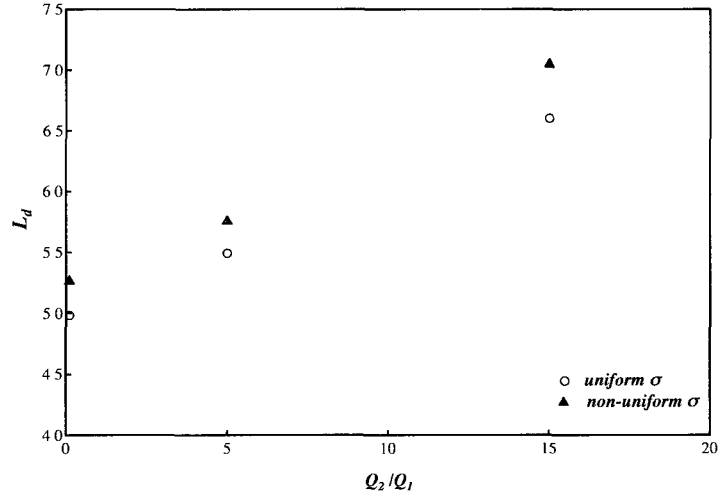
(b)

Figure 4-28: The effect of flow rate ratio on the (a) length of remnant drop and (b) limiting drop length at breakupfor the formation of the strongly shear-thinning drops ($n_1 = 0.3$, $\beta_1 = 0.002$ and $\alpha_1 = 10$) in a Newtonian co-flowing fluid with $R_2/R_1 = 3$, $\chi = 0.1$, $\lambda_0 = 1$, $Re = 10$, $Ca = 0.1$, $Bo = 1$, $Pe_s = 10$, $x = 0.667$, and $Bi = 0.1$ (the last three parameters are for the soluble surfactant case).

106
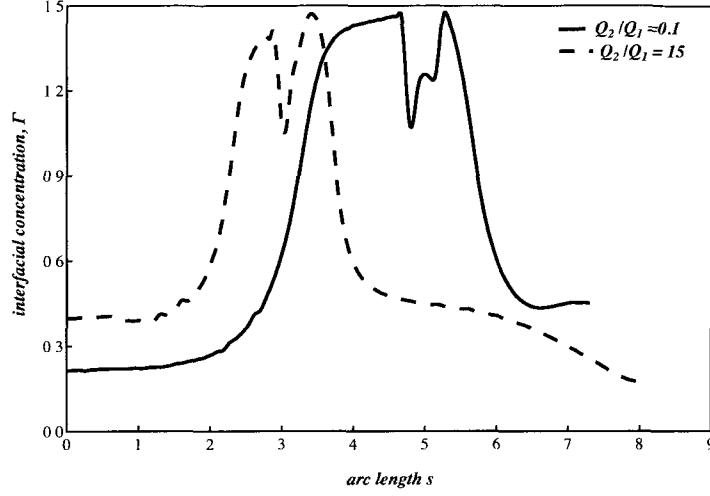
Figure 4-29: The surfactant concentration along the interface at breakup of strongly shear-thinning drops ($n_1 = 0.3$, $\beta_1 = 0.002$ and $\alpha_1 = 10$) for $Q_2/Q_1 = 0.1$ and $Q_2/Q_1 = 15$ for $R_2/R_1 = 3$, $\chi = 0.1$, $\lambda_0 = 1$, $Re = 10$, $Ca = 0.1$, $Bo = 1$, $Pe_s = 10$, $x = 0.667$, and $Bi = 0.1$.

The drop interface shape and the surfactant distribution on the drop surface at breakup for a Newtonian and a strongly shear-thinning drop is shown in Fig. 4-30. For this result, the drop viscosity is small compared to the bulk phase viscosity, $\lambda_0 = 0.1$. In addition, $R_2/R_1 = 3$, $\chi = 0.1$, $Re = 10$, $Ca = 0.1$, $Bo = 1$, $Q_2/Q_1 = 5$, $Pe_s = 10$, $x = 0.9$, and $Bi = 0.1$. The Newtonian drop in this case breaks at the primary neck as seen in the expanded view of the neck region in Fig. 4-30. For the strongly shear-thinning drop fluid, the neck not only shows breakup at the secondary neck but shows the formation of multiple satellite drops as seen in the expanded view of the neck region in Fig. 4-30. This shows that breakup at the secondary neck does not always help in suppressing satellite drop formation.

0 50 0 66 0 81 0 96 1 11   0 50 0 66 0 81 0 96 1 11

Newtonian   Strongly shear-thinning
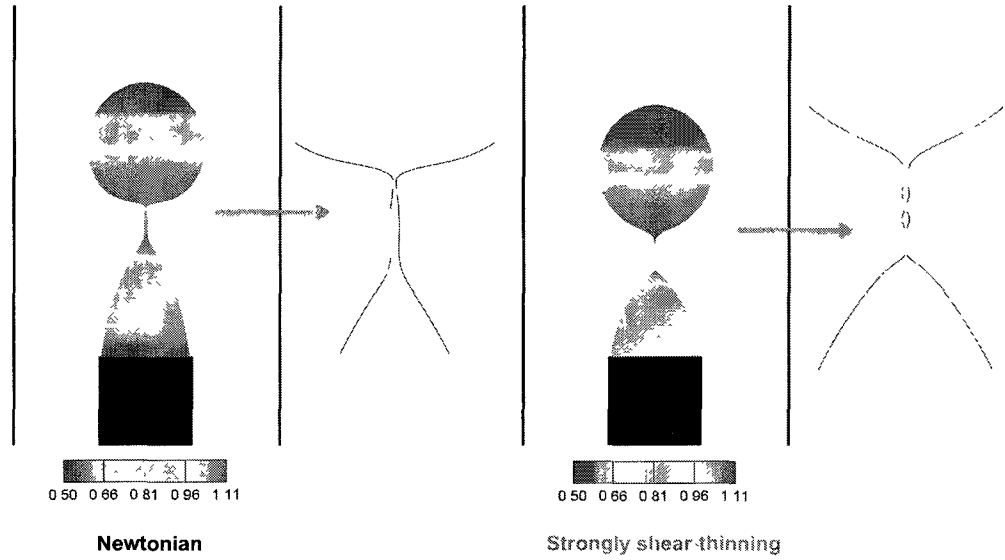
Figure 4-30: The comparison of shapes and necks at breakup between the Newtonian drop formation and the strongly shear-thinning drop ($n_1 = 0.3$, $\beta_1 = 0.002$ and $\alpha_1 = 10$) formation in to a Newtonian co-flowing fluid with $Q_2/Q_1 = 5$ in the presence of soluble surfactants in the adsorption-desorption limit with interfacial coverage of $x = 0.9$ for $R_2/R_1 = 3$, $\chi = 0.1$, $\lambda_0 = 0.1$, $Re = 10$, $Ca = 0.1$, $Bo = 1$, $Q_2/Q_1 = 5$, $Pe_s = 10$, $x = 0.9$, and $Bi = 0.1$. The surfactant concentration along the interface at breakup is shown as the contour plot inside the drop shape with red indicating the high surfactant concentration while blue indicating the low surfactant concentration.

Chapter 5

Drops Rising in a Tube

The motion of deformable drops through a tube is important in a number of natural and industrial processes such as enhanced oil recovery. During primary oil recovery, the natural pressure in the oil well is sufficient to drive the oil out of the reservoir. As the reservoir depletes in time, secondary recovery techniques are employed where fluids are injected to displace the oil out of unsaturated fractures in oil reservoirs. When both of them fail to bring the oil out from the depleted reservoir, tertiary or enhanced oil recovery techniques are used to mobilize the oil droplets lodged inside the reservoir pores [10, 57]. One enhanced oil recovery technique is surfactant-flooding where surfactant solutions are injected into the reservoir to force out the oil trapped in depleted oil reservoirs by capillary and viscous forces. Understanding the interplay of interfacial, viscous, inertial, and gravitational forces as well as the confinement of the fracture walls on the motion and deformation of oil droplets can provide important clues for improved oil recovery [71].

5.1   Model Problem

The system consists of an axisymmetric viscous drop of density ρ_1 and viscosity μ_1 rising through a quiescent immiscible viscous liquid of density ρ_2 and viscosity μ_2
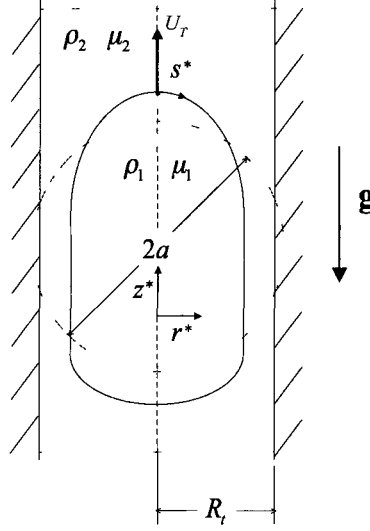
Figure 5-1: Schematic of the drop rising process through a quiescent immiscible viscous liquid.

in a cylindrical tube of radius R_t as shown in Fig. 5-1. Both phases are treated as incompressible fluids. The gravitational vector $\mathbf{g} = -g\mathbf{e}_z$, points in the negative z–direction. The drop migration velocity is denoted as U_T^* along the axis of the channel. In the following mathematical description, the reference frame is attached to the center of mass of the rising drop so that the tube wall moves downwards relative to drop with the drop migration velocity. The drop size is characterized by the radius of a spherical drop, a, of the same volume as seen by the dashed line in Fig. 5-1. Therefore, $a = (3V_d/4\pi)^{1/3}$ where V_d is the volume of the drop.

The numerical model presented in Chapters 2 and 3 are implemented to study the process of drops rising in a tube as shown in Fig. 5-1. Specifically, the numerical model will be used to:

110

- identify parameters governing the steady shapes and terminal velocities for drops rising in a confined tube,

- determine how surfactants adsorbed at the drop interface affect the mobility and deformation of the rising drop, and

- investigate the effects of a shear-thinning drop or bulk rheology on the dynamics of rising drops in a quiescent fluid in a confined tube.

In Section 5.2, the modification to the mathematical formulation presented in Chapter 2 to solve the drop rising problem is discussed. The numerical algorithm used to obtain the solution is presented in Section 5.3. The current state of knowledge for the drop rising problem is discussed in Section 5.4 and the results of this work are presented in Section 5.5.

5.2 Mathematical Formulation

As seen in Fig. 5-1, the flow domain is axisymmetric about the z^*-axis and the solution is obtained for the fluid on one $rz-$plane with the bounds $0 \leq r^* \leq R_t$ and $-Z_{max} \leq z^* \leq Z_{max}$. Z_{max} is chosen such that the axial length of the simulation domain does not affect the steady shape and mobility of the drops. A non-inertial reference frame attached to the center of mass of the rising drop is employed for the drop rising problem so that the tube wall moves in the opposite direction relative to drop with the drop migration velocity. Under the non-inertial reference frame, the two-phase flow is governed by the mass and momentum conservation equations in the same forms as Eqs. 2.1 - 2.3, but the modified pressure is expressed as

$$P_i^* = p_i^* - \rho_i \mathbf{g} \cdot \mathbf{x}^* + \rho_i \frac{dU_T^*}{dt^*} \mathbf{k} \cdot \mathbf{x}^* = p_i^* + \rho_i g z^* - \rho_i \frac{dU_T^*}{dt^*} z^*, \qquad (5.1)$$

where U_T^* is the migration velocity or terminal velocity of the drop, and $\mathbf{k}$ is the unit vector pointing in the direction of gravity. dU_T^*/dt^* gives the acceleration of the reference frame. If either phase is non-Newtonian, the Carreau model in Eq. 2.33 is used to describe the viscosity of the shear-thinning fluid. In the presence of surfactants, the Langmuir interfacial equation of state in Eq. 2.18 is applied to describe the relationship between the local interfacial tension, σ^* and the local surfactant concentration, Γ^*. The surfactant mass balance equation in Eq. 2.22 is used to solve for the local surfactant concentration Γ^*. The governing equations are solved subject to initial and boundary conditions prescribed at the fluid domain boundaries and the two-phase interface. The initial guess for the drop interface depends on the drop size, a. If $a/R_t \leq 0.9$, a spherical drop interface is assumed as the initial drop shape while a cylinder with two hemispherical caps is assumed as the initial shape for large drops with $a/R_t > 0.9$. If surfactants are present, the initial surfactant concentration at the interface is set equal to the equilibrium interfacial concentration, that is, $\Gamma^* = \Gamma_{eq}$ along the drop interface.

The boundary conditions imposed at the two-phase interface are described in Eqs. 2.4 and 2.6, and due to the non-inertial frame of reference, the stress jump across the interface is given as

$$(P_1^* - P_2^*)\,\mathbf{n} + (\tau_2^* - \tau_1^*) \cdot \mathbf{n} = \sigma^* \mathbf{n}\,(\nabla^* \cdot \mathbf{n})$$
$$- \nabla_s^* \sigma^* + (\rho_2 - \rho_1)\,(\mathbf{g} \cdot \mathbf{x}^*)\,\mathbf{n} - (\rho_2 - \rho_1)\,\frac{dU_T^*}{dt^*}\,(\mathbf{k} \cdot \mathbf{x}^*)\,\mathbf{n}. \quad (5.2)$$

In addition, boundary conditions at the flow domain boundaries are needed. No-slip and impermeable boundary conditions are imposed at the solid tube walls as

$$\left. \begin{aligned} u_{2r}^* &= 0 \\ u_{2z}^* &= -U_T^* \\ \tfrac{\partial P_2^*}{\partial r^*} &= 0 \end{aligned} \right\} \text{ at } r^* = R_t. \quad (5.3)$$

112

The symmetry boundary condition is applied along the central axis as

$$\left. \begin{array}{l} \frac{\partial \mathbf{u}_1^*}{\partial r^*} = 0 \\[2mm] \frac{\partial P_1^*}{\partial r^*} = 0 \end{array} \right\} \text{ at } r^* = 0. \qquad (5.4)$$

At the far-field boundaries zero gradients of velocity and pressure are applied,

$$\left. \begin{array}{l} \frac{\partial \mathbf{u}_2^*}{\partial z^*} = 0 \\[2mm] \frac{\partial P_2^*}{\partial z^*} = 0 \end{array} \right\} \text{ at } z^* = \pm Z_{max}. \qquad (5.5)$$

For non-dimensionalizing the governing equations, the tube radius R_t is chosen as the characteristic length, the buoyancy velocity $(\rho_2 - \rho_1)gR_t^2/\mu_2$ is chosen as the characteristic velocity, and the pressure is scaled with $(\rho_2 - \rho_1)gR_t$. The dimensionless drop size is defined as, $\kappa = a/R_t$. The clean interfacial tension σ_o for the surfactant-free simulations or the equilibrium interfacial tension σ_{eq} for the surfactant-laden simulations is chosen as the characteristic interfacial tension. The dimensionless governing equations defined between $0 \leq r \leq 1$ and $-Z_{max}/R_t \leq z \leq Z_{max}/R_t$ are then given by

$$\nabla \cdot \mathbf{u} = 0, \qquad (5.6)$$

$$\bar{\rho} Re \left(\frac{\partial \mathbf{u}}{\partial t} + \mathbf{u} \cdot \nabla \mathbf{u} \right) = -\nabla P + \nabla \cdot \left(\bar{\mu} \left[(\nabla \mathbf{u}) + (\nabla \mathbf{u})^T \right] \right)$$
$$+ \frac{1}{Bo} \left[\nabla_s \sigma - \sigma \mathbf{n} (\nabla \cdot \mathbf{n}) \right] \delta_s + \left[1 - (1 - \chi) \frac{dU_T}{dt} Re \right] z \mathbf{n} \delta_s, \qquad (5.7)$$

where the dimensionless modified pressure is defined as

$$P_i = p_i + \rho_i g z - \rho_i (dU_T/dt) z. \qquad (5.8)$$

The dimensionless interfacial boundary conditions are given by Eqs. 2.10 and 2.12, and the stress jump reduces to

$$(P_1 - P_2) \mathbf{n} + (\tau_2 - \tau_1) \cdot \mathbf{n} =$$
$$\frac{1}{Bo} \left[\sigma \mathbf{n} (\nabla \cdot \mathbf{n}) - \nabla_s \sigma \right] - \left[1 - (1 - \chi) \frac{dU_T}{dt} Re \right] z \mathbf{n}. \qquad (5.9)$$

Due to the choice of the characteristic velocity, the capillary number reduces to the Bond number and only two dimensionless groups, namely, the Reynolds number and the Bond number are defined as

$$Re = \rho_2 U_1 R_1 / \mu_2, \tag{5.10}$$

$$Bo = (\rho_2 - \rho_1) g R_t^2 / \sigma_c. \tag{5.11}$$

If either phase is non-Newtonian, the dimensionless Carreau model in Eq. 2.34 is used to describe the viscosity of the shear-thinning fluid. In the presence of surfactants, Eqs. 2.26 and 2.23 are applied to determine the local interfacial tension along the interface, Γ. The surface Peclet number and the Biot number are then defined as

$$Pe_s = \frac{(\rho_2 - \rho_1) g R_t^3}{\mu_2 D_s}, \tag{5.12}$$

$$Bi = \frac{\alpha_s \mu_2}{(\rho_2 - \rho_1) g R_t}. \tag{5.13}$$

The elasticity number and equilibrium surface coverage have the same definition as Eqs. 2.24 and 2.25.

The dimensionless boundary conditions at the solid tube wall,

$$\left.\begin{aligned} u_{2r} &= 0 \\ u_{2z} &= -U_T \\ \tfrac{\partial P_2}{\partial r} &= 0 \end{aligned}\right\} \text{ at } r = 1 \tag{5.14}$$

and symmetry boundary conditions and far-field boundary conditions are imposed as

$$\left.\begin{aligned} \tfrac{\partial \mathbf{u}_i}{\partial r} &= 0 \\ \tfrac{\partial P_i}{\partial r} &= 0 \end{aligned}\right\} \text{ at } r = 0, \tag{5.15}$$

$$\left.\begin{aligned} \tfrac{\partial \mathbf{u}_2}{\partial z} &= 0 \\ \tfrac{\partial P_2}{\partial z} &= 0 \end{aligned}\right\} \text{ at } z = \pm Z_{max}/R_t. \tag{5.16}$$

114

5.3   Solution procedure

The hybrid VOF technique discussed in Chapter 3 is now modified and applied to solve the problem of drop rising in a tube via the single-fluid VOF formulation under the non-inertial reference frame as

$$\nabla^* \cdot \mathbf{u}^* = 0, \tag{5.17}$$

$$\tilde{\rho} \left(\frac{\partial \mathbf{u}^*}{\partial t^*} + \mathbf{u}^* \cdot \nabla^* \mathbf{u}^* \right) = -\nabla^* P^* + \nabla^* \cdot \left(\tilde{\mu} \left[(\nabla^* \mathbf{u}^*) + (\nabla^* \mathbf{u}^*)^T \right] \right)$$
$$+ \left[\nabla_s^* \sigma^* - \sigma^* \mathbf{n} (\nabla^* \cdot \mathbf{n}) - (\rho_2 - \rho_1) \mathbf{g} \cdot \mathbf{x}^* \mathbf{n} + (\rho_2 - \rho_1) \frac{dU_T^*}{dt^*} \mathbf{k} \cdot \mathbf{x}^* \mathbf{n} \right] \delta_s. \tag{5.18}$$

The dimensionless form is given by

$$\nabla \cdot \mathbf{u} = 0, \tag{5.19}$$

$$\bar{\rho} Re \left(\frac{\partial \mathbf{u}}{\partial t} + \mathbf{u} \cdot \nabla \mathbf{u} \right) = -\nabla P + \nabla \cdot \left(\bar{\mu} \left[(\nabla \mathbf{u}) + (\nabla \mathbf{u})^T \right] \right)$$
$$+ \frac{1}{Bo} \left[\nabla_s \sigma - \sigma \mathbf{n} (\nabla \cdot \mathbf{n}) \right] \delta_s + \left[1 - (1 - \chi) \frac{dU_T}{dt} Re \right] z \mathbf{n} \delta_s, \tag{5.20}$$

where $\bar{\rho} = 1 - (1 - \chi) \phi$ and $\bar{\mu} = 1 - (1 - \lambda) \phi$ and ϕ is the VOF function, which takes the value 1 for the drop phase and 0 for the bulk phase.

The interface is represented by Lagrangian marker particles with a parameter representation $(r_s (s), z_s (s))$ where s is the arc length starting from the apex of the drop. The initial shape of the drop is assumed to be spherical if the drop size $\kappa \leq 0.9$ and a cylinder with two hemispherical end caps otherwise. The VOF function ϕ and the continuous surface force are calculated in the entire domain. The velocity and pressure fields on the fixed grid are solved using Eqs. 5.19 and 5.20. Note that the terminal velocity of the drop, U_T is a variable that is solved for as part of the solution. The velocities of the marker particles on the moving grid at the interface are

115

determined by employing a linear interpolation based on the velocity fields obtained on the fixed grid. The marker particles are advected as material particles based on the kinematic condition to determine the new interface location using an explicit Euler scheme. As the interface continuously deforms, marker particles are added or removed at each time step to maintain the same level of discretization. A volume correction technique proposed by Ryskin and Leal [109] is adopted to preserve the drop volume. A scaling factor $\beta_v = V^n/V^0$ is used where V^n denotes the drop volume updated according to the kinematic condition at the nth time step and V^0 denotes the initial drop volume. Once the updated drop shape is obtained, the new ϕ field can be calculated for the next time step. For surfactant systems, starting with an equilibrium concentration of surfactants, $\Gamma = 1$, the surfactant concentration and interfacial tension are updated using Eqs. 2.23 and 2.26. The surface mass balance, Eq. 2.26, is solved using a finite difference formulation. For the cases with shear-thinning drop or bulk fluid, the viscosities are updated via the Carreau model in Eq. 2.34. This algorithm is repeated until drop shape and terminal velocity reach a steady state. The Eulerian and Lagrangian mesh sizes and time steps are chosen to ensure convergence of drop shape, velocity, and pressure fields for a chosen set of dimensionless parameters. A mesh size of at least 0.025 and a time step of at least 10^{-4} is used.

5.4   Literature Review

Most of previous work has been done to study the buoyancy-driven motion of drops and bubbles in confined domains under creeping flow conditions where inertial effects can be neglected, that is, $Re \ll 1$. Bretherton studied the motion of a long air bubble in a cylindrical tube using asymptotic analysis at small Reynolds and capillary

numbers [20]. For the case of buoyancy-driven motion of a long bubble, he found the

drop would rise only if Bond number, $Bo = (\Delta \rho g R_t^2/\sigma$, was greater than 0.842, where

$\Delta \rho$ was the difference in density between the two fluids, R_t was the tube radius, and

σ was the interfacial tension between the two fluids. He also found that the rise

velocity of the long bubbles, U, was independent of bubble size, which was described

by $Bo - 0.842 = 1.25Ca^{\frac{2}{9}} + 2.24Ca^{\frac{1}{3}}$. Here, Ca was the capillary number defined as

$Ca = \mu U/\sigma$ where μ was the viscosity of the ambient fluid. He also showed the film

thickness was proportional to $Ca^{\frac{2}{3}}$, and there was a wave-like appearance (bulge) at

the rear meniscus. Bretherton's analysis, however, was limited to vanishing values of

Ca with the error of about 10% for $Ca = 8 \times 10^{-5}$. The analysis was confirmed and

extended to larger values of Ca for $0.0001 \leq Ca \leq 0.1$ by Reinelt's numerical work

[103] on a finger rising in a vertical cylindrical tube under the effect of gravity. He used

a finite difference method in the creeping flow limit to obtain a relationship between

the Bond number and the capillary number and compared it with Bretherton's results.

In the limit of $Ca \rightarrow 0$, the numerical solution matched the asymptotic solution of

Bretherton. Borhan and Pallinti [16] experimentally investigated the buoyancy-

driven motion of viscous drops through vertical cylindrical capillaries under creeping

flow conditions for a wide range of viscosity ratios, density ratios, Bond numbers,

capillary numbers as well as drop sizes. They investigated the effects of the Bond

number and the viscosity ratio on the drop shape and terminal velocity. As the

Bond number increased, the drop became elongated, and the film thickness increased

to a plateau value. Furthermore, the film thickness seemed independent of the

viscosity ratio and agreed with the predictions by Bretherton [20] and Reinelt [103].

The retarding effect of the capillary wall was found to decrease as the Bond number

increased, or as the viscosity ratio of drop phase to bulk phase decreased. For a given

viscosity ratio, there was a limiting value of the Bond number beyond which the film

thickness reached a plateau value indicating that wall effect remained unchanged with further increase in the Bond number. For small Bond numbers, the terminal velocity as a function of drop size showed a local maxima due to the wall effect. For large Bond numbers, the terminal velocity seemed to increase monotonically with drop size. For both cases, the terminal velocity for large enough drop became independent of drop size. They also showed that the numerical solutions using the boundary integral method were in good agreement with the experimental measurements. They observed tip-streaming for large Bond numbers and at vanishing values of drop fluid viscosity compared to the bulk fluid viscosity due to the presence of surface-active impurities.

Some recent studies have considered the effect of inertia on the buoyancy-driven motion of drops and bubbles through a vertical tube at finite Reynolds numbers. Bozzi et al. [18] numerically studied the buoyancy-driven motion of deformable drops falling or rising in a cylindrical tube at intermediate Reynolds numbers using a Galerkin finite-element method. The radius of the tube was set to twice the radius of a sphere having the same drop volume. The drop and bulk fluids had the same viscosities. The density ratios were also close to unity, so similar results for falling or rising drops were expected. For capillary numbers ranging from 0.005 to 1, they found that the drops became oblate and even lost the rear convexity as inertia was increased by increasing Reynolds or Weber number. They observed novel hat-shaped drops. For the cases with capillary numbers less than 0.6, they plotted the streamlines for different Reynolds numbers and found that the disjoint recirculation zone with front and rear stagnation points grew, approached the drop from the rear, and eventually crossed the drop interface with increasing Reynolds number. Viana et al. [135] presented universal correlations to predict the terminal velocity of long bubbles in round pipes based on experimental data for wide ranges of tube buoyancy Reynolds numbers, $Re_B = (D^3 g(\rho_l - \rho_g)\rho_l)^{1/2}/\mu$ and Eotvos numbers, $Eo = g\rho_l D^2/\sigma$,

where D is the pipe diameter, and ρ_l and ρ_g are densities of liquid and gas phases. The normalized terminal velocity were formulated as functions of Re_B and Eo for large $Re_B > 200$, small $Re_B < 10$, and a transition region, $10 < Re_B < 200$. It was found that long bubble terminal velocity was independent of bubble volume. Taha and Cui presented numerical studies to investigate the buoyancy-driven and pressure-driven motion of single Taylor bubbles (long bubbles) in vertical cylindrical tubes [124] as well as in rectangular channels [125] using FLUENT software implemented with volume-of-fluid (VOF) method. They showed the bubble shape profile and wall stress distribution along the axis. The bubble shape was found to be dependent upon ambient liquid viscosity and surface tension but not on the bubble size. Mukundakrishnan et al. [85] numerically studied the wall effects on buoyant bubble rise in a finite cylinder filled with a viscous liquid by employing a front tracking finite difference method coupled with a level contour reconstruction of the front. They presented results of how bubbles with different shapes in infinite medium changed when applying the wall confinement. For a fixed volume of the bubble, rear recirculatory wakes would form in large cylindrical tubes resulting in lateral bulging and skirt formation in drop shape. When cylinder radius was reduced, the wake effects on bubble rise were reduced and elongated bubbles occurred with retarded motion due to increased drag. Li et al. [76] experimentally studied the buoyancy-driven motion of bubbles in circular and square channels over a range of Reynolds numbers at moderate capillary and Bond numbers. The steady shapes and terminal velocities of the bubbles as a function of the bubble size were determined. Bubbles in a circular channel were more prolate and rose slower than bubbles in a square channel with the same hydraulic diameter. As the Weber number increased, the bubble showed bubbles with a negative curvature at the rear of the bubble due to the increasing inertial effects. Feng used a Galerkin finite-element method with a boundary-fitted

mesh to study the buoyancy-driven motion of a bubble [45] in a round tube filled with a viscous liquid. Small bubbles exhibited similar behavior to bubbles moving in an infinite liquid and developed a spherical-cap when the Reynolds number was increased and the capillary number was not too small. Long bubbles exhibited a prolate nose-like shape with various tail shapes which could be adjusted by changing the Reynolds number and the Weber number. At a large Weber numbers, $We > 10$, the long bubble formed a concave profile with a "cup" at small Reynolds number and a "skirt" with sharply curved rims at larger Reynolds number. For Weber numbers less than 1, the bubble tail appeared rounded without large local curvatures though a slightly concave tail developed at larger Reynolds numbers. Non-uniform annular film with a bulge forming at the rim of the bubble tail was observed for small Weber numbers suggesting the surface tension effect could play a role.

Surfactant effects on the motion of fluid particles has been restricted to the motion of long bubbles under creeping flow conditions. Bretherton's theoretical work showed that the thickness of the liquid film separating the rising long bubble from the tube wall was proportional to $Ca^{2/3}$ [20]. However, the film thickness obtained experimentally was found significantly larger than theoretical values. He speculated that the film-thickening phenomena might be caused by small amount of surface impurities present at the bubble-liquid interface. The effect of surfactants on the liquid film thickness was studied theoretically (asymptotically) [36, 53, 98, 102, 116], numerically [50], as well as experimentally [112]. Compared to the surfactant-free case, both film-thinning and film-thickening were observed when surfactants were present. The film-thinning occurred when the mass transfer of surfactants was sorption-controlled at small bulk surfactant concentration [50, 53]. The film-thickening occurred when surfactant transport was controlled by bulk diffusion at small bulk surfactant concentrations [102] or when surfactant transport was controlled by sorption kinetics at

elevated bulk surfactant concentrations [116]. For large bubbles of a finite length, the film-thickening would be observed in diffusion-controlled regime only when the bubble length was larger than a critical value [98, 112]. The effect of surfactants on the shape and motion of bubbles and drops through a tube has been reported at small Reynolds numbers. Borhan and Pallinti [17] experimentally examined the shape and breakup of air bubbles and viscous drops translating through vertical cylindrical capillaries under the action of pressure and/or buoyancy forces in the creeping flow regime over a wide range of particle sizes and capillary number in various two-phase systems. They identified four distinct breakup modes: formation and growth of capillary waves at the interface, continuous stretching in the axial direction, tail-streaming, and penetration of a re-entrant cavity at the trailing end of the particle. They also determined the critical conditions for the onset of different modes. For all four breakup modes, the critical capillary number was found to be a decreasing function of particle size. It was also found that buoyancy forces could have a stabilizing effect on the breakup mechanism observed by Olbricht and Kung [93] for low viscosity-ratio drops, where a growing indentation at the trailing end of the drop developed into a penetrating jet of outer phase fluid. Almatroushi and Borhan [1] added various amounts of sodium dodecyl sulfate (SDS) into two specific gas-liquid and liquid-liquid systems in the bubble/drop rising experiments to study the effect of surfactant concentration of SDS on the buoyancy-driven motion of bubbles/drops in a cylindrical tube at low Reynolds numbers ($Re < 0.1$). For air bubbles, the presence of surfactants retarded the motion of small bubbles due to the development of adverse Marangoni stresses, while enhanced the motion of large bubbles by allowing them to deform away from the wall more easily. For viscous drops, the enhancement of mobility for large drops became more pronounced when increasing the surfactant concentration. Borhan and Mao [15] used a boundary integral method

in conjunction with a convective-diffusion equation to numerical study the effect of insoluble surfactants on the motion and deformation of viscous drops in Poiseuille flow through circular tubes at low Reynolds number. Surfactant concentration at the interface was described by a linear equation of state, which is typically valid in the dilute regime. While the drop shape was slightly affected by the presence of surfactants, more significant effects were found for the droplet velocity. They found large variations in surfactant concentration were produced across the interface of the drop and the resulting interfacial tension gradients led to Marangoni stresses that opposed surface convection and retarded the motion of the drop when surface Peclet number was increased. For large surface Peclet numbers, large Marangoni stresses immobilized the drop interface, and large deformations were required to satisfy the normal stress balance. Johnson and Borhan [68] extended Borhan and Mao's work [15] to numerically investigated the nondilute concentrations of insoluble surfactants on the drop shape and motion in Poiseuille flow through circular tubes in creeping flow. They still used the boundary integral method, but they applied the Frumkin adsorption framework which was able to describe the monolayer saturation and non-ideal surfactant interactions in the limit of high surface coverage instead of using a linear equation of state. Later, they extended their numerical work to study the effects of surfactant solubility [69]. It was found that the mechanism by which drop mobility was reduced changed from uniform retardation at low surface coverage to the formation of a stagnant cap at high surface coverage as the equilibrium surface coverage was increased. For large capillary numbers, they observed the destabilizing effect on transient drop shapes by accelerating the formation and development of the penetrating viscous jet that led to drop breakup, or by continuous elongation and pinch-off of a tail at the rear stagnation point. None of these studies considered the effect of inertia on the shape and motion of bubbles and drops translating in a tube

in the presence of surfactants.

In an unbounded domain, an increase in inertia leads to strong shape deformation of bubble/drop from a spherical shape to an oblate-ellipsoid to a spherical cap shape accompanying flow separation and wake formation at the rear stagnation point even without surfactants [35, 110] as well as with surfactants [128, 136]. In the presence of insoluble surfactants, the interface can be substantially retarded due to accumulation of surfactants at the rear stagnation point. When surfactants are bulk soluble, the surfactant gradients along the interface reduce making the interface more mobile [84, 136]. The surfactant concentration can be used to control the formation, size, and the ultimate disappearance of the wake [136]. Research has been conducted on the effect of surfactants on the flow around a spherical bubble/drop at finite Reynolds number in an unbounded domain, that is, bubble/drop size is sufficiently small compared to the tube diameter, where bubble/drop deformation is not very important [32, 44, 79, 83, 96, 126, 136, 151, 152]. Several studies assumed the bubble to be spherical that would not deform in the flow field [32, 44, 96, 126, 136, 151, 152] while others considered the deformation of bubbles/drops [79, 83]. Three regimes of surfactant transport were identified in the theoretical work: stagnant cap regime, uniformly retarded regime, and remobilization regime. Most of studies have focused on the stagnant cap regime where the interfacial convection dominated the bulk diffusion or kinetic fluxes [32, 44, 79, 83, 96, 126, 151, 152]. This regime commonly occurred when surfactant bulk concentration was low. To leading order, adsorbed surfactants behaved as if they were insoluble and swept to the back end of the particles where stagnant caps developed. Finite rates of both kinetic exchange and diffusive transport of surfactants were taken into account in the studies of this regime, and the relationship between surfactant concentration and cap angle were explored [32, 79, 96, 126]. Measurements of the terminal velocities of bubbles showed

a decrease in the terminal velocity with increasing bulk concentration of surfactants [44, 96, 151, 152]. In the other limit where the bulk concentration of surfactants was large, and the kinetic and bulk diffusive exchange were much faster than convection, this regime was called as remobilization regime since the distribution of surfactants at the interface tended to be uniform and Marangoni stresses tended to disappear [126, 136]. The regime in between when the rates of bulk diffusion and kinetic exchange of the surfactants were of the same order as the interfacial convection was named as uniformly retarded regime because the bubble surface became uniformly retarded [24, 25].

Numerical schemes have been developed to describe the surfactant effect on the motion and shapes of buoyancy-driven bubbles/drops through a tube in the presence of soluble surfactants at finite Reynolds numbers [7, 86, 148]. Ayyaswamy's group developed a front-tracking scheme and their numerical results showed that the bulk fluid in the vicinity of the interface might become depleted of surfactant when the location of the adsorptive interface got closer to the tube wall [7, 148]. Tasoglu et al. [128] pointed out the confinement effect of tube wall on the motion of buoyancy-driven bubbles in the presence of soluble surfactants at finite Reynolds numbers using a finite-different/front-tracking method developed by Muradoglu and Tryggvason [86]. They compared their numerical results for contaminated bubbles with the experimental results for solid sphere done by Clift et al. [28] for different tube wall radii, and showed the retardation effect of surfactants that make the contaminated bubble behavior more like a solid sphere. They also found that the wall had a considerable effect on the interfacial surfactant concentration when the ratios of tube radius to bubble radius was less than 2.5. However, most of these results were obtained in an unbounded domain. They recovered the stagnant cap regime for the bubble with oblate-ellipsoid shape at low elasticity and high interfacial Peclet numbers.

A number of studies were conducted to investigate the bubble motion in a quiescent viscoelastic fluid [5, 12, 74, 80, 56, 58, 105, 106, 107, 145]. Interesting phenomena such as cusp-formation [5, 80], velocity discontinuity [5, 58, 74, 80], and negative-wake formation [56, 58] were observed in viscoelastic fluid systems experimentally. A stability analysis of bubbles in viscoelastic flows was done by You et al. [145] using asymptotic and numerical techniques. They used the finitely extensible nonlinear elastic Chilcott-Rallison (FENE-CR) model to describe the viscoelastic fluids. They confirmed a cusp did form during bubble rising in a viscoelastic fluid. Moreover, the cusp formation and the velocity discontinuity for rising bubbles were also observed in viscoelastic solutions in the presence of surfactants such as surfactant micellar solutions in Belmonte's experiments [12], and surfactants can alter the conditions for the onset of the discontinuity of terminal velocity of rising bubbles shown in the experiments of Rodrigue and co-workers [105, 106, 107].

You et al. [144] developed a numerical method for simulating the drop motion in a viscoelastic two-phase system using a finite-volume formulation. The FENE-CR model was applied to described the viscoelastic phase. They applied this numerical method on a drop rising in a quiescent ambient fluid in a confined cylindrical tube [146]. They studied a Newtonian drop rising in a Newtonian suspending fluid, and showed a slightly negative curvature developed at the drop rear for larger Reynolds number and capillary numbers based on the terminal velocity of the drop. They then investigated both a Newtonian drop rising in a viscoelastic suspending fluid and a viscoelastic drop rising in a Newtonian suspending fluid. A cusp could be formed at the rear of the rising Newtonian drop in a viscoelastic fluid. They generally concluded that a prolate shape would be developed for a Newtonian drop rising in a viscoelastic fluid whereas an oblate shape would be developed for a viscoelastic drop rising in a Newtonian fluid. Researchers have attempted to isolate the shear-thinning effect in

viscoelastic fluids by preparing dilute solutions with low zero shear-rate viscosity in their experiments [89, 90, 91, 104] or modeling purely shear-thinning fluid in their simulations [89, 90, 91] to simplify the complex two-phase problems. Ohta et al. [89, 90, 91] conducted numerical simulations and experiments to study the dynamics of a Newtonian drop rising through a quiescent shear-thinning liquids. They first ignored the deformation of the drop shape and only consider a spherical drop rising in a cylindrical tube [89]. In their experiments, silicone oil drops were injected into diluted aqueous carboxymethyl cellulose (CMC) sodium salt and sodium acrylate polymer (SAP) solutions as weakly and strongly shear-thinning continuous phase liquids. They applied VOF/CSF method to numerically simulate the two-phase flow and the generalized Cross-Carreau model to describe the shear-thinning fluids. They showed that strongly shear-thinning liquid affected the flow field around a small spherical drop more strongly than the weakly shear-thinning liquid. Ohta et al. [90] extended their experiments and numerical model to account for the deformation of the drop. They showed that the deformable drop could greatly affect the local viscosity changes, and the stagnant flow field behind the drop induced a much higher viscosity region at the drop rear. Later, they extended their numerical work from two-dimensions to three-dimensions using a coupled level-set/volume-of-fluid method to simulate a deformable Newtonian drop rising through a quiescent shear-thinning liquids in a rectangular channel [91]. Their simulation reproduced the dynamics of drop rising well including the nonlinear wobbling effects associate with a sufficiently high Reynolds number. Rodrigue [104] conducted experiments to investigate the effect of surfactants on the deformation of non-Newtonian drops falling in a quiescent Newtonian liquid in a unconfined domain. They used corn oil as the Newtonian outer fluid, and polyacrylamide dissolved in aqueous glycerine as the shear-thinning drop fluid described by a power-law model. Different concentration of sodium dodecyl

126

sulphate (SDS) were introduced into this two-phase flow system, and the effect of SDS on rheological parameters of shear-thinning fluids could be neglected for their range of shear rates $(1 - 15s^{-1})$. They showed that the drop was more elongated when the concentration of the surfactant SDS was increased or the concentration of PAA was increased. They, however, pointed out that drop formation was mainly controlled by viscous and interfacial tension forces and the effects of shear-thinning and inertia were negligible.

5.5   Results and Discussion

The drop rising process is studied by running the simulations for the complete range of drop sizes, κ, for a specified set of dimensionless parameters such as Reynolds number, Bond number and so on. The simulations are run till a steady drop shape and the terminal velocity, U_T, is obtained. The terminal velocity, U_T, as a function of drop size, κ, is used to compare the results. In addition, the drop shape is quantified by the length of the drop, L, the width of the drop, B, and the deformation parameter, Δ. The length and the width of the drop are defined as the maximum axial and radial dimension of the drop at steady state. The deformation parameter is defined as

$$\Delta \equiv \frac{L - B}{L + B}. \tag{5.21}$$

Eq. 5.21 indicates that the drop shape is spherical when $\Delta = 0$, that is $L = B$. The drop is elongated in the direction of flow or prolate when $\Delta > 0$, that is $L > B$. Finally, an oblate or a drop elongated perpendicular to the direction of flow has $L < B$ and $\Delta < 0$. For the case of long drops, only the central region is chosen to measure the maximum radial length. Results are also presented in terms of the film thickness, δ, defined as the dimensionless minimum distance between the drop

interface and the capillary wall. For the case of long drops, film thickness in the central uniform region is reported.

5.5.1 Validation of numerical method

In order to validate the numerical scheme for drops rising in a confined tube, the numerical results in this study are compared with the experimental results of Borhan and Pallinti [16] where a viscous drop rises in a vertical precision-bore glass capillary. The experimental results used for comparison were for a suspending fluid of 84.2 wt % glycerol-water mixture with the density and viscosity of 1212 kg/m^3 and 80 $mPa \cdot s$, respectively. The drop fluid was a Dow Corning silicone fluid (DC510-100) with a density and viscosity of 990 kg/m^3 and 105 $mPa \cdot s$, respectively. The interfacial tension between the two phases was 26.8×10^{-3} N/m. Based on Borhan and Pallinti's experimental data, the dimensionless parameters for the numerical simulations are chosen as $\chi = 0.82$, $\lambda = 1.3$, $Re = 26$, and $Bo = 1.3$. Comparisons of steady shapes and terminal velocities for drop size of $\kappa = 0.58, 0.73, 0.92, 1.15,$ and 1.32 are shown in Fig. 5-2 and Fig. 5-3, respectively. There is good qualitative agreement between the numerical results and the experimental results.

5.5.2 Surfactant-free results for Newtonian fluids

For the surfactant-free results presented in this section, the density ratio $\chi = 0.1$ and the effect of viscosity ratio, λ, Reynolds number, Re, and Bond number, Bo, on the steady drop deformation and mobility is presented. First, a typical velocity volume curve for a system with $\chi = \lambda = 0.1$, $Re = 10$, and $Bo = 1$ is shown in Fig. 5-4. The drop shapes for some of the drop sizes are shown as insets in Fig. 5-4. The terminal velocity of the smallest drop of size $\kappa = 0.1$ is also compared with the Hadamard-
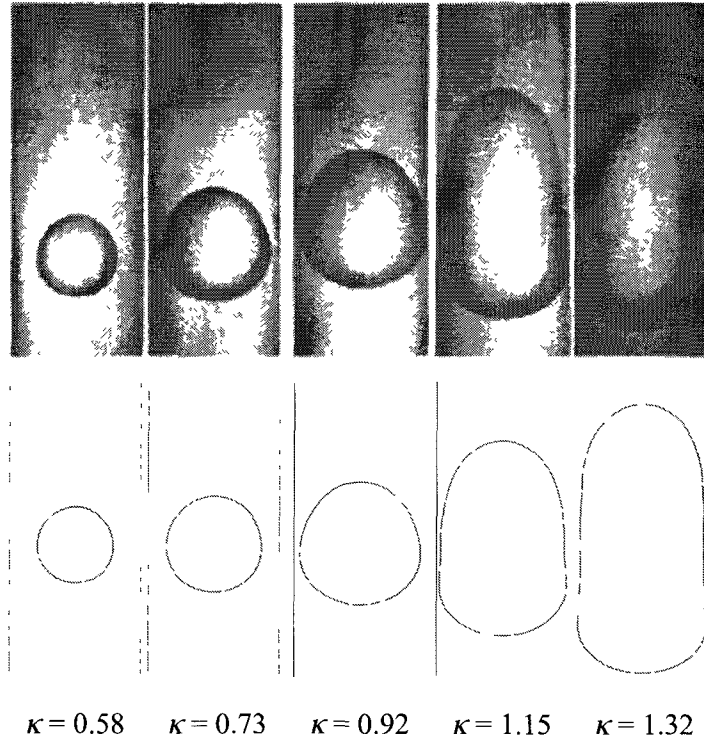
Figure 5-2: Comparison of steady drop shapes observed in Borhan and Pallinti's experimental work (top) and predicted in our numerical simulation (bottom).
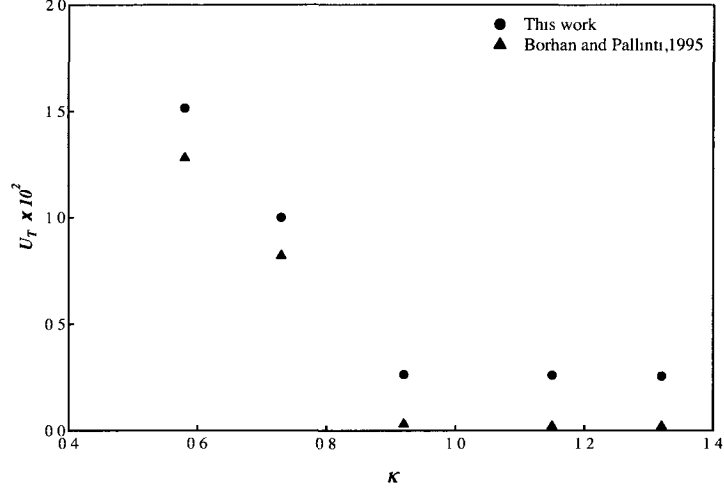
Figure 5-3: Comparison of terminal velocity as a function of drop size observed in Borhan and Pallinti's experimental work (triangle) and predicted in our numerical simulation (circle).

Rybczinki velocity shown as an open circle in Fig. 5-4. The Hadamard-Rybczinki equation gives the terminal velocity of a spherical drop rising through an ambient fluid in an unbounded domain and is given in dimensionless form as

$$U_{HR} = \frac{2}{3} \left(\frac{\lambda + 1}{3\lambda + 2} \right) \kappa^2. \tag{5.22}$$

For a drop size of $\kappa = 0.1$, the presence of the tube wall does not affect the drop mobility and the Hadamard-Rybczinki velocity is recovered. As the drop size increases, the terminal velocity first increases due to predominantly buoyancy effects. As the drop size becomes comparable to the tube size, the terminal velocity decreases due to the increased wall drag and it eventually reaches a constant value which is independent of the drop size. This is expected as shown in Bretherton's work [20].

To quantify the drop deformation, the drop width as a function of drop length, and the deformation parameter as a function of drop size are also plotted in Fig. 5-5 and Fig. 5-6, respectively. Dash lines in both figures, $L = B$, and $\Delta = 0$ correspond

130

Figure 5-4: Typical plot of terminal velocity of the drop as a function of drop size for $\chi = \lambda = 0.1$, $Re = 10$, and $Bo = 1$.

to spherical drop shapes. Additionally, the film thickness as a function of drop size is shown in Fig. 5-7. For small drops, the drop length and width increase almost linearly with drop size and the drop stays nearly spherical for $\kappa < 0.9$. As drop size becomes comparable to the tube size, the width of the drop approaches an upper bound and does not change much for any further increase in the drop size as seen in Fig. 5-5. Correspondingly, the film thickness first reduces linearly as the drop size increases and eventually appears to reach a constant value for long drops as seen in Fig. 5-7. The length of the drop, on the other hand, increases much faster with increasing drop size and become more and more prolate when $\kappa \geq 0.9$. These results are consistent with the experimental observations of Li et al. [76] for steady bubbles rising in tubes and channels.

The effect of viscosity ratio of inner to outer fluid on drops rising in a tube is investigated by changing λ from 0.1 to 1 while keeping $\chi = 0.1$, $Re = 10$, and $Bo = 1$. A comparison of terminal velocity of the drop as a function of drop size for
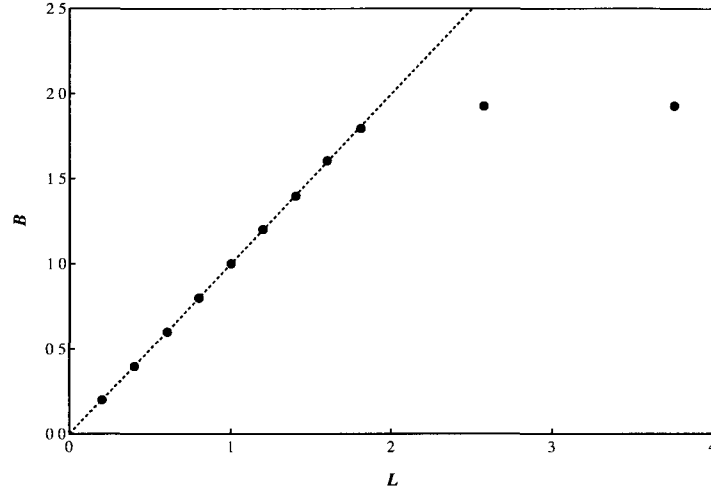
Figure 5-5: Typical plot of the width versus the length of the rising drop at steady state for $\chi = \lambda = 0.1$, $Re = 10$, and $Bo = 1$. The dashed line represents $L = B$ curve.
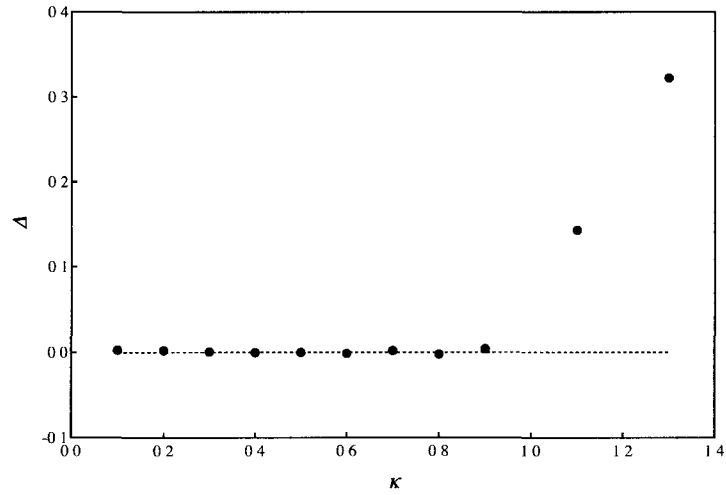
Figure 5-6: Typical plot of the deformation parameter of the rising drop at steady state as a function of drop size for $\chi = \lambda = 0.1$, $Re = 10$, and $Bo = 1$. The dashed line represents $L = B$ curve.
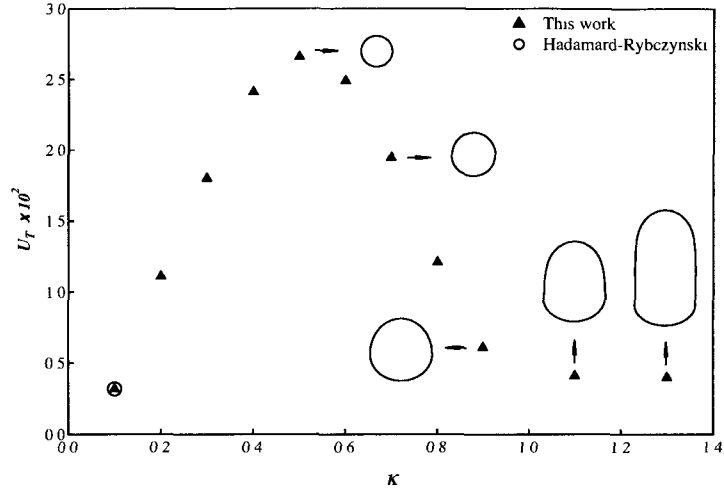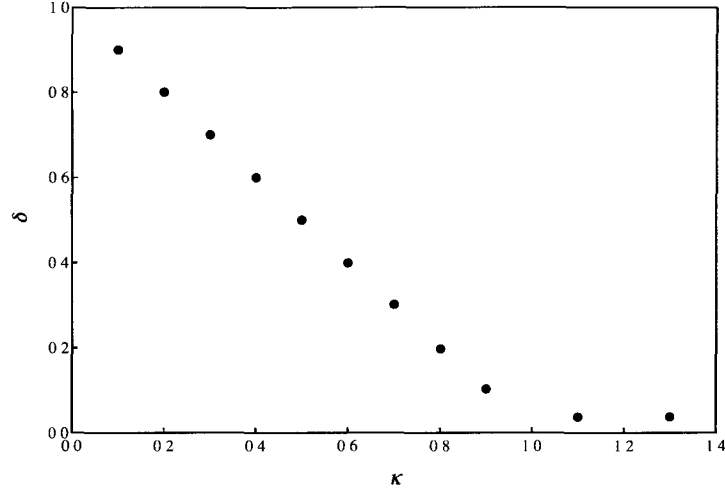
Figure 5-7: Typical plot of film thickness of the drop as a function of drop size for $\chi = \lambda = 0.1$, $Re = 10$, and $Bo = 1$.

$\lambda = 0.1$ and $\lambda = 1$ is presented in Fig. 5-8. As the viscosity ratio increases, that is the drop viscosity increases, the terminal velocity for each size of drops decreases since the increasing resistance of drop to the ambient fluid reduces the interfacial velocity of the drop. At smaller drop sizes, the retardation effect is more pronounced and for long bubbles the terminal velocities are nearly independent of λ. It should be noted that the results presented in Fig. 5-8 show the dimensionless terminal velocity, non-dimensionalized with the buoyancy velocity which is inversely related to the viscosity of the bulk phase. The dimensional velocities for drops rising in a low viscosity bulk phase will be much higher than the dimensional velocities for drops rising in a higher viscosity fluid. A comparison of the deformation parameter for rising drops as a function of drop size for $\lambda = 0.1$ and $\lambda = 1$ shows that the drop shape is insensitive to λ as seen in Fig. 5-9. The only difference between the two case is drops change from spherical to oblate to prolate for $\lambda = 1$ whereas drops change from spherical to prolate for $\lambda = 0.1$. without first becoming oblate. The film thickness is also found to be insensitive to the variation of viscosity ratio for the range of drop sizes studied

Figure 5-8: Comparison of terminal velocity of the drop as a function of drop size between viscosity ratio $\lambda = 0.1$ and 1 for $\chi = 0.1$, $Re = 10$, and $Bo = 1$.

as seen in Fig.5-10. These results are consistent with the experimental observations of Borhan and Pallinti [16].

Bond number $Bo = (\rho_2 - \rho_1)gR_t^2/\sigma_c$ gives the relative significance of gravitational forces to interfacial forces. The effect of Bond number on the steady drop velocity as a function of drop size for $\chi = \lambda = 0.1$ and $Re = 10$ is seen in Fig. 5-11. The results for $Bo = 1$ are identical to those presented in Fig. 5-4. For the simulations of drop with $Bo = 10$, the terminal velocities of drops with drop size $\kappa \leq 0.6$ show a maxima in the terminal velocity at $\kappa = 0.5$ similar to the $Bo = 1$ curve but with smaller terminal velocities. For drop sizes $\kappa > 0.6$, the terminal velocities start to increase again reaching a plateau value much higher than $Bo = 1$ drops. The steady drop shapes for $\kappa = 0.3$, 0.5, 0.7 and 0.9 at $Bo = 1$ and $Bo = 10$ are shown in Fig. 5-12. The comparisons of the deformation parameter and the film thickness of the rising drops for $Bo = 1$ and $Bo = 10$ are shown in Figs. 5-13 and 5-14, respectively. For small drop sizes, $\kappa \leq 0.6$, with negligible wall effect at $Bo = 10$, the drop shapes are

Figure 5-9: Comparison of the deformation parameter of the rising drop at steady state as a function of drop size between viscosity ratio $\lambda = 0.1$ and 1 for $\chi = 0.1$, $Re = 10$, and $Bo = 1$. The dashed line represents $L = B$ curve.
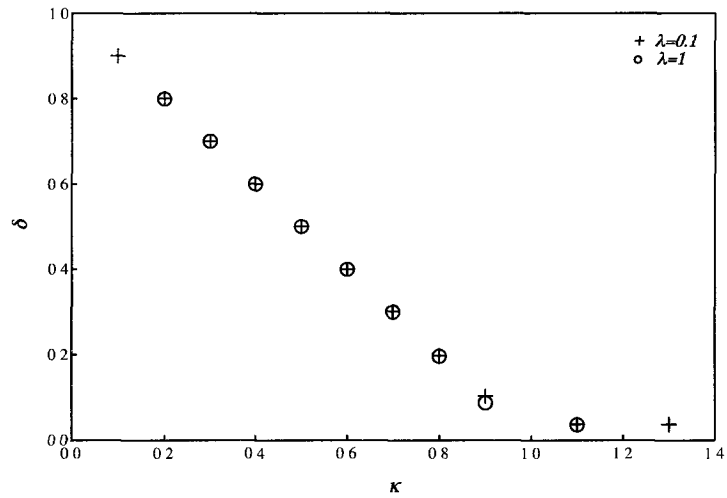
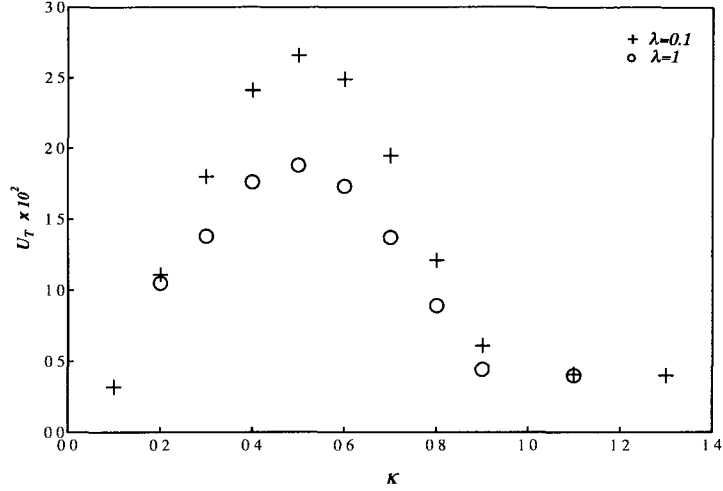Figure 5-10: Comparison of film thickness of the drop as a function of drop size between viscosity ratio $\lambda = 0.1$ and 1 for $\chi = 0.1$, $Re = 10$, and $Bo = 1$.
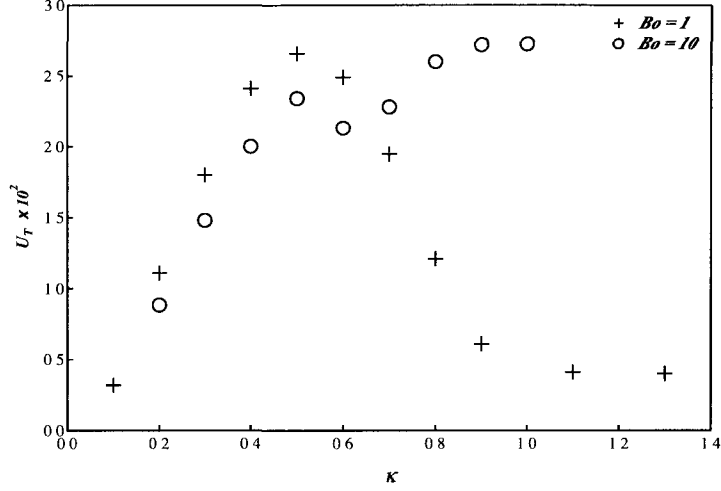
Figure 5-11: Comparison of terminal velocity of the drop as a function of drop size between $Bo = 0.1$ and 1 for $\chi = \lambda = 0.1$ and $Re = 10$.

nearly spherical but lose fore and aft symmetry as seen in Fig. 5-12. For larger drops with $\kappa > 0.6$, the drops are more prolate for larger Bond numbers. A larger Bond number indicates lower interfacial tension since the density ratio is held constant at $\chi = 0.1$ giving the same buoyancy force. The shear stress applied by outer liquid around the drop tends to deform the drop while the interfacial forces oppose this deformation. Hence, drops with a larger Bond number are more deformed in the direction of flow resulting in a larger film thicknesses as seen in Fig. 5-14. The more prolate shape of the drops at higher Bond numbers results in larger terminal velocities.

The inertial effect is captured by the Weber number, We_T, which is defined as $We_T = \rho U_T^2 R_t / \sigma_c$ and is a measure of the inertial force as compared to the interfacial force. The steady shapes of drops for both small drop size ($\kappa = 0.5$) and large drop size ($\kappa = 1$) for various Weber numbers is shown in Fig. 5-15 for $\chi = \lambda = 0.1$. The Weber number is varied by changing the Reynolds and Bond numbers simultaneously

136

Bo = 1

κ = 0.3   κ = 0.5   κ = 0.7   κ = 0.9

Bo = 10

κ = 0.3   κ = 0.5   κ = 0.7   κ = 0.9
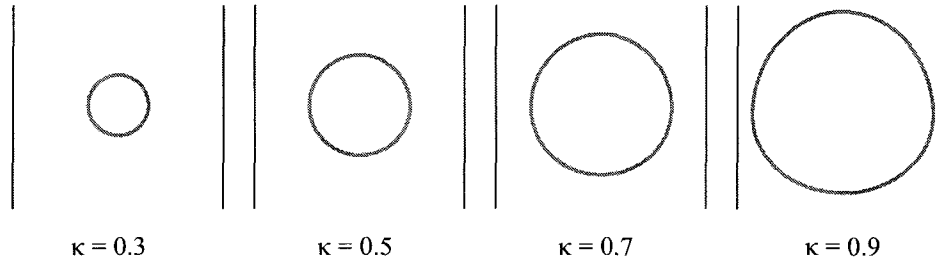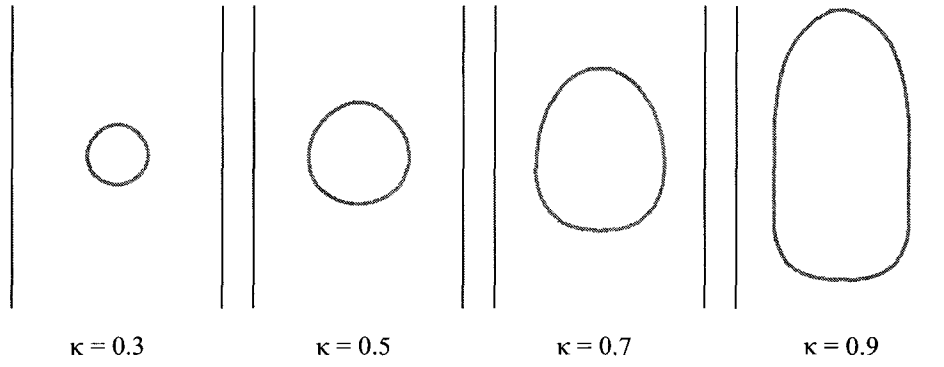
Figure 5-12: The steady drop shapes for κ = 0.3, 0.5, 0.7 and 0.9 at Bo = 1 and Bo = 1 when $\chi = \lambda = 0.1$ and Re = 10.
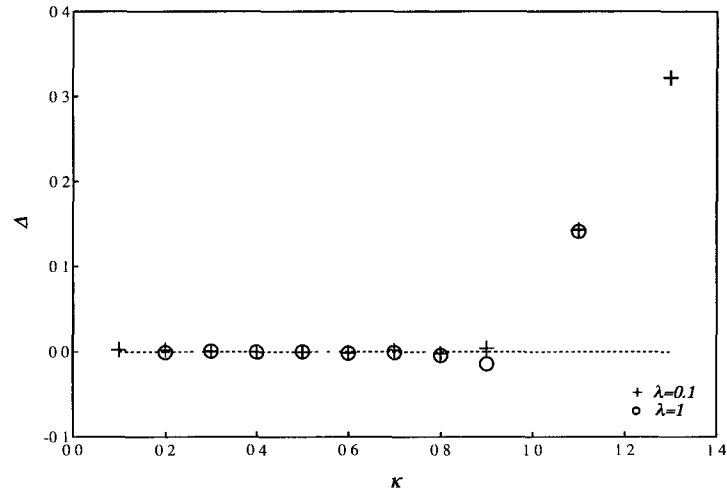
Figure 5-13: Comparison of the deformation parameter of the rising drop at steady state as a function of drop size between $Bo = 0.1$ and 1 for $\chi = \lambda = 0.1$ and $Re = 10$. The dashed line represents $L = B$ curve.
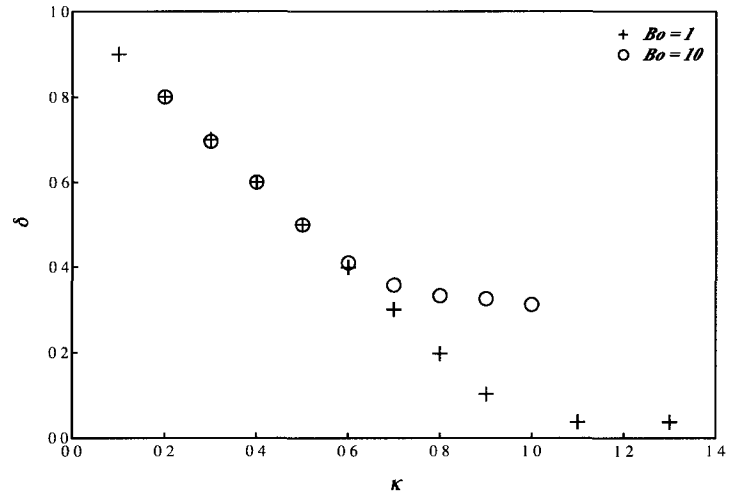
Figure 5-14: Comparison of film thickness of the drop as a function of drop size between $Bo = 0.1$ and 1 for $\chi = \lambda = 0.1$ and $Re = 10$.
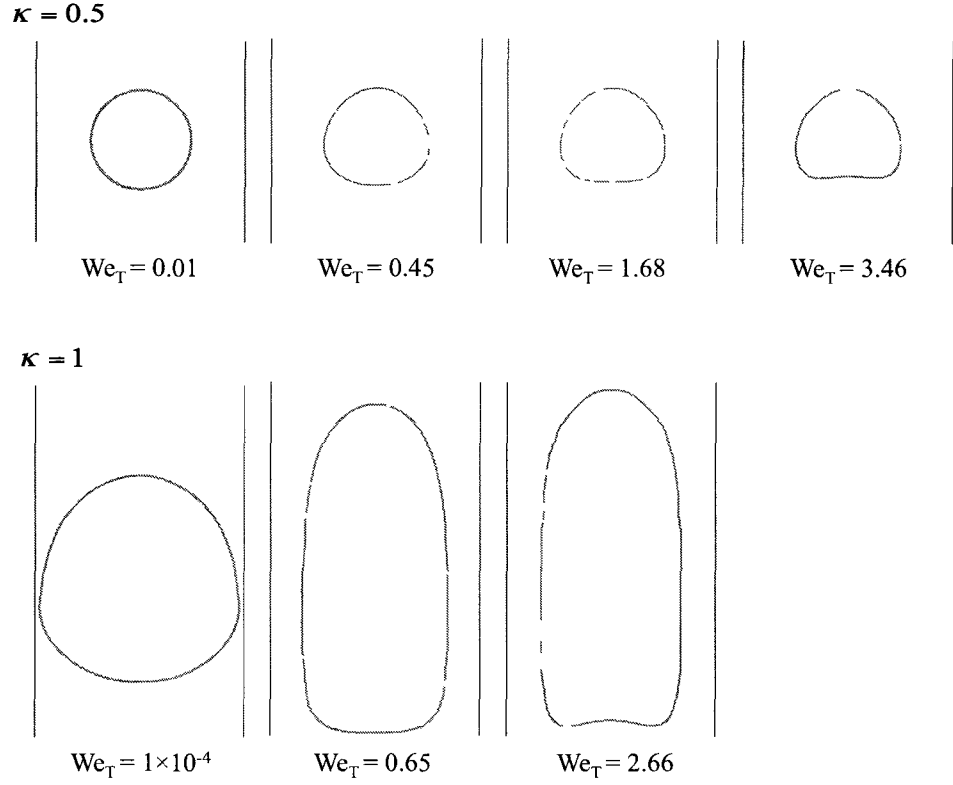
Figure 5-15: The steady drop shapes for both small drop size ($\kappa = 0.5$) and large drop size ($\kappa = 1$) for various Weber number when $\chi = \lambda = 0.1$, and $Re/Bo = 10$.

while keeping the ratio of $Re/Bo = 10$. As the Weber number is increased, drop deforms, becomes flat and eventually develops a negative curvature at the rear. The flattening and development of negative curvature at the drop rear have been observed for both small and large drops with increasing weber numbers in the experimental work by Li et al. [76].

5.5.3 Surfactant results for Newtonian fluids

The effect of the equilibrium surfactant coverage, x, and surfactant mass transfer on the drop dynamics is discussed in this section for $\chi = \lambda = 0.1$, $Re = 10$, $Bo = 1$, and $E = 0.164$. A comparison of terminal velocity as a function of drop size for $x = 0$ and $x = 0.667$ for drops rising in a tube is shown in Fig. 5-16. As the equilibrium fractional coverage is increased, the terminal velocities for drops of all sizes reduce but follow a similar trend as the surfactant-free cases. With increasing drop size, the terminal velocities of drops with $x = 0.667$ first increase up to a maximum values at $\kappa = 0.5$, and then decrease to a constant plateau values indicating the terminal velocity is independent of drop size for large drops. Previous studies have shown the retardation effect of surfactants on rising drops/bubbles in a confined capillary [1, 15] as well as for rising bubbles in an unbounded domain [44, 96, 151, 152], and a decrease in the terminal velocity of bubbles with increasing bulk concentration of surfactants [44, 96, 151, 152]. The retarded mobility of drops in the presence of surfactants is due to Marangoni stresses generated at the interface which oppose the flow. As shown in Fig. 5-17, the interfacial tension for $x = 0$ is uniform along the length of the drop while for $x = 0.667$, the interfacial tension at the rear of the drop is lower than the front of the drop due to accumulation of soluble surfactants at the rear of the drop. In this comparison, while the equilibrium fractional coverage changes, the equilibrium interfacial tension for the two cases is the same. The interfacial tension gradient due to the non-uniform distribution of soluble surfactants gives rise to Marangoni stresses that opposes the flow and hence retards the drop motion.

The comparisons of deformation parameter of the rising drops at steady state and the film thickness for $x = 0$ and $x = 0.667$ are shown in Figs. 5-18 and 5-19, respectively. Both figures indicate that the drop shapes are not very sensitive to
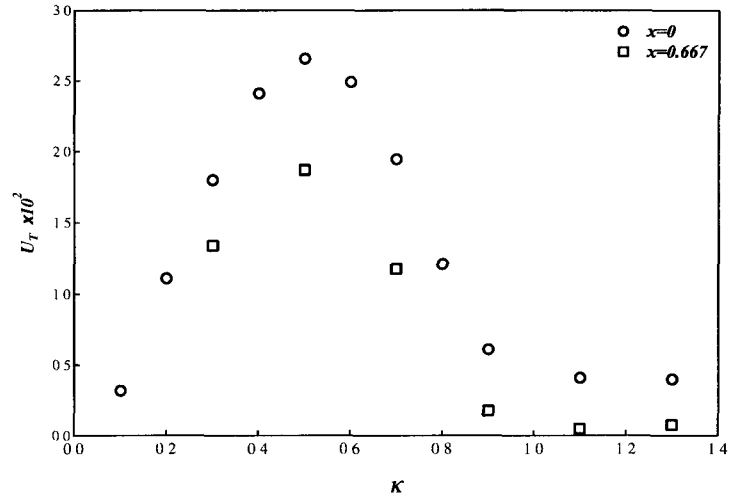
Figure 5-16: Comparison of terminal velocity as a function of drop size among soluble surfactant cases of $x = 0$ and 0.667 for $\chi = \lambda = 0.1$, $Re = 10$, $Bo = 1$, $Bi = 0.1$, and $Pe_s = 10$.
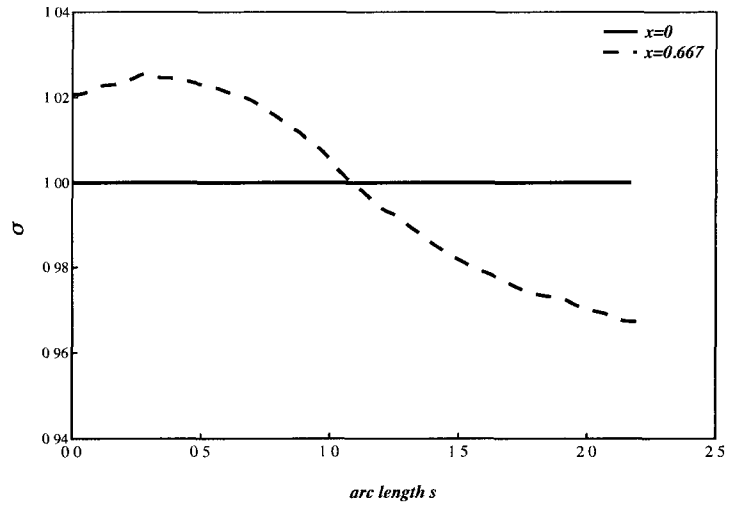
Figure 5-17: Comparison of interfacial tension along the interface at steady state among soluble surfacant cases of $x = 0$ and 0.667, in the adsorption-desorption limit for $\kappa = 0.7$, $\chi = \lambda = 0.1$, $Re = 10$, $Bo = 1$, $Bi = 0.1$, and $Pe_s = 10$.
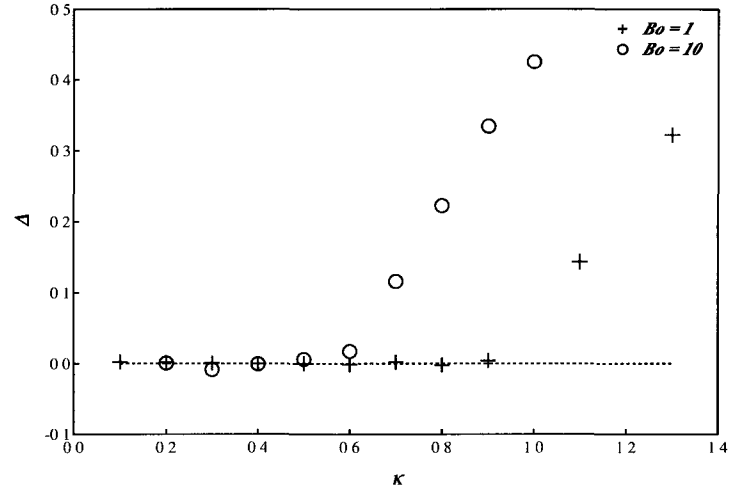
141

Figure 5-18: Comparison of the deformation parameter of the rising drop at steady state as a function of drop size between $x = 0$ and 0.667 for $\chi = \lambda = 0.1$, $Re = 10$, $Bo = 1$, $Bi = 0.1$, and $Pe_s = 10$. The dashed line represents $L = B$ curve.

the presence of surfactants especially for small drops. A comparison of steady drop shapes for $x = 0$ and $x = 0.667$ for $\kappa = 0.5$, 0.7, 0.9, 1.1, and 1.3 is shown in Fig. 5-20. The drop shapes with surfactant coverage of $x = 0.667$ are similar to the surfactant-free drops in that they stay spherical for small drops ($\kappa < 0.7$) but become more prolate for large drops ($\kappa \geq 0.7$). This is seen in Fig. 5-18 as well as in Fig. 5-20 and is consistent with the experimental observations of Almatroushi and Borhan [1]. As a consequence, the film thickness for large drops ($\kappa \geq 0.7$) with soluble surfactants are higher than the corresponding film thickness in the absence of surfactants seen in Fig. 5-19 [98, 102]. For a long drop of size $\kappa = 1.3$, the film thickness in the central region is 0.04 for a surfactant-free system while it is 0.09 for the soluble surfactant system where the surfactant transport is controlled by sorption kinetics. The apparent film-thickening phenomenon is expected for long bubbles in the presence of soluble surfactants in the adsorption-desorption limit [116].

Surfactant mass transfer plays an important role in drop dynamics [96, 116].

142
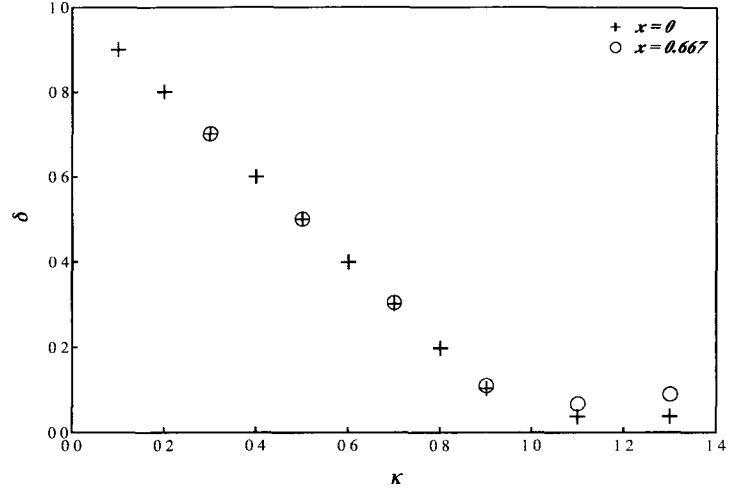
Figure 5-19: Comparison of film thickness of the drop as a function of drop size between $x = 0$ and 0.667 for $\chi = \lambda = 0.1$, $Re = 10$, $Bo = 1$, $Bi = 0.1$, and $Pe_s = 10$.

When the mass transport of surfactants to the interface is much faster than interfacial convection, the surfactant concentration at the interface remains almost at the equilibrium concentration and results in a uniform reduction in interfacial tension. It is actually the 'clean' case with lower interfacial tension. This scenario is designated as Case I for $\sigma = 1$. It corresponds to the surfactant case with $Bi \to \infty$. When surfactant mass transfer to the interface is much slower than surface convection, surfactants cannot adsorb/desorb from the interface and behave as insoluble surfactants. This scenario is designated as Case II for which $Bi = 0$. Finally, Case III refers to soluble surfactants in the adsorption-desorption limit when the rate of the surfactant mass transport to the interface is comparable to the interfacial convection rate and the adsorption/desorption rate of surfactants is much slower than the bulk diffusion rate. In this case, the Biot number Bi is set to 0.1. A comparison of terminal velocity as a function of drop size for these three cases for $\chi = \lambda = 0.1$, $Re = 10$, $Bo = 1$, $x = 0.667$, and $Pe_s = 10$ is shown in Fig. 5-21. For Case I, the plot of terminal velocity as a function of drop size is similar to Fig. 5-4. In the presence of insoluble
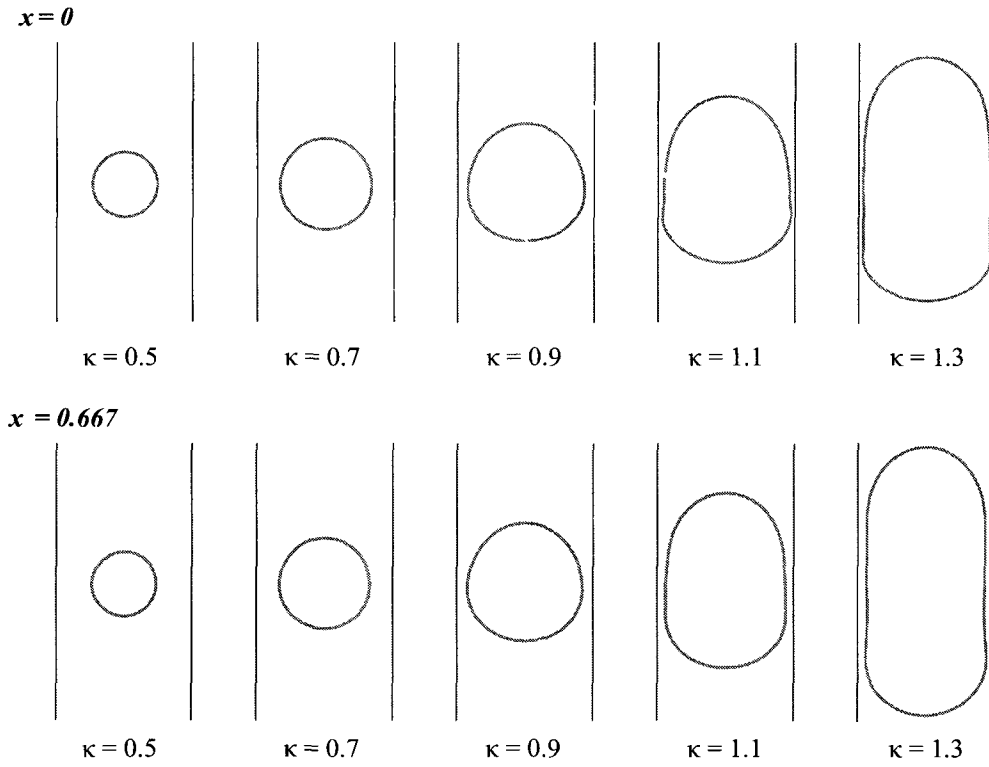
Figure 5-20: The steady drop shapes for $\kappa = 0.5$, 0.7, 0.9, 1.1 and 1.3 at $x = 0$ and $x = 0.667$ for $\chi = \lambda = 0.1$, $Re = 10$, $Bo = 1$, $Bi = 0.1$, and $Pe_s = 10$.
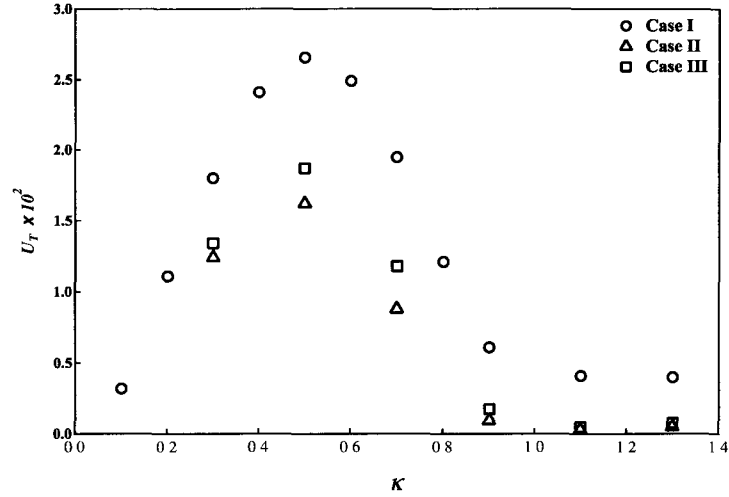
Figure 5-21: Comparison of terminal velocity as a function of drop size among cases of 'clean' (Case I), insoluble surfactants (Case II), and soluble surfactants (Case III) in the adsorption-desorption limit for $\chi = \lambda = 0.1$, $Re = 10$, $Bo = 1$, $x = 0.667$, and $Pe_s = 10$.

surfactants, the mobility of drops of all sizes is retarded compared to Case I. In the presence of soluble surfactants, the drops of all sizes become remobilized compared to the insoluble surfactant case. The comparisons of deformation parameters of the rising drops at steady state and the film thickness between insoluble surfactant case (Case II) and soluble surfactant case (Case III) are shown in Fig. 5-22 and Fig. 5-23, respectively. Both figures indicate that the drop shapes are insensitive to the surfactant mass transfer effect except at very large drop sizes.

The effect of surfactant mass transfer can be better understood by comparing the interfacial tension as a function of the arc length for the three cases for a drop size $\kappa = 0.7$ as seen in Fig. 5-24. The interfacial tension in Case I is uniform along the length of the drop. In Case II, the surfactants are insoluble and not allowed to transport between the interface and the bulk. The interfacial tension at the rear of the drop is much lower than the front of the drop indicating the accumulation of

145
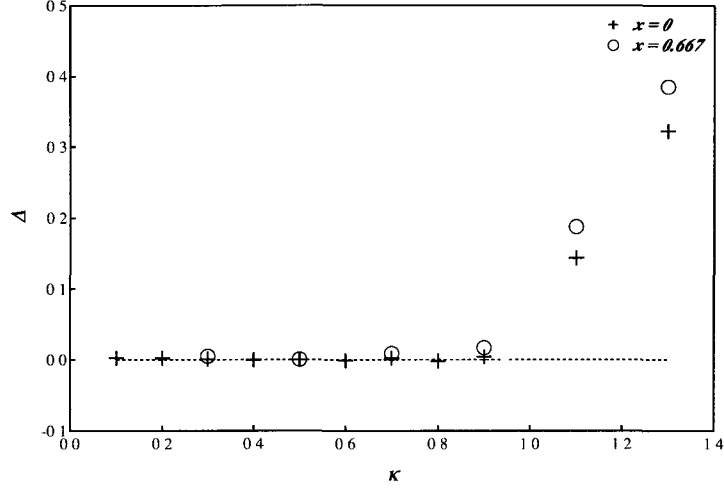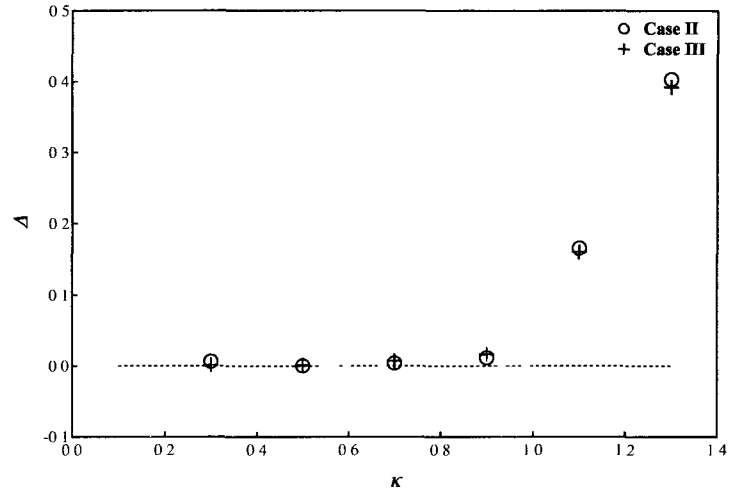
Figure 5-22: Comparison of the deformation parameter of the rising drop at steady state as a function of drop size between insoluble surfactant case (Case II) and soluble surfactant case (Case III) for $\chi = \lambda = 0.1$, $Re = 10$, $Bo = 1$, $x = 0.667$, and $Pe_s = 10$. The dashed line represents $L = B$ curve.
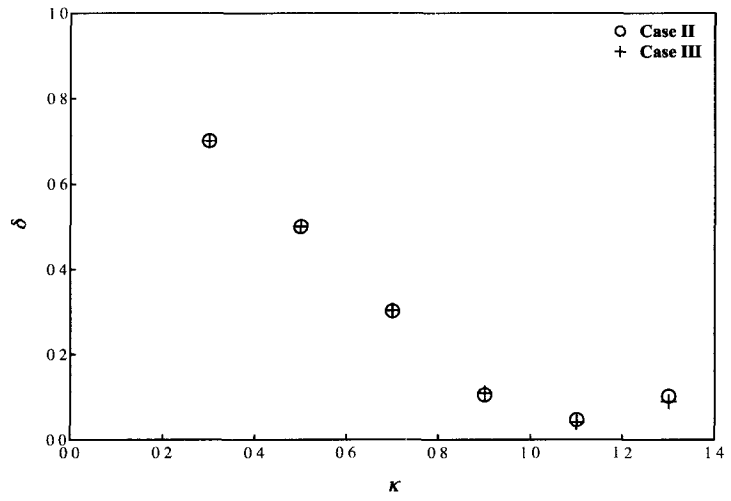
Figure 5-23: Comparison of film thickness of the drop as a function of drop size between insoluble surfactant case (Case II) and soluble surfactant case (Case III) for $\chi = \lambda = 0.1$, $Re = 10$, $Bo = 1$, $x = 0.667$, and $Pe_s = 10$.

0.96 0.98 0.99 1.01 1.03

Case I   **Case II**   **Case III**
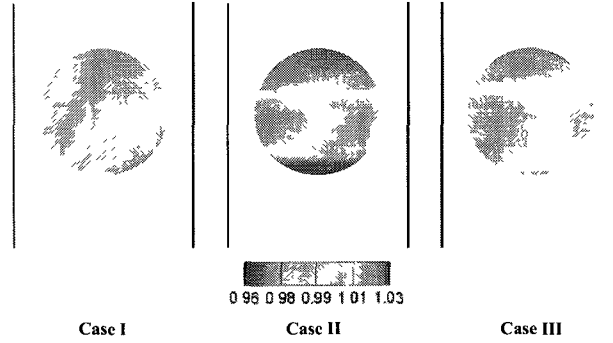
Figure 5-24: Comparison of interfacial tension along the interface at steady state among cases of 'clean', insoluble surfactants, and soluble surfactants in the adsorption-desorption limit for $\kappa = 0.7$, $\chi = \lambda = 0.1$, $Re = 10$, $Bo = 1$, $x = 0.667$, and $Pe_s = 10$.

surfactants at the rear of the drop due to the interfacial flow moving towards the end of the drop. The large variation of interfacial tension along the interface gives rise to Marangoni stresses that oppose the flow and hence retard the drop motion. That is why the terminal velocities for drops of all sizes are reduced in Fig. 5-21. If mass transfer is allowed to take place as in Case III, surfactants will desorb from the rear of the drop where surfactant concentration is higher while surfactants will adsorb at the front of the drop. Thus the interfacial tension gradient between the front and the rear of the drop will reduce as is shown in Fig. 5-24, and so will the Marangoni stresses. The reduced Marangoni stresses in the case of soluble surfactants result in an increased drop mobility as shown in Fig. 5-21. The remobilization due to the reduced Marangoni stresses has also been observed when the exchange of surfactants between the interface and the bulk increases [126, 136].

5.5.4 Results for Shear-thinning Fluids

In the last section, the effects of the fluid rheology on the mobility and deformation of drops rising in a tube in the presence of soluble surfactants in the adsorption-desorption limit are investigated. For the results presented in this section, $\chi = \lambda = 0.1$, $Re = 10$, and $Bo = 1$, and for surfactant systems, $E = 0.164$, $Pe_s = 10$, $x = 0.667$, and $Bi = 0.1$. In order to study the effect of the drop rheology, both Newtonian ($n_1 = 1$) and strongly shear-thinning ($n_1 = 0.3$, $\beta_1 = 0.002$, and $\alpha_1 = 10$) drops rising in a Newtonian quiescent bulk fluid are considered. The comparisons of the terminal velocity, the deformation parameter, and the film thickness of steady rising drops as a function of drop size between Newtonian drop case and strongly shear-thinning drop case are shown in Fig. 5-25, Fig. 5-26, and Fig. 5-27, respectively. There are no significant differences for the terminal velocities, the deformation parameters, and the film thickness of the rising drop at steady state between Newtonian drop case and strongly shear-thinning drop case with surfactant coverage of 0.667. Since $\lambda = 0.1$, the zero-shear viscosity of the drop phase is only one-tenth of the bulk phase viscosity. Even for a strongly shear-thinning drop phase, the drop viscosity does not reduce significantly to cause a change in the drop deformation and mobility.

To study the effect of bulk rheology, Newtonian drops rising in both Newtonian ($n_2 = 1$) and strongly shear-thinning ($n_2 = 0.3$, $\beta_2 = 0.002$, and $\alpha_2 = 10$) quiescent bulk fluids are considered. The comparisons of the terminal velocity, the deformation parameter, and the film thickness of steady rising drops as a function of drop size between Newtonian bulk case and strongly shear-thinning bulk case are shown in Fig. 5-28, Fig. 5-29, and Fig. 5-30, respectively. As the bulk phase becomes strongly shear-thinning, drop mobility increases compared to the Newtonian bulk case as seen in Fig. 5-28. The larger shear rate near the rising drop results in a lower viscosity of
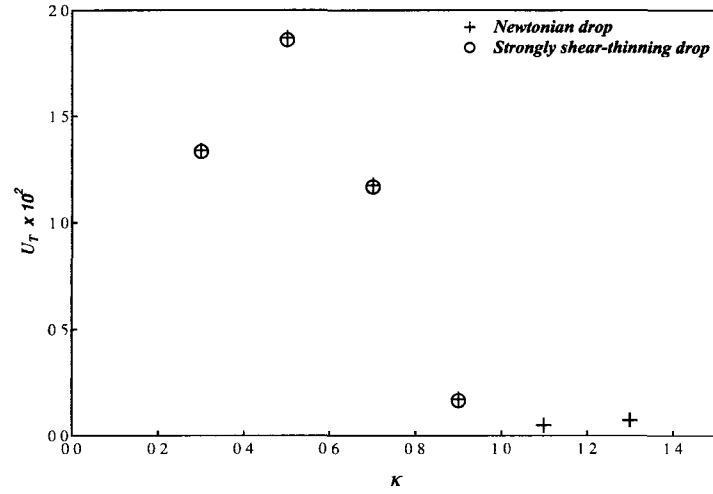
Figure 5-25: Comparison of terminal velocity as a function of drop size between Newtonian drop case ($n_1 = 1$) and strongly shear-thinning drop case ($n_1 = 0.3$, $\beta_1 = 0.002$, and $\alpha_1 = 10$) in the presence of soluble surfactants in the adsorption-desorption limit for $\chi = \lambda = 0.1$, $Re = 10$, $Bo = 1$, $Pe_s = 10$, $x = 0.667$, and $Bi = 0.1$.
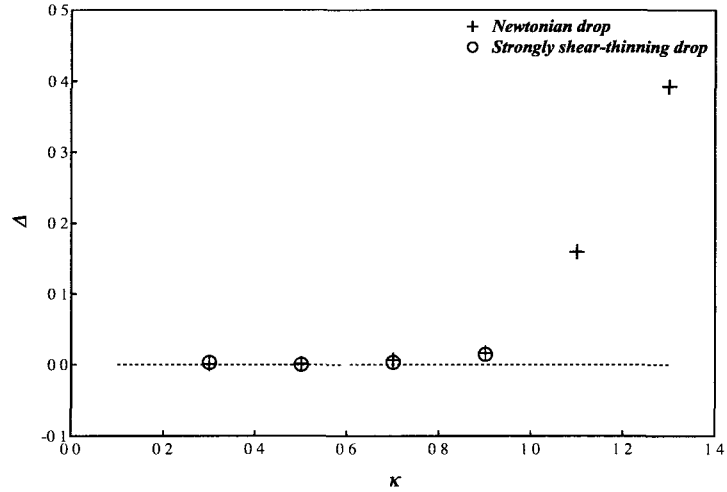
Figure 5-26: Comparison of the deformation parameter of the rising drop at steady state as a function of drop size between Newtonian drop case ($n_1 = 1$) and strongly shear-thinning drop case ($n_1 = 0.3$, $\beta_1 = 0.002$, and $\alpha_1 = 10$) in the presence of soluble surfactants in the adsorption-desorption limit for $\chi = \lambda = 0.1$, $Re = 10$, $Bo = 1$, $Pe_s = 10$, $x = 0.667$, and $Bi = 0.1$. The dashed line represents $L = B$ curve.

149
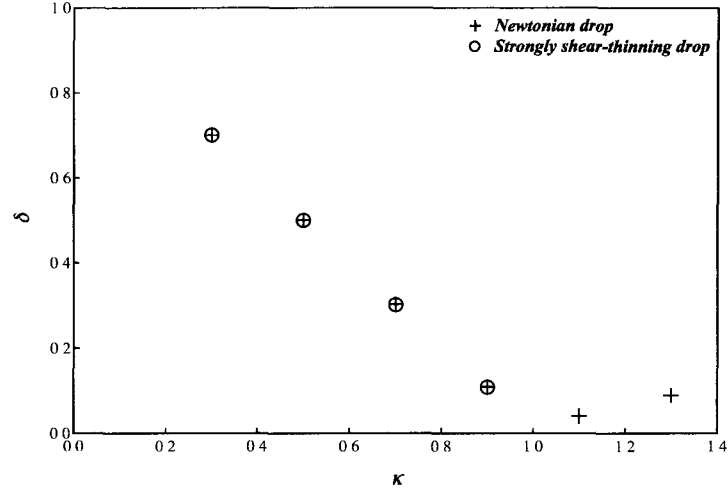
Figure 5-27: Comparison of film thickness of the drop as a function of drop size between Newtonian drop case ($n_1 = 1$) and strongly shear-thinning drop case ($n_1 = 0.3$, $\beta_1 = 0.002$, and $\alpha_1 = 10$) in the presence of soluble surfactants in the adsorption-desorption limit for $\chi = \lambda = 0.1$, $Re = 10$, $Bo = 1$, $Pe_s = 10$, $x = 0.667$, and $Bi = 0.1$.

the strongly shear-thinning bulk phase. The resistance from the bulk for the rising drop is reduced and the drop mobility increases when the drop rises in a strongly shear-thinning bulk phase. Both Fig. 5-29 and Fig. 5-30 indicate that the bulk rheology has a minimal impact on the drop shape.
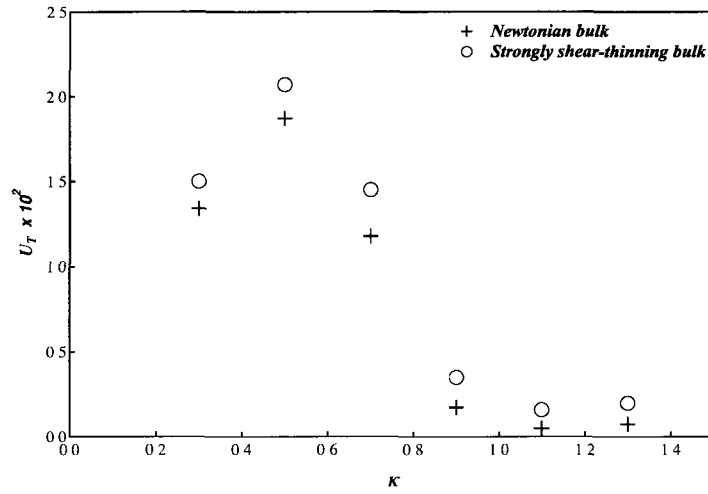
Figure 5-28: Comparison of terminal velocity as a function of drop size between Newtonian bulk case ($n_2 = 1$) and strongly shear-thinning bulk case ($n_2 = 0.3$, $\beta_2 = 0.002$, and $\alpha_2 = 10$) in the presence of soluble surfactants in the adsorption-desorption limit for $\chi = \lambda = 0.1$, $Re = 10$, $Bo = 1$, $Pe_s = 10$, $x = 0.667$, and $Bi = 0.1$.
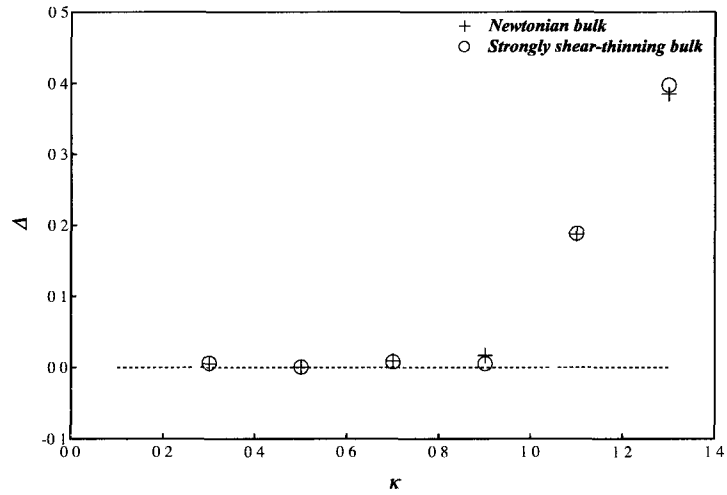
Figure 5-29: Comparison of the deformation parameter of the rising drop at steady state as a function of drop size between Newtonian bulk case ($n_2 = 1$) and strongly shear-thinning bulk case ($n_2 = 0.3$, $\beta_2 = 0.002$, and $\alpha_2 = 10$) in the presence of soluble surfactants in the adsorption-desorption limit for $\chi = \lambda = 0.1$, $Re = 10$, $Bo = 1$, $Pe_s = 10$, $x = 0.667$, and $Bi = 0.1$. The dashed line represents $L = B$ curve.

151
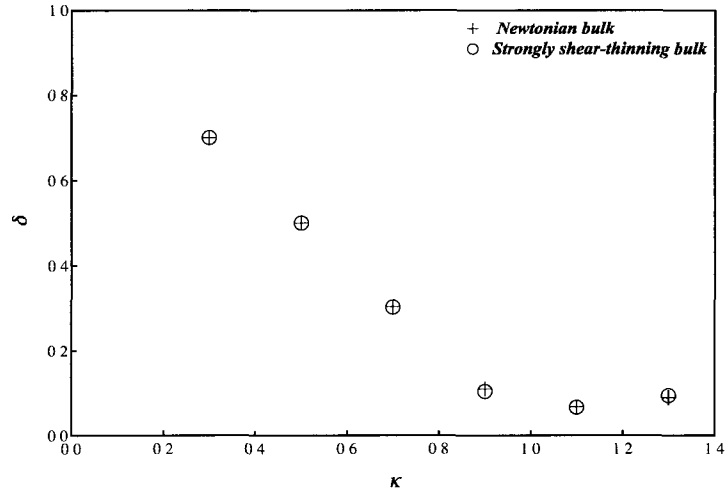
Figure 5-30: Comparison of film thickness of the drop as a function of drop size between Newtonian bulk case ($n_2 = 1$) and strongly shear-thinning bulk case ($n_2 = 0.3$, $\beta_2 = 0.002$, and $\alpha_2 = 10$) in the presence of soluble surfactants in the adsorption-desorption limit for $\chi = \lambda = 0.1$, $Re = 10$, $Bo = 1$, $Pe_s = 10$, $x = 0.667$, and $Bi = 0.1$.

Chapter 6

Summary and Future Work

A robust hybrid Volume-of-Fluid (VOF) numerical model was developed, which combined the mass conservation properties of the VOF method with the accuracy of the front-tracking scheme to study strongly deforming interface. The numerical method was used to study the drop formation process in co-flowing fluids and the motion of drops rising in a confined tube with inertia, surfactants, and shear-thinning fluid rheology effects. In the numerical simulations, the motion of the incompressible drop and bulk fluids were described by the continuity and momentum equations. The surfactant-free numerical models were validated by comparing with previously published experimental data. Surfactants were modeled using a Langmuir adsorption framework and considered soluble with adsorption-desorption as the rate-limiting step. The non-Newtonian shear-thinning behavior was described by the Carreau model.

For drop formation process, the effects of the ratio of outer flow rate to inner flow rate, ratio of drop viscosity to bulk viscosity, Bond number, and capillary number on the drop size was investigated for Newtonian systems. The simulation results indicated that the drop size decreased by decreasing the viscosity ratio, decreasing the capillary number, increasing the flow rate ratio, or increasing the Bond number. Jetting mode was observed at higher flow rate ratios, viscosity ratios, and capillary

numbers. At higher Bond numbers, $Bo \geq 3$, a negative curvature was observed at the rear of the drop resulting in a mushroom shape. When surfactants were present in the system, they were swept from the apex of the drop and accumulated in the neck region slowing down the break up of the primary neck. This resulted in larger primary drop volumes and longer break up times. The outer co-flowing flow washed the surfactants away from the neck region and weakened the effect of Marangoni stresses. At high equilibrium interfacial coverages, larger Marangoni stresses resulted in substantial retardation of the primary neck formation and the drops broke at the secondary neck. By increasing the outer co-flowing flow, surfactant gradients were reduced weakening the Marangoni stresses. Drop breakup was then reverted back to the primary neck. The adsorption-desorption rate characterized by the Biot number also affected the neck breakup location. The primary drop volume and breakup time showed non-linear behavior with Biot number in the absence and presence of an outer co-flowing flow. As the confining walls moved closer, the formation of the neck could be completely suppressed. The geometry and flow rate of the outer fluid in a co-flowing system thus provided further control in dispensing fluids of desired drop sizes in the presence of surfactants. Shear-thinning rheology of the drop fluid also affected the drop formation process. As the drop became more shear-thinning, the drop broke up faster with a shorter remnant drop length. Retardation of drop breakup in the presence of soluble surfactants were seen for shear-thinning drops as well. In the presence of soluble surfactant with high equilibrium interfacial coverage, shear-thinning drop rheology caused the drop break up at the secondary neck with multiple satellite drop formation.

The hybrid VOF numerical method was also implemented on the buoyancy-driven rise of drops in a tube filled with a quiescent immiscible fluid in the presence of surfactants at finite Reynolds numbers. The steady drop shape and size, drop terminal

154

velocity, film thickness, and deformation parameter were analyzed from the simulation results. For the surfactant-free Newtonian system, the effect of the tube confinement, viscosity ratio of drop to bulk fluids, Bond number, and Weber number on the steady drop motion and shape were investigated for drops of different sizes. It was shown that for small drop sizes, the terminal velocity of the drops increased with the drop size. As the drop size became comparable to the tube size, the increased wall drag reduced the velocity of the drops. Beyond a critical drop size, the drop terminal velocity was independent of the drop size. As the viscosity of drop phase was increased, the terminal velocity for drops of all sizes were reduced due to the increasing resistance to the outer fluid. As the Bond number was increased, small drops ($\kappa \leq 0.6$) lost fore and aft symmetry and their mobility was retarded due to shear stresses applied by the outer fluid. Large drops ($\kappa > 0.6$), on the other hand, were more elongated in the axial direction due to the confining wall and their mobility increased. The increasing inertial effect indicated by the Weber number could increase the terminal velocity of drops and resulted in deformation such as flattening and negative curvatures at the rear of the drop. For the surfactant systems, the effect of the equilibrium coverage of soluble surfactants in the adsorption-desorption limit and surfactant mass transfer on the drop mobility were also determined. The simulation results showed that non-uniform distribution of surfactants along the interface gave rise to Marangoni stresses that opposed the interfacial flow and retarded the drop motion. Larger Marangoni stresses generated in the presence of insoluble surfactants compared to soluble surfactants, or with higher equilibrium coverage of soluble surfactants led to larger retardation effects on buoyancy-driven motion of drops. For the range of parameters studied, the shear-thinning drop rheology had a negligible effect on the deformation and mobility of the drop. For a strongly shear-thinning bulk fluid, the drop mobility increased though the drop deformation showed

no significant change compared to a Newtonian bulk phase.

Two-phase flow problems are of great interest in a variety of applications such as microencapsulation, enhanced oil recovery, and microfluidics. The results of this work are a first attempt at implementing the developed numerical model to study drop formation in co-flowing fluids and the drop motion in a confined domain with the effects of surfactants and non-Newtonian rheology at finite Reynolds numbers. In the future, the numerical model presented in this work can be extended to

- include more complex non-Newtonian rheologies such as viscoelastic rheology,

- consider effect of soluble surfactants where the adsorption-desorption rate is comparable to the diffusion rate,

- incorporate the effects of the geometry of the confining wall into rectangular channels or more complex geometries.

Bibliography

[1] E. Almatroushi and A. Borhan   Surfactant Effect on the Buoyancy-Driven Motion of Bubbles and Drops in a Tube. *Annals of the New York Academy of Sciences*, 1027(1).330–341, 2004.

[2] S.L. Anna, N. Bontoux, and H.A. Stone. Formation of dispersions using flow focusing in microchannels. *Applied Physics Letters*, 82:364, 2003.

[3] S.L. Anna and H.C. Mayer. Microscale tipstreaming in a microfluidic flow focusing device. *Physics of Fluids*, 18:121512, 2006.

[4] N. Ashgriz and J.Y. Poo. Flair: Flux line-segment model for advection and interface reconstruction. *Journal of Computational Physics*, 93(2):449–468, 1991.

[5] G. Astarita and G. Apuzzo. Motion of gas bubbles in non-newtonian liquids. *AIChE Journal*, 11(5):815–820, 1965

[6] M.E. Avery and J. Mead. Surface properties in relation to atelectasis and hyaline membrane disease. *Archives of Pediatrics and Adolescent Medicine*, 97:517–523, 1959.

[7] P.S. Ayyaswamy, J. Zhang, and D.M. Eckmann. Numerical modeling of the transport to an intravascular bubble in a tube with a soluble/insoluble surfactant. *Annals of the New York Academy of Sciences*, 1077(1):270–287, 2006.

[8] A. Barrero and I.G. Loscertales. Micro-and nanoparticles via capillary flows. *Annual Review of Fluid Mechanics*, 39:89–106, 2007.

[9] O.A. Basaran. Small-scale free surface flows with breakup: Drop formation and emerging applications. *AIChE Journal*, 48(9):1842, 2002.

[10] M. Bavière. *Basic concepts in enhanced oil recovery processes*. Chapman & Hall, 1991.

[11] P. Becher. *Emulsions: theory and practice*. Reinhold Pub. Corp., 1965.

[12] A. Belmonte. Self-oscillations of a cusped bubble rising through a micellar solution. *Rheologica Acta*, 39(6):554–559, 2000.

[13] R.B. Bird, R.C. Armstrong, and O. Hassager. Dynamics of polymeric liquids. volume 1: Fluid mechanics. *A Wiley-Interscience Publication, John Wiley & Sons*, 1987.

[14] R.B. Bird, W.E. Stewart, E.N. Lightfoot, et al. *Transport phenomena*. Wiley New York, 2007.

[15] A. Borhan and C.F. Mao. Effect of surfactants on the motion of drops through circular tubes. *Physics of Fluids A: Fluid Dynamics*, 4:2628–2640, 1992.

[16] A. Borhan and J. Pallinti. Buoyancy-driven motion of viscous drops through cylindrical capillaries at small Reynolds numbers. *Industrial & Engineering Chemistry Research*, 34(8):2750–2761, 1995.

[17] A. Borhan and J. Pallinti. Breakup of drops and bubbles translating through cylindrical capillaries. *Physics of Fluids*, 11:2846–2855, 1999.

[18] L.A. Bozzi, J.Q. Feng, T.C. Scott, and A.J. Pearlstein. Steady axisymmetric motion of deformable drops falling or rising through a homoviscous fluid in a tube at intermediate Reynolds number. *Journal of Fluid Mechanics*, 336:1–32, 1997.

[19] J.U. Brackbill, D.B. Kothe, and C. Zemach. A continuum method for modeling surface tension. *Journal of Computational Physics*, 100(2):335, 1992.

[20] F.P. Bretherton. The motion of long bubbles in tubes. *Journal of Fluid Mechanics*, 10(02):166–188, 1961.

[21] P.J. Carreau, D.D. Kee, and M. Daroux. An analysis of the viscous behaviour of polymeric solutions. *The Canadian Journal of Chemical Engineering*, 57(2):135–140, 1979.

[22] E. Castro-Hernández, V. Gundabala, A. Fernández-Nieves, and J.M. Gordillo. Scaling the drop size in coflow experiments. *New Journal of Physics*, 11:075021, 2009.

[23] C.H. Chang and E.I. Franses. Adsorption dynamics of surfactants at the air/water interface: a critical review of mathematical models, data, and mechanisms. *Colloids and Surfaces A: Physicochemical and Engineering Aspects*, 100:1–45, 1995.

[24] J. Chen and K.J. Stebe. Marangoni retardation of the terminal velocity of a settling droplet: The role of surfactant physico-chemistry. *Journal of Colloid and Interface Science*, 178:144–155, 1996.

[25] J. Chen and K.J. Stebe. Surfactant-induced retardation of the thermocapillary migration of a droplet. *Journal of Fluid Mechanics*, 340:35–59, 1997.

[26] R.P. Chhabra. *Bubbles, drops, and particles in non-Newtonian fluids*. CRC, 2007.

[27] C. Clasen, J. Bico, V.M. Entov, and G.H. McKinley. gobbling drops: the jetting–dripping transition in flows of polymer solutions. *Journal of Fluid Mechanics*, 636(1):5–40, 2009.

[28] R. Clift, J.R. Grace, M.E. Weber, and R. Clift. *Bubbles, drops, and particles*, volume 3. Academic press New York, 1978.

[29] D.J. Coyle, C.W. Macosko, and L.E. Scriven. Film-splitting flows of shear-thinning liquids in forward roll coating. *AIChE Journal*, 33(5):741–746, 1987.

[30] C. Cramer, P. Fischer, and E.J. Windhab. Drop formation in a co-flowing ambient fluid. *Chemical Engineering Science*, 59(15):3045, 2004.

[31] R.V. Craster, O.K. Matar, and D.T. Papageorgiou. Pinchoff and satellite formation in surfactant covered viscous threads. *Physics of Fluids*, 14:1364, 2002.

[32] B. Cuenot, J. Magnaudet, and B. Spennato. The effects of slightly soluble surfactants on the flow around a spherical bubble. *Journal of Fluid Mechanics*, 339:25–53, 1997.

[33] Y. Cui and N.R. Gupta. Drop formation in co-flowing fluid streams. *International Journal of Transport Phenomena*, 12:217–226, 2011.

[34] Y. Cui and N.R. Gupta. Surfactant effects on drop formation in co-flowing fluid streams. *Colloids and Surfaces A*, 393:111–121, 2011.

[35] D.S. Dandy and L.G. Leal. Buoyancy-driven motion of a deformable drop through a quiescent liquid at intermediate Reynolds numbers. *Journal of Fluid Mechanics*, 208:161–192, 1989.

[36] P. Daripa and G. Paşa. The effect of surfactant on the motion of long bubbles in horizontal capillary tubes. *Journal of Statistical Mechanics: Theory and Experiment*, 2010:L02002, 2010.

[37] J.F. Davidson and B.O.G. Schuler. Bubble formation at an orifice in an inviscid liquid. *Chemical Engineering Research and Design*, 38(a):335, 1960.

[38] M.R. Davidson and J.J. Cooper-White. Pendant drop formation of shear-thinning and yield stress fluids. *Applied Mathematical Modelling*, 30(11):1392–1405, 2006.

[39] M.R. Davidson, J.J. Cooper-White, and V. Tirtaatmadja. Shear-thinning drop formation. *ANZIAM Journal*, 45, 2004.

[40] H. Ding and P.D.M. Spelt. Onset of motion of a three-dimensional droplet on a wall in shear flow at moderate reynolds numbers. *Journal of Fluid Mechanics*, 599:341–362, 2008.

[41] C.R. Easton. Homogeneous boundary conditions for pressure in the mac method. *Journal of Computational Physics*, 9(2):375–379, 1972.

[42] J. Eggers and E. Villermaux. Physics of liquid jets. *Reports on Progress in Physics*, 71:036601, 2008.

[43] C.D. Eggleton and K.J. Stebe. An adsorption-desorption-controlled surfactant on a deforming droplet. *Journal of Colloid and Interface Science*, 208(1):68–80, 1998.

[44] R.B. Fdhila and P.C. Duineveld. The effect of surfactant on the rise of a spherical bubble at high Reynolds and Peclet numbers. *Physics of Fluids*, 8:310, 1996.

[45] J.Q. Feng. Buoyancy-driven motion of a gas bubble through viscous liquid in a round tube. *Journal of Fluid Mechanics*, 609:377–410, 2008.

[46] M. Fernandez, M.E. Munoz, A. Santamaria, R. Azaldegui, R. Diez, and M. Pelaez. Rheological analysis of highly pigmented inks: Flocculation at high temperatures. *Journal of Rheology*, 42:239, 1998.

[47] J.H. Ferziger and M. Perić. *Computational methods for fluid dynamics*, volume 2. Springer Berlin, 1999.

[48] A. M. Gañán-Calvo. Generation of steady liquid micro-threads and micron-sized monodisperse sprays in gas streams. *Physical Review Letters*, 80:285, 1998.

[49] A.M. Gañán-Calvo and J.M. Gordillo. Perfectly monodisperse microbubbling by capillary flow focusing. *Physical Review Letters*, 87(27):274501, 2001.

[50] S.N. Ghadiali and D.P. Gaver. The influence of non-equilibrium surfactant dynamics on the flow of a semi-infinite bubble in a rigid cylindrical capillary tube. *Journal of Fluid Mechanics*, 478:165–196, 2003.

[51] F.J.H. Gijsen, F.N. Van de Vosse, and J.D. Janssen. Wall shear stress in backward-facing step flow of a red blood cell suspension. *Biorheology*, 35:263–280, 1998.

[52] F.J.H. Gijsen, F.N. Van de Vosse, and J.D. Janssen. The influence of the non-newtonian properties of blood on the flow in large arteries: steady flow in a carotid bifurcation model. *Journal of Biomechanics*, 32(6):601–608, 1999.

[53] G.M. Ginley and C.J. Radke. Influence of soluble surfactants on the flow of long bubbles through a cylindrical capillary. In *ACS Symposium Series*, volume 396, pages 480–501. ACS Publications, 1989.

[54] D. Gueyffier, J. Li, A. Nadim, R. Scardovelli, and S. Zaleski. Volume-of-fluid interface tracking with smoothed surface stress methods for three-dimensional flows. *Journal of Computational Physics*, 152(2):423, 1999.

[55] P. Guillot, A. Colin, A.S. Utada, and A. Ajdari. Stability of a jet in confined pressure-driven biphasic flows at low Reynolds numbers. *Physical Review Letters*, 99(10):104502, 2007.

[56] O. Hassager. Negative wake behind bubbles in non-newtonian liquids. *Nature*, 279(402–403):6071, 1979.

[57] T. Hassenkam, L.L. Skovbjerg, and S.L.S. Stipp. Probing the intrinsically oil-wet surfaces of pores in North Sea chalk at subpore resolution. *Proceedings of the National Academy of Sciences*, 106(15):6071, 2009.

[58] J.R. Herrera-Velarde, R. Zenit, D. Chehata, and B. Mena. The flow of non-newtonian fluids around bubbles and its connection to the jump discontinuity. *Journal of Non-newtonian Fluid Mechanics*, 111(2-3):199–209, 2003.

[59] C.A. Hieber and H.H. Chiang. Shear-rate-dependence modeling of polymer melt viscosity. *Polymer Engineering & Science*, 32(14):931–938, 1992.

[60] C.W. Hirt and B.D. Nichols. Volume of fluid (vof) method for the dynamics of free boundaries* 1. *Journal of Computational Physics*, 39(1):201–225, 1981.

[61] S. Homma, K. Akimoto, J. Koga, and S. Matsumoto. Computations of the Breakup of a Jet into Drops in Non-Newtonian Liquid–Liquid Systems. *Journal of Chemical Engineering of Japan*, 40(11):920–927, 2007.

[62] S. Homma, M. Yokotsuka, and J. Koga. Numerical Simulation of the Formation of a Jet and Droplets from a Capillary in a Co-Flowing Ambient Fluid. *Journal of Chemical Engineering of Japan*, 43(1):7, 2010.

[63] Y. Hong and F. Wang. Flow rate effect on droplet control in a co-flowing microfluidic device. *Microfluidics and Nanofluidics*, 3(3):341, 2007.

[64] J. Hua, B. Zhang, and J. Lou. Numerical simulation of microdroplet formation in co-flowing immiscible liquids. *AIChE Journal*, 53:2534, 2007.

[65] K.J. Humphry, A. Ajdari, A. Fernández-Nieves, H.A. Stone, and D.A. Weitz. Suppression of instabilities in multiphase flow by geometric confinement. *Physical Review E*, 79(5):56310, 2009.

[66] F. Jin, N.R. Gupta, and K.J. Stebe. The detachment of a viscous drop in a viscous solution in the presence of a soluble surfactant. *Physics of Fluids*, 18:022103, 2006.

[67] F. Jin and K.J. Stebe. The effects of a diffusion controlled surfactant on a viscous drop injected into a viscous medium. *Physics of Fluids*, 19:112103, 2007.

[68] R.A. Johnson and A. Borhan. Effect of insoluble surfactants on the pressure-driven motion of a drop in a tube in the limit of high surface coverage. *Journal of Colloid and Interface Science*, 218(1):184–200, 1999.

[69] R.A. Johnson and A. Borhan. Pressure-driven motion of surfactant-laden drops through cylindrical capillaries: effect of surfactant solubility. *Journal of Colloid and Interface Science*, 261(2):529–541, 2003.

[70] D.D. Joseph and Y.Y. Renardy. Fundamentals of two-fluid dynamics. pt. i: Mathematical theory and applications. In *Fundamentals of two-fluid dynamics. Pt. I: Mathematical theory and applications Springer-Verlag (Interdisciplinary Applied Mathematics. Vol. 3), 473 p.*, volume 3, 1993.

[71] J.R. Kanicky, J.C. Lopez-Montilla, S. Pandey, and D.O. Shah. Surface chemistry in the petroleum industry. *Handbook of Applied Surface and Colloid Chemistry. John Wiley & Sons, New York*, pages 251–267, 2001.

[72] E. Kreyszig. *Advanced engineering mathematics*. Wiley-India, 2007.

[73] L.G. Leal. *Advanced transport phenomena: fluid mechanics and convective transport processes*. Cambridge Univ Pr, 2007.

[74] L.G. Leal, J. Skoog, and A. Acrivos. On the motion of gas bubbles in a viscoelastic liquid. *The Canadian Journal of Chemical Engineering*, 49(5):569–575, 1971.

[75] R.J. Leveque and Z. Li. The immersed interface method for elliptic equations with discontinuous coefficients and singular sources. *SIAM Journal on Numerical Analysis*, pages 1019–1044, 1994.

[76] J. Li, V. Bulusu, and N.R. Gupta. Buoyancy-driven motion of bubbles in square channels. *Chemical Engineering Science*, 63(14):3766–3774, 2008.

[77] J. Li and M.A. Fontelos. Drop dynamics on the beads-on-string structure for viscoelastic jets: A numerical study. *Physics of Fluids*, 15:922, 2003.

[78] Z. Li and K. Ito. *The immersed interface method: numerical solutions of PDEs involving interfaces and irregular domains*, volume 33. Society for Industrial Mathematics, 2006.

[79] Y. Liao and J.B. McLaughlin. Bubble motion in aqueous surfactant solutions. *Journal of Colloid and Interface Science*, 224(2):297–310, 2000.

[80] Y.J. Liu, T.Y. Liao, and D.D. Joseph. A two-dimensional cusp at the trailing edge of an air bubble rising in a viscoelastic liquid. *Journal of Fluid Mechanics*, 304:321–342, 1995.

[81] M.S. Longuet-Higgins, B.R. Kerman, and K. Lunde. The release of air bubbles from an underwater nozzle. *Journal of Fluid Mechanics*, 230:365, 1991.

[82] A. G. Marin, F. Campo-Cortes, and J. M. Gordillo. Generation of micron-sized drops and bubbles through viscous co-flows. *Colloids and Surfaces A: Physicochemical and Engineering Aspects*, 344:2, 2009.

[83] J.B. Mclaughlin. Numerical simulation of bubble motion in water. *Journal of Colloid and Interface Science*, 184(2):614–625, 1996.

[84] W.J. Milliken and L.G. Leal. The influence of surfactant on the deformation and breakup of a viscous drop: the effect of surfactant solubility. *Journal of Colloid and Interface Science*, 166(2):275–285, 1994.

[85] K. Mukundakrishnan, S. Quan, D.M. Eckmann, and P.S. Ayyaswamy. Numerical study of wall effects on buoyant gas-bubble rise in a liquid-filled finite cylinder. *Physical Review E*, 76(3):036308, 2007.

[86] M. Muradoglu and G. Tryggvason. A front-tracking method for computation of interfacial flows with soluble surfactants. *Journal of Computational Physics*, 227:2238–2262, 2008.

[87] W. Noh and P. Woodward. Slic (simple line interface calculation). In *Proceedings of the Fifth International Conference on Numerical Methods in Fluid Dynamics June 28–July 2, 1976 Twente University, Enschede*, pages 330–340. Springer, 1976.

[88] H.N. Oguz and A. Prosperetti. Dynamics of bubble growth and detachment from a needle. *Journal of Fluid Mechanics*, 257:111, 1993.

[89] M. Ohta, E. Iwasaki, E. Obata, and Y. Yoshida. A numerical study of the motion of a spherical drop rising in shear-thinning fluid systems. *Journal of Non-newtonian Fluid Mechanics*, 116(1):95–111, 2003.

[90] M. Ohta, E. Iwasaki, E. Obata, and Y. Yoshida. Dynamic processes in a deformed drop rising through shear-thinning fluids. *Journal of Non-newtonian Fluid Mechanics*, 132(1-3):100–107, 2005.

[91] M. Ohta, Y. Yoshida, and M. Sussman. Three-dimensional computations of the motion of a Newtonian drop rising through immiscible quiescent shear-thinning liquids. *Journal of Chemical Engineering of Japan*, 39(4):394–400, 2006.

[92] W.L. Olbricht. Pore-scale prototypes of multiphase flow in porous media. *Annual Review of Fluid Mechanics*, 28(1):187–213, 1996.

[93] W.L. Olbricht and D.M. Kung. The deformation and breakup of liquid drops in low Reynolds number flow through a capillary. *Physics of Fluids A: Fluid Dynamics*, 4:1347, 1992.

[94] M.S.N. Oliveira and G.H. McKinley. Iterated stretching and multiple beads-on-a-string phenomena in dilute solutions of highly extensible flexible polymers. *Physics of Fluids*, 17:071704, 2005.

[95] S. Osher and R.P. Fedkiw. *Level set methods and dynamic implicit surfaces*, volume 153. Springer Verlag, 2003.

[96] R. Palaparthi, D.T. Papageorgiou, and C. Maldarelli. Theory and experiments on the stagnant cap regime in the motion of spherical surfactant-laden bubbles. *Journal of Fluid Mechanics*, 559:1–44, 2006.

[97] G. Pangalos, J.M. Dealy, and M.B. Lyne. Rheological properties of news inks. *Journal of Rheology*, 29:471, 1985.

[98] C.W. Park. Influence of soluble surfactants on the motion of a finite bubble in a capillary tube. *Physics of Fluids A: Fluid Dynamics*, 4:2335, 1992.

[99] C.S. Peskin. The fluid dynamics of heart valves: experimental, theoretical, and computational methods. *Annual Review of Fluid Mechanics*, 14(1):235–259, 1982.

[100] S. Popinet and S. Zaleski. A front-tracking algorithm for accurate representation of surface tension. *International Journal for Numerical Methods in Fluids*, 30(6):775, 1999.

[101] W.H. Press. *Numerical recipes in FORTRAN: the art of scientific computing*, volume 1. Cambridge Univ Pr, 1992.

[102] J. Ratulowski and H.C. Chang. Marangoni effects of trace impurities on the motion of long gas bubbles in capillaries. *Journal of Fluid Mechanics*, 210:303–328, 1990.

[103] D.A. Reinelt. The rate at which a long bubble rises in a vertical tube. *Journal of Fluid Mechanics*, 175:557–565, 1987.

[104] D. Rodrigue. The effect of surfactants on deformation of falling non-Newtonian drops in a Newtonian liquid. *The Canadian Journal of Chemical Engineering*, 86(1):105–109, 2008.

[105] D. Rodrigue and D. De Kee. Bubble velocity jump discontinuity in polyacrylamide solutions: a photographic study. *Rheologica Acta*, 38(2):177–182, 1999.

[106] D. Rodrigue, D. De Kee, and C.F. Chan Man Fong. An experimental study of the effect of surfactants on the free rise velocity of gas bubbles. *Journal of Non-newtonian Fluid Mechanics*, 66(2-3):213–232, 1996.

[107] D. Rodrigue, D. De Kee, and C.F. Chan Man Fong. Bubble velocities: further developments on the jump discontinuity. *Journal of Non-newtonian Fluid Mechanics*, 79(1):45–55, 1998.

[108] M.J Rosen. *Surfactants and interfacial phenomena*. Wiley Online Library, 2004.

[109] G. Ryskin and L.G. Leal. Numerical solution of free-boundary problems in fluid mechanics. Part 1. The finite-difference technique. *Journal of Fluid Mechanics*, 148:1–17, 1984.

[110] G. Ryskin and L.G. Leal. Numerical solution of free-boundary problems in fluid mechanics. Part 2. Buoyancy-driven motion of a gas bubble through a quiescent liquid. *Journal of Fluid Mechanics*, 148:19–35, 1984.

[111] R. Scardovelli and S. Zaleski. Direct numerical simulation of free-surface and interfacial flow. *Annual Review of Fluid Mechanics*, 31(1):567–603, 1999.

[112] L.W. Schwartz, H.M. Princen, and A.D. Kiss. On the motion of bubbles in capillary tubes. *Journal of Fluid Mechanics*, 172:259–275, 1986.

[113] T.W. Secomb. Mechanics of blood flow in the microcirculation. In *Symposia of the Society for Experimental Biology*, volume 49, page 305, 1995.

[114] T.W. Secomb, R. Skalak, N. Ozkaya, and J.F. Gross. Flow of axisymmetric red blood cells in narrow capillaries. *Journal of Fluid Mechanics*, 163:405–423, 1986.

[115] H.J. Shore and G.M. Harrison. The effect of added polymers on the formation of drops ejected from a nozzle. *Physics of Fluids*, 17:033104, 2005.

[116] K.J. Stebe and D. Barthes-Biesel. Marangoni effects of adsorption-desorption controlled surfactants on the leading end of an infinitely long bubble in a capillary. *Journal of Fluid Mechanics*, 286:25–48, 1995.

[117] H.A. Stone. A simple derivation of the time-dependent convective-diffusion equation for surfactant transport along a deforming interface. *Physics of Fluids A: Fluid Dynamics*, 2:111, 1990.

[118] H.A. Stone. Dynamics of drop deformation and breakup in viscous fluids. *Annual Review of Fluid Mechanics*, 26:65–102, 1994.

[119] H.A. Stone, A.D. Stroock, and A. Ajdari. Engineering flows in small devices. *Annual Review of Fluid Mechanics*, 36:381–411, 2004.

[120] R. Suryo and O.A. Basaran. Tip streaming from a liquid drop forming from a tube in a co-flowing outer fluid. *Physics of Fluids*, 18:082102, 2006.

[121] M. Sussman, E. Fatemi, P. Smereka, and S. Osher. An improved level set method for incompressible two-phase flows. *Computers & Fluids*, 27(5-6):663–680, 1998.

[122] M. Sussman, P. Smereka, and S. Osher. A level set approach for computing solutions to incompressible two-phase flow. *Journal of computational Physics*, 114(1):146–159, 1994.

[123] P. Tabeling. *Introduction to microfluidics*. Oxford University Press, USA, 2005.

[124] T. Taha and Z.F. Cui. CFD modelling of slug flow in vertical tubes. *Chemical Engineering Science*, 61(2):676–687, 2006.

[125] T. Taha and Z.F. Cui. CFD modelling of slug flow inside square capillaries. *Chemical Engineering Science*, 61(2):665–675, 2006.

[126] F. Takemura. Adsorption of surfactants onto the surface of a spherical rising bubble and its effect on the terminal velocity of the bubble. *Physics of Fluids*, 17:048104, 2005.

[127] R.I. Tanner. *Engineering rheology*. Oxford University Press, USA, 2000.

[128] S. Tasoglu, U. Demirci, and M. Muradoglu. The effect of soluble surfactant on the transient motion of a buoyancy-driven bubble. *Physics of Fluids*, 20:040805, 2008.

[129] P.B. Umbanhowar, V. Prasad, and D.A. Weitz. Monodisperse emulsion generation via drop break off in a coflowing stream. *Langmuir*, 16:347, 2000.

[130] S. O. Unverdi and G. Tryyvason. A front-tracking method for viscous, incompressible, multi-fluid flows. *Journal of Computational Physics*, 100:25, 1992.

[131] A.S. Utada, A. Fernández-Nieves, J. M. Gordillo, and D.H. Weitz. Absolute instability of a liquid jet in a co-flowing stream. *Physical Review Letter*, 100:014502, 2008.

[132] A.S. Utada, A. Fernández-Nieves, H.A. Stone, and D.H. Weitz. Dripping to jetting transitions in co-flowing liquid streams. *Physical Review Letter*, 99:094502, 2007.

[133] L.A. Utracki. *Polymer alloys and blends: thermodynamics and rheology*. Hanser Munich, 1990.

[134] B. Vempati, M.V. Panchagnula, A. Öztekin, and S. Neti. Numerical investigation of liquid-liquid coaxial flows. *Journal of Fluids Engineering*, 129:713, 2007.

[135] F. Viana, R. Pardo, R. Yanez, J.L. Trallero, and D.D. Joseph. Universal correlation for the rise velocity of long gas bubbles in round pipes. *Journal of Fluid Mechanics*, 494:379–398, 2003.

[136] Y. Wang, D.T. Papageorgiou, and C. Maldarelli. Using surfactants to control the formation and size of wakes behind moving bubbles at order-one Reynolds numbers. *Journal of Fluid Mechanics*, 453:1–19, 2002.

[137] H. Wong, D. Rumschitzki, and C. Maldarelli. On the surfactant mass balance at a deforming fluid interface. *Physics of Fluids*, 8:3203, 1996.

[138] H. Wong, D. Rumschitzki, and C. Maldarelli. Theory and experiment on the low-Reynolds-number expansion and contraction of a bubble pinned at a submerged tube tip. *Journal of Fluid Mechanics*, 356:93, 1998.

[139] H. Wong, D. Rumschitzki, and C. Maldarelli. Marangoni effects on the motion of an expanding or contracting bubble pinned at a submerged tube tip. *Journal of Fluid Mechanics*, 379:279, 1999.

[140] Q. Xu, Y.C. Liao, and O.A. Basaran. Can surfactant be present at pinch-off of a liquid filament? *Physical Review Letter*, 98(5):54503, 2007.

[141] Z. Xue, C.M. Corvalan, V. Dravid, and P.E. Sojka. Breakup of shear-thinning liquid jets with surfactants. *Chemical Engineering Science*, 63(7):1842–1849, 2008.

[142] K.Y. Yasuda, R.C. Armstrong, and R.E. Cohen. Shear flow properties of concentrated solutions of linear and star branched polystyrenes. *Rheologica Acta*, 20(2):163–178, 1981.

[143] O.E. Yildirim and O.A. Basaran. Dynamics of formation and dripping of drops of deformation-rate-thinning and-thickening liquids from capillary tubes. *Journal of Non-newtonian Fluid Mechanics*, 136(1):17–37, 2006.

[144] R. You, A. Borhan, and H. Haj-Hariri. A finite volume formulation for simulating drop motion in a viscoelastic two-phase system. *Journal of Non-Newtonian Fluid Mechanics*, 153(2-3):109–129, 2008.

[145] R. You, A. Borhan, and H. Haj-Hariri. Stability analysis of cusped bubbles in viscoelastic flows. *Journal of Fluid Mechanics*, 621(1):131–154, 2009.

[146] R. You, H. Haj-Hariri, and A. Borhan. Confined drop motion in viscoelastic two-phase systems. *Physics of Fluids*, 21:013102, 2009.

[147] D.F. Zhang and H.A. Stone. Drop formation in viscous flows at a vertical capillary tube. *Physics of Fluids*, 9(8):2234, 1997.

[148] J. Zhang, D.M. Eckmann, and P.S. Ayyaswamy. A front tracking method for a deformable intravascular bubble in a tube with soluble surfactant transport. *Journal of Computational Physics*, 214:366–396, 2006.

[149] X. Zhang. Dynamics of drop formation in viscous flows. *Chemical Engineering Science*, 54(12):1759, 1999.

[150] X. Zhang and O.A. Basaran. An experimental study of dynamics of drop formation. *Physics of Fluids*, 7:1184–1203, 1995.

[151] Y. Zhang and J.A. Finch. A note on single bubble motion in surfactant solutions. *Journal of Fluid Mechanics*, 429:63–66, 2001.

[152] Y. Zhang, J.B. McLaughlin, and J.A. Finch. Bubble velocity profile and model of surfactant mass transfer to bubble surface. *Chemical Engineering Science*, 56:6605–6616, 2001.

Appendix A

Derivation of the Single-fluid VOF

Formulation

Start from the linear momentum balance for a control volume containing a singular interface which separates the two phases 1 and 2 [70, 73] sketched in Fig. A-1:

$$\frac{D}{Dt} \iiint_V \tilde{\rho} \mathbf{u}^* dV = \iint_S \mathbf{n} \cdot \Pi^* ds + \int_C \sigma^* \mathbf{m} dl - \iint_S (\rho_2 - \rho_1) \mathbf{g} \cdot \mathbf{x}^* \mathbf{n} ds. \qquad (A.1)$$

Here $\Pi^* = -P^* \mathbf{I} + \boldsymbol{\tau}^*$ is the modified stress tensor expressed in term of the modified pressure P^*, and $\tilde{\rho}$ is ρ_1 or ρ_2 for drop or bulk phase. Seen in Fig. A-1, $V = V_1 + V_2$ denotes the total control volume, $S = S_1 + S_2$ denotes the total area of the control volume, C denotes the perimeter of the interface, and $\mathbf{m} = \mathbf{t} \times \mathbf{n}$ is a unit vector which lies in S_{int} and is normal to the curve C.

Next, each term in Eq. A.1 must be converted into the volume integral. Surface integrals can be converted into volume integrals via the Gauss divergence theorem, and the line integrals can be converted into surface integrals via the Stokes' theorem [72] as below:

$$\iint_S \mathbf{n} \cdot \Pi^* ds = \iiint_V \nabla^* \cdot \Pi^* dV, \qquad (A.2)$$

$$\int_C \sigma^* \mathbf{m} dl = \iint_S \left[\nabla_s^* \sigma^* - \sigma^* \mathbf{n} (\nabla^* \cdot \mathbf{n}) \right] ds, \qquad (A.3)$$

$$\iint_S \left[\nabla_s^* \sigma^* - \sigma^* \mathbf{n} (\nabla^* \cdot \mathbf{n}) - (\rho_2 - \rho_1) \mathbf{g} \cdot \mathbf{x}^* \mathbf{n} \right] ds$$

$$= \iiint_V \left[\nabla_s^* \sigma^* - \sigma^* \mathbf{n} (\nabla^* \cdot \mathbf{n}) - (\rho_2 - \rho_1) \mathbf{g} \cdot \mathbf{x}^* \mathbf{n} \right] \delta_s^* dV. \qquad (A.4)$$

The term on the left hand side of Eq. A.1 can be treated by the Reynolds transport theorem [72] after applying the continuity equation as:

$$\frac{D}{Dt} \iiint_V \tilde{\rho} \mathbf{u}^* dV = \iiint_V \tilde{\rho} \frac{D\mathbf{u}^*}{Dt} dV. \qquad (A.5)$$
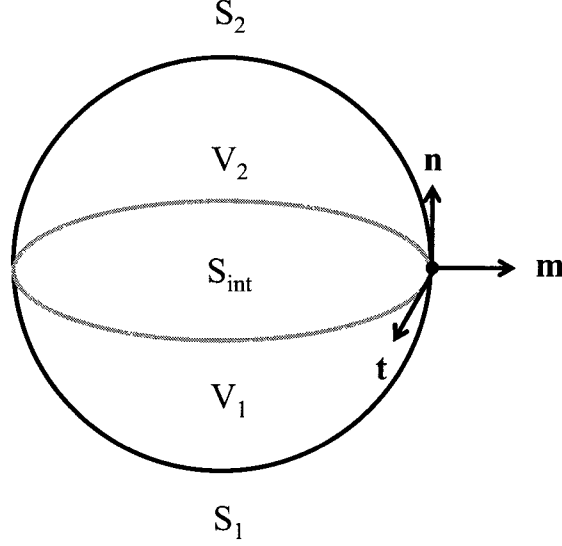
167

Figure A-1: Schematic of a control volume containing a singular interface which separates the two phases 1 and 2.

Thus, after removing volume integrals, Eq. A.1 becomes

$$\tilde{\rho}\left(\frac{\partial \mathbf{u}^*}{\partial t^*} + \mathbf{u}^* \cdot \nabla^* \mathbf{u}^*\right) = \nabla^* \Pi^* + \left[\nabla_s^* \sigma^* - \sigma^* \mathbf{n}\left(\nabla^* \cdot \mathbf{n}\right) - (\rho_2 - \rho_1)\,\mathbf{g} \cdot \mathbf{x}^* \mathbf{n}\right]\delta_s^*. \quad (A.6)$$

Then, by substituting $\Pi^* = -P^*\mathbf{I} + \boldsymbol{\tau}^*$ into Eq. A.6, the single-fluid VOF formulation in the dimensional form is obtained:

$$\tilde{\rho}\left(\frac{\partial \mathbf{u}^*}{\partial t^*} + \mathbf{u}^* \cdot \nabla^* \mathbf{u}^*\right) = -\nabla^* P^* + \nabla^* \cdot \left(\tilde{\mu}\left[(\nabla^* \mathbf{u}^*) + (\nabla^* \mathbf{u}^*)^T\right]\right)$$
$$+ \left[\nabla_s^* \sigma^* - \sigma^* \mathbf{n}\left(\nabla^* \cdot \mathbf{n}\right) - (\rho_2 - \rho_1)\,\mathbf{g} \cdot \mathbf{x}^* \mathbf{n}\right]\delta_s^*, \quad (A.7)$$

where $\tilde{\mu}$ is μ_1 or μ_2 for drop or bulk phase.

Finally, the single-fluid VOF formulation in the dimensionless form via nondimensionalizing with l_c, u_c, $t_c = l_c/u_c$, $P_c = \mu_2 u_c/l_c$, and σ_c is given by

$$\bar{\rho}Re\left(\frac{\partial \mathbf{u}}{\partial t} + \mathbf{u} \cdot \nabla \mathbf{u}\right) = -\nabla P + \nabla \cdot \left(\bar{\mu}\left[(\nabla \mathbf{u}) + (\nabla \mathbf{u})^T\right]\right)$$
$$+ \frac{1}{Ca}\left[\nabla_s \sigma - \sigma \mathbf{n}\left(\nabla \cdot \mathbf{n}\right) + Bo\mathbf{z}\mathbf{n}\right]\delta_s. \quad (A.8)$$

Here, $\bar{\rho} = 1 - (1 - \chi)\,\phi$ and $\bar{\mu} = 1 - (1 - \lambda)\,\phi$, with $\chi = \rho_1/\rho_2$ and $\lambda = \mu_1/\mu_2$ representing the density and viscosity ratio of drop to bulk fluids, respectively.